

FINAL REPORT

PREDICTION OF COMBUSTION INDUCED VIBRATION IN ROCKET MOTORS

By

Warren C. Strahle
John C. Handley

Prepared for

THE U. S. ARMY BALLISTIC MISSILE DEFENSE
ADVANCED TECHNOLOGY CENTER
HUNTSVILLE, ALA. 35808
CONTRACT NO. DASG60-77-C-0054

April 1978

GEORGIA INSTITUTE OF TECHNOLOGY
SCHOOL OF AEROSPACE ENGINEERING
ATLANTA, GEORGIA 30332

1978



the noise are presented and a comparison is made of the theory and an actual motor firing.

UNCLASSIFIED

Abstract

The source of solid rocket motor vibration is investigated by treating the problem of pressure fluctuations inside the motor cavity. Theoretical aeroacoustics is applied to the cavity gases and imbedded burning metal agglomerates. Several critical experiments are performed to provide numerical input to the theory. Consideration of turbulence, combustion and entropy noise yields the conclusion that only one cause is dominant for the fluctuations in chamber pressure - that of interaction of turbulence with the exhaust nozzle. Typically, an 0.4% rms pressure fluctuation can be accounted for by this mechanism. Spectral distributions of the noise are presented and a comparison is made of the theory and an actual motor firing.

Table of Contents

	Page
Abstract	i
Table of Contents	ii
List of Illustrations	1
Nomenclature	3
I. Introduction	7
II. Results of the Theory	9
III. Experimental Results	13
A. Combustion Noise from Heterogeneous Propellant	13
B. Cross-flow Effects on Combustion Noise	30
C. Temperature Fluctuations	41
IV. Order of Magnitude Calculations	61
A. Turbulence Noise	63
B. Combustion Noise	69
C. Entropy Noise	72
V. Motor Prediction	73
VI. Conclusions	83
Appendix - General Theory	85
References	115

List of Illustrations

Figure		Page
III A-1	Solid Propellant Acoustic Tube Test Apparatus	14
III A-2	Propellant Strand Prepared for Acoustic Testing	15
III A-3	Data Acquisition System for Combustion Noise	18
III A-4	Data Reduction System for Combustion Noise	19
III A-5	Time History for a Typical Solid Propellant	20
III A-6	Pressure Spectra of a Typical Solid Propellant	21
III A-7	Strength of the Combustion Noise Source	26
III A-8	Time History for MC-170 using BBN 376 LF Microphone	27
III A-9	Pressure Spectra for MC-172 extending from 1.6 to 410 Hz	29
III B-1	Apparatus to Test Combustion-Flow Interaction	31
III B-2	Sample holder for 300 psie Combustion-Flow Interaction Tests	32
III B-3	Combustion-Flow Interaction Side Profiles	34
III B-4	Time History of Burning Surface Positions for T-48 at Atmospheric Pressure	35
III B-5	Time History of Area Correction Factor	36
III B-6	Sound Pressure Level History for Strand Test	39
III B-7	Sound Pressure Level History for U-shaped Channel Test	40
III C-1	Temperature Fluctuation Test Apparatus	44
III C-2	Photograph of Temperature Fluctuation Test Apparatus	45
III C-3	Temperature History for a Non-aluminized Propellant	47
III C-4	Temperature History for an Aluminized Propellant	48
III C-5	Temperature Spectra for Two Propellants	49
III C-6	Temperature Measured above the Burning Surface of a Non-aluminized Propellant	51

III C-7	Temperature Measured above the Burning Surface of an Aluminized Propellant	52
III C-8	Photograph of Temperature Fluctuation Measurement of UTP-3001 Propellant, 6.2" away from the Surface	53
III C-9	Temperature Measured above the Burning Surface of an Aluminized Propellant for Various Pressures.	56
III C-10	Temperature Spectra for an Aluminized Propellant at 900 psi	57
IV A-1	Turbulence Spectra from Laufer's Pipe Flow Data	65
V - 1	Turbulence Spectra as a Function of Radial Position with Wavenumber a Parameter	75
V - 2	Cutaway View of Solid Propellant Motor	79
V - 3	Comparison of Theoretical and Experimental Spectra for Hercules Motor	81
A - 1	Schematic of a Rocket Motor and Nomenclature Illustration	92
A - 2	Green's Function for Baseline Case and Its Low Frequency Approximation	103
A - 3	Green's Function for Various Pairs of Values of x and y	105
A - 4	Green's Function for Various Values of the Feedback Parameter, $\tilde{\mu}$	106
A - 5	Green's Function for Two Values of Exit Mach Number	108
A - 6	Green's Function for Two Values of Radial Mach Number at Fixed Motor Thrust	109
A - 7	Effect of Particle Mass Loading on the Green's Function	110

Nomenclature

A	feedback pacemeter
a	radius
a_{ω}	isentropic admittance coefficient
b_{ω}	entropy admittance coefficient
B	feedback parameter
c	speed of sound
c_p	specific heat at constant pressure
c^*	characteristic velocity
d	diameter
D_i	drag in i^{th} direction
e_1, e_r	unit vectors in axial and radial directions, respectively
f_i	force per unit volume
f	frequency
g_{ω}	Green's function developed in Appendix
G	one sided spectral density
\tilde{k}	wavenumber based on flow speed, ω/\bar{u}
k	wavenumber, ω/c_e
l	length
l_e	integral scale of turbulence
m	mass addition rate per unit volume or particle mass or mass flow rate per unit area
\mathcal{M}	combustion noise source function
M	Mach number
n	burn rate pressure exponent or number of droplets per unit volume
p	pressure
P	perimeter

r	radial coordinate or burn rate
Re	Reynolds number
s	entropy
S, S _{cor}	area, correlation area
St	Strouhal number
t	time
t ₀	sample time for Fourier transform
T	temperature
T _{ij}	$\rho_e u_i u_j$
u _i , u _l or u	velocity in i th direction, velocity in axial direction
v _i	velocity in i th direction
v	1/n
V, V _{cor}	chamber volume, correlation volume
x _i , x	coordinate in i th direction, axial coordinate
y _i , y	i th coordinate direction, axial coordinate
Y	mass fraction of droplets
z	droplet drag function defined in Eq. (11) of Appendix
\bar{D}/Dt	$\partial/\partial t + u_e \frac{\partial}{\partial x}$
$\langle \quad \rangle^2$	mean square value
α	thermal diffusivity or coefficients in boundary condition or droplet parameter of Eq. (7) of the Appendix
β	isentropic specific wall admittance, boundary condition parameters or droplet parameter of Eq. (8) of the Appendix
γ	ratio of specific heats
Γ	source function of Eq. (12) of the Appendix
δ	$\int_{S_w} \eta_w dS$ or Dirac delta function
η_i	coordinate in i th direction
θ	angular coordinate
κ	complex wavenumber

λ	defined in Eq. (12)
μ	gas viscosity
$\tilde{\mu}$	feedback parameter
ξ_i	coordinate in i^{th} direction
ρ	density
σ	dimensionless entropy fluctuation, s'/c_p
ω	circular frequency
Ω	frequency parameter in feedback law

Subscripts except where defined above

$I_a, I_b, I_c, II_a, II_b, III, IV_a, IV_b$	source term identifiers
d	condensed phase material
e	nozzle entrance plane or effective value
h	head end
inf	influence
i, j	cartesian coordinate directions
max	maximum
min	minimum
nit	nitrogen in pressurization vessel
p	pressure perturbation or particles
prop	immediately above propellant surface
r	radial component
rms	root mean square
S	condensed phase
w	propellant surface
oo	plane wave mode
δ	pertaining to δ

ω Fourier transform,

Superscripts except where defined above

' perturbation quantity

\sim coefficient in boundary conditions

$-$ mean value

I. Introduction

The propulsion community has traditionally resigned itself to acceptance of a background noise level in rocket motor pressure of the order of 1% of the mean chamber pressure. There has been little concern over the cause of such fluctuations, or their reduction, except in cases where a) they have substantially exceeded the 1% level or b) they have become phase coherent instabilities in the motor or engine. These chamber pressure fluctuations are, of course, a source of motor vibration. There are reasons why it would be desirable to reduce this vibration level. Consequently, this program was undertaken to understand the origin of the chamber pressure fluctuations and to understand the scaling rules in order to be able to design low vibration into a motor.

This report is concerned with solid rocket motors. Potential sources of noise in the chamber pressure are relatively easy to identify, although quantification is much more difficult. First, in the case of composite solid propellants the propellant is heterogeneous in structure. This forces an unsteady combustion process, and, hence fluctuations in chamber pressure. Secondly, the flow is turbulent within the motor cavity. There are pressure fluctuations due to the turbulence itself, there may be a turbulence-combustion interaction called direct combustion noise,⁽¹⁾ and there may be an interaction of the turbulence with the nozzle flow called nozzle-vorticity interaction noise.⁽²⁾ Thirdly, there may be hot spots in the flow field due to metal burning in the chamber volume; these hot spots (or cold spots) encountering the nozzle will give rise to

noise which has been called "entropy noise".⁽³⁾

To complicate the problem, there will be feedback between pressure fluctuations and the combustion process, and there will be damping of acoustic energy due to the presence of condensed phase material in the chamber gas flow. Moreover, there will be damping due to the exhaust of acoustic energy through the nozzle. The chamber pressure fluctuation which is ultimately achieved will depend upon a balance of the acoustic losses and the strength of the sources in the presence of feedback with the combustion process. This report attempts to calculate the stationary random oscillation which will be achieved for a given motor design. The treatment is necessarily approximate. What is primarily sought is a) the proper order of magnitude of the oscillation, b) a spectral shape estimate and c) scaling rules for the pressure fluctuation magnitude.

For reasons to be delineated below the theory will be based on the Lighthill approach⁽⁴⁾ to aeroacoustics.⁽⁵⁾ Where data are required to feed into the theory, appropriate data from the literature will be used, if it exists. In some areas, however, exploratory experiments are required to generate the data; these experiments are carried out and reported on in this report.

II. Results of the Theory

The details of the theoretical formulation and solution are contained in the Appendix. What is sought is an expression for the pressure fluctuation, and its spectral content. Accounted for in an approximate manner are particulate matter suspended in the gases, the effect of a mean flow and feedback between the pressure fluctuations and combustion process. These are effects which are important in the chamber acoustics. The sources of the pressure fluctuations are the turbulence, turbulence-combustion interaction, and turbulence-nozzle interaction. All of these have their representations in the theory.

The theory specifically considers a stationary random oscillation. At sufficiently high values of the propellant feedback response function the motor (and the computation) will indicate an instability. At this point the analysis will fail. The motor must be stable for this calculation to be valid. Even in the case of a stable rocket motor, there is a background noise level of pressure fluctuations. The calculation of the background level is the purpose of this program.

Major limitations of the theory are a) frequencies are restricted to those below cut-on of the first transverse mode of oscillation of the chamber gases and b) the cross-section area of the cavity must be reasonably invariant with axial position. The effects of these restrictions are that a) only axial vibration of the motor is under consideration and b) there may be difficulties in interpretation of data from motors with a complex grain configuration. The theory, therefore, only considers nearly plane wave motion in the motor cavity so that the pressure fluctuation, p' , is a function of axial length, x , alone. Vibration of a motor in the axial direction is set up by the difference in pressure acting on

the head end as opposed to the tail end, where the nozzle is discharging the gases and particles. Roughly, the thrust fluctuation is $F' \approx p' A_t$ so the pressure fluctuation is the primary quantity of interest.

The mean square pressure fluctuation, $\langle p'^2 \rangle$ is related to its spectral distribution, $G_p(f)$ by⁽⁶⁾

$$\langle p'^2 \rangle = \int_0^{\infty} G_p(f) df \quad (1)$$

where $G_p(f)$ may be estimated by a Fourier transform operation on p' by

$$G_p(f) = 2 \frac{p_{\omega}^* p_{\omega}}{t_0}$$

$$p_{\omega} = \int_0^{t_0} p'(t) e^{-2\pi i f t} dt \quad (2)$$

Consequently, the solution to the aeroacoustic problem is given in terms of the Fourier transform of the pressure fluctuation as the quantity of interest.

As shown in the appendix the solution for G_p at the boundary of the chamber (say, the head end) is given by

$$G_p = G_{P_{I_a}} + G_{P_{I_b}} + G_{P_{I_c}} + G_{P_{II_a}} + G_{P_{II_b}} + G_{P_{III}} \quad (3)$$

where each term in the sum is due to a specific noise source. In Eq. (3) an assumption is that there is no correlation between the different noise sources. This assumption is open to some question but becomes unimportant in the end, because only one of the terms of Eq. (3) is found to be important. In Eqs. (3) the terms designated by I have to do with noise caused by pure turbulence. I_a and I_b are related to the turbulence distributed through the cavity volume and are separated into two terms

purely for analytical convenience. Term I_c is caused by the interaction of the turbulence and the nozzle flow process. Term II_a deals with noise generated by combustion near the surface of a heterogeneous propellant and term II_b is combustion noise of particulate metal imbedded in the gas stream. Term III is noise from an interaction of hot spots with the nozzle flow process.

Written out in full the individual terms of Eq. (3) become

$$\begin{aligned}
 G_{PI_a} &= \frac{2M^4}{t_o} \left(\int_V g_\omega (T_{11})_\omega dV \right) \left(\int_V g_\omega^* (T_{11})_\omega^* dV \right) \\
 G_{PI_b} &= \frac{2}{t_o} \left(\int_{S_e} [\tilde{\alpha}_e + ikM_e(2+z_d)] g_\omega (T_{11})_\omega dS \right) \left(\int_{S_e} [\tilde{\alpha}_e + ikM_e(2+z_d)]^* g_\omega (T_{11})_\omega^* dS \right) \\
 G_{PI_c} &= \frac{2}{t_o} \left(\int_{S_e} g_\omega \frac{\partial}{\partial y_i} (T_{ii})_\omega dS \right) \left(\int_{S_e} g_\omega^* \frac{\partial}{\partial y_i} (T_{ii})_\omega^* dS \right) \\
 G_{PII_a} &= \frac{2k^2 \gamma^2 \bar{p}^2 M_r^2}{t_o} \left(\int_{S_w} g_\omega \mathcal{M}_\omega dS \right) \left(\int_{S_w} g_\omega^* \mathcal{M}_\omega dS \right) \\
 G_{PII_b} &= \frac{2}{t_o} k^2 \gamma \bar{p} \rho_e \left(\int_V \left(\frac{\bar{D}G}{Dt} \right)_\omega g_\omega dV \right) \left(\int_V \left(\frac{\bar{D}G}{Dt} \right)_\omega^* g_\omega^* dV \right) \\
 G_{PIII} &= \frac{2}{t_o} k^2 \gamma^2 \bar{p}^2 \left(\int_{S_e} b_\omega g_\omega \sigma_\omega dS \right) \left(\int_{S_e} b_\omega^* g_\omega^* \sigma_\omega^* dS \right) \quad (4)
 \end{aligned}$$

Each term of Eqs. (4) contributes to the square of the pressure fluctuation, so a square of a source term occurs in each of the above.

In each case either the volume or surface integral contains the number g_ω as a factor in the integrand. This is the Green's function for the duct acoustics problem and tells how a source gets turned into pressure, depending upon the location and the strength of the source. The Green's

function and its behavior are described in the Appendix. To calculate it requires the flow, particulate and nozzle details and also the behavior of the feedback response law for the propellant. At low frequencies an analytical expression for the Green's function is worked out in the Appendix. It is valid for frequencies lower than about 1/2 the first longitudinal mode frequency. The expression for the square of the Green's function is

$$g_{\omega} g_{\omega}^* = \frac{1}{M_e^2 k^2 S^2 \left[\frac{5-\gamma}{2} - \gamma n \right]^2} \quad (5)$$

This is useful for quick order of magnitude use in Eqs. (4) and for rough investigation of scaling rules.

In each of the terms of Eqs. (4) there is a source term to be evaluated. For example, in $G_{P_{I_a}}$, there is required knowledge for T_{11} , which is a turbulence fluctuation term. The estimation of these terms is deferred until Section IV.

Although it was not guaranteed at the outset, the theory has recovered every physically expected noise source. While the accuracy might not be high, because the simplest aeroacoustics formalism was used and several approximations were introduced, the scaling rules and order of magnitude of various terms should be correct. Moreover, the accuracy with which the input variables are known is low, as will be seen, because of the lack of some fundamental data on turbulence in solid rocket motor cavities. Consequently, it is considered that the accuracy of the theory and the accuracy of the input data are commensurate.

III. Experimental Results

After viewing the results of the theory, in Eqs. (4), there are several experimental inputs required. These are spatial correlation length scales and spectral behavior of the axial velocity fluctuations, temperature fluctuations and mass flow per unit area fluctuations just above the propellant surface. None of these quantities have been investigated in the literature in the detail required for this program. However, reasonable magnitude estimates may be made of the axial velocity turbulence characteristics through use of Laufer's pipe flow data⁽⁷⁾ as corrected by the results of Ref. 8, which investigated the effects of mass addition from the wall. The other data is generated here through experiments which, although not precision experiments, will yield preliminary magnitude and spectral estimates for the unknown quantities.

A. Combustion Noise from Heterogeneous Propellant

The object of this measurement was to determine the strength of the combustion noise source if the propellant were radiating sound to a free field. This information can be translated to knowledge of η_w in Eqs. (4). The apparatus shown in Fig. III A-1 was used to determine the acoustic properties of the burning propellant. This tube had a length of 64" (162.5 cm) and an inside diameter of 4" (10.16 cm). It was described in detail in Ref. (9). The tube had a maximum operating pressure of 1000 psi.

A typical sample is shown in Fig. III A-2. The strands of propellants were cut to be $\frac{1}{2}$ " x $\frac{1}{2}$ " x 3" (6.35 mm x 6.35 mm x 76.2 mm). This size of sample resulted in an average action time pressure approximately 10% higher than the initial pressure when the tube was pressurized to 300 psi. The sides of the strands used in this investigation were coated with approximately 1/8" (3.2mm) of Dow Corning silicon rubber coating to act as an inhibitor to the spread of deflagration down the side of the end burning strands. This thick coating

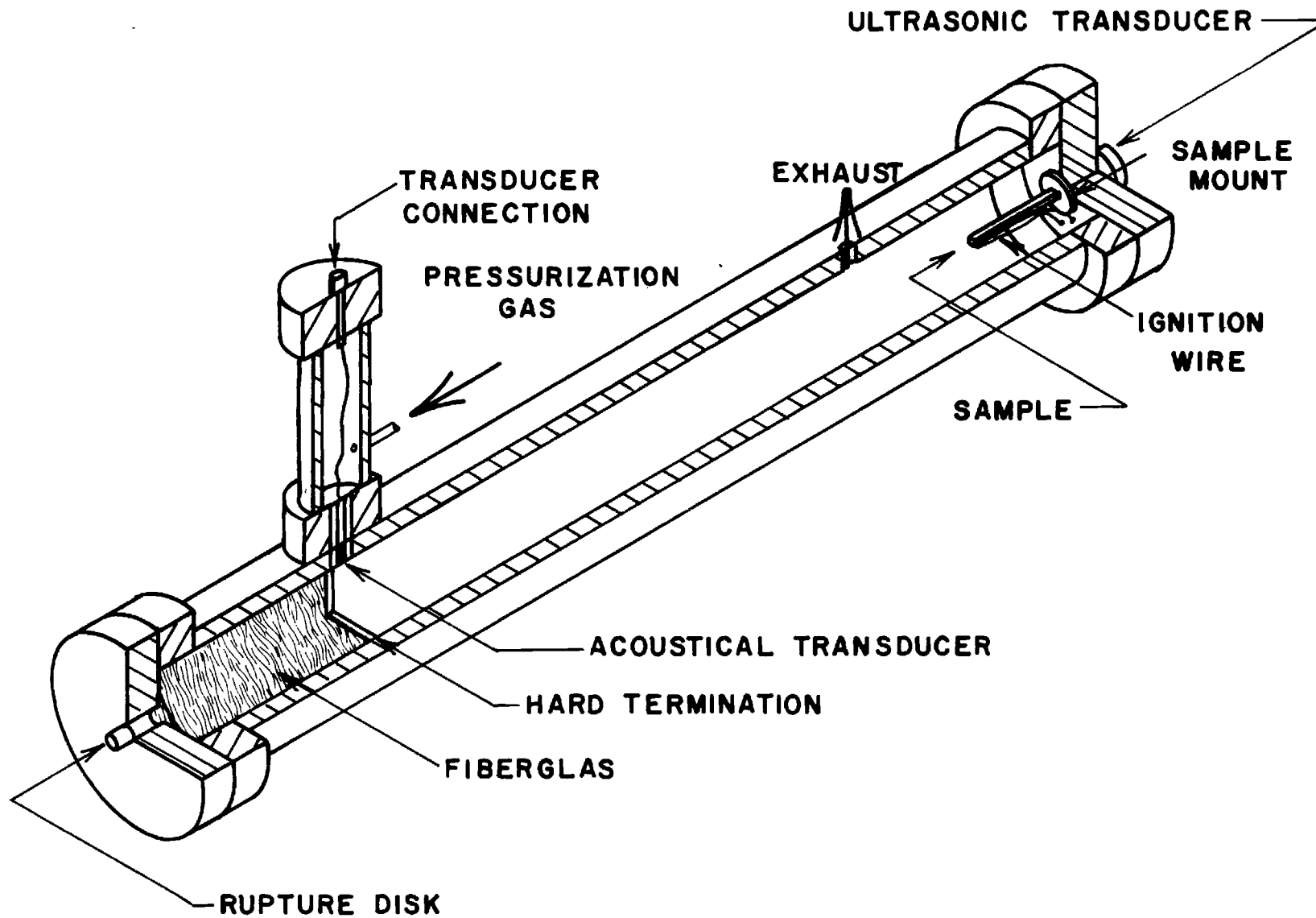


Figure III A-1. Solid Propellant Acoustic Tube Test Apparatus.

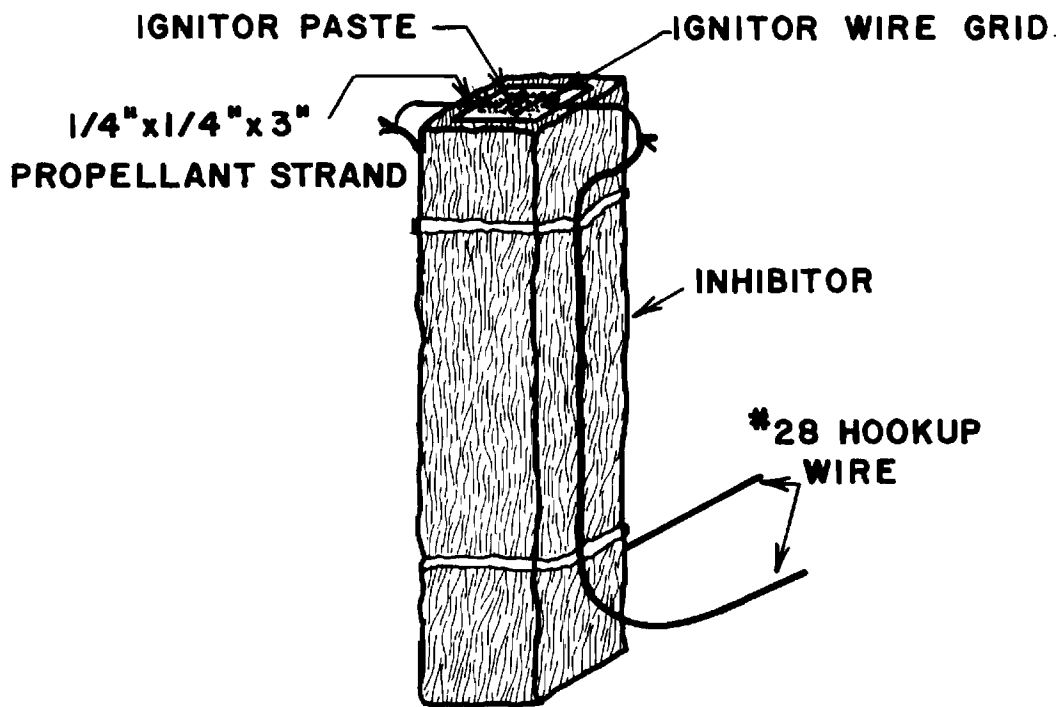


Figure III A-2. Propellant Strand Prepared for Acoustic Testing.

was necessary to prevent metal agglomerate recirculation ignition of the sample along the side of the sample when aluminized propellants were tested. Once the inhibitor on the side of the sample was cured the sample was trimmed and mounted on an aluminum flange using the same silicon rubber. The ignition power supply required approximately 1 3/4" (4.5 cm) of .010" (.25mm) diameter nichrome wire. This wire was formed into a grid and bonded to the 1/4" x 1/4" (6.35 mm x 6.35 mm) surface with a boron-titanium based ignitor paste (x - 225 pyrotechnic mixture). Two 6" electrical leads of #28 teflon insulated copper hookup wire were soldered to the ignitor wire for hookup to the electrical feed-through in the acoustic tube. These wires were then tied to the side of the inhibited sample to minimize the chance of ignition wire damage during handling.

The prepared sample was bolted on the one inch (2.54 cm) thick closure flange of the acoustic tube. A special viscous grease was used between the aluminum sample flange and the stainless steel closure flange to ensure a transmission path for ultrasonic acoustic emissions. Both of these flanges had precision ground surfaces at the mounting points. A Dunegan-Endevco Model D 9201 ultrasonic transducer was mounted on the opposite side of the closure flange to measure the ultrasonic acoustic emission of the burning propellant. This signal was used to determine the burn rate. The prepared sample is located at the right hand end of the acoustic emission tube shown in Fig. III A-1.

An acoustic hard termination with a vent hole in the center was located 7.87" (20 cm) away from the left hand end closure flange. The acoustical transducer, a BBN Model 376A or 376LF, piezoelectric sensor was located immediately in front of the hard termination. A CEC Model 20077 pressure transducer was located in the exhaust line to record the pressure rise due

to combustion of the solid propellant in the acoustic tube.

The three signals were filtered and amplified and then recorded on a magnetic tape recorder. The acoustic data and the pressure data were recorded using the FM mode for more accurate signal reproduction. Recording at 60 in/sec (152.4 cm/sec) gave an upper limit of 30,000 Hz. It was necessary to record the ultrasonic signal using the direct or AM mode of signal recording. This gave an upper limit of 300 kHz. The data acquisition system is shown schematically in Fig. III A-3.

The signals were then played back at reduced rates for graphical reproduction and Fourier analysis. Some signal conditioning in the form of filtering, discriminating and counting was necessary for all channels. The data reduction system is shown schematically in Fig. III A-4.

Typical results for an aluminized propellant, MC-170, are shown in Fig. III A-5. The pressure rise for this test was from 300 psi to 366 psi. The average pressure was 333 psi. The acoustic signal detected by the acoustic transducer represented an average sound pressure level of 91 db re 2×10^{-5} N/m². The burn time indicated by the ultrasonic transducer agreed with the pressure rise and the acoustic signal. It was a uniform burning strand with an initial burst of ultrasonic noise due to the ignitor paste and a final burst due to the non-uniform burning as the deflagration reaches the mounting flange and the mounting material. This sample was 3.5" (8.9 cm) long. The burn rate for this propellant was .39 cm/sec (1 cm/sec) at 300 psi.

The pressure spectral level of the acoustic signal was obtained using the Hewlett Packard 5451A Fourier Analyzer. The preliminary analysis of the acoustic signal shown in Fig. III A-5 is shown in Fig. III A-6. The range of this analysis was from 4 Hz to 1024 Hz with a resolution of 4 Hz. This was obtained by using a block size of 512, a time window of 2 seconds

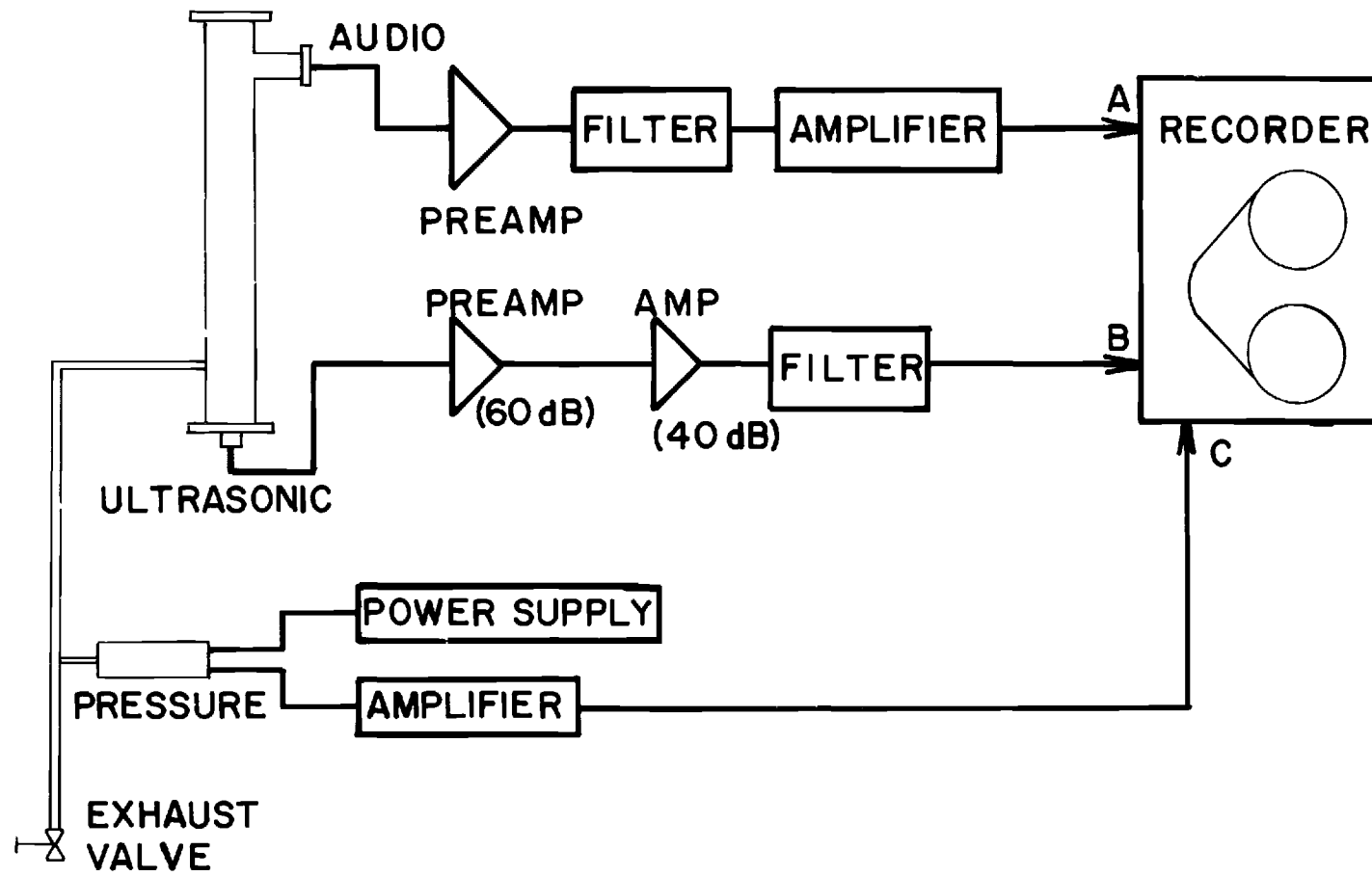


Figure III A-3. Data Acquisition System for Combustion Noise.

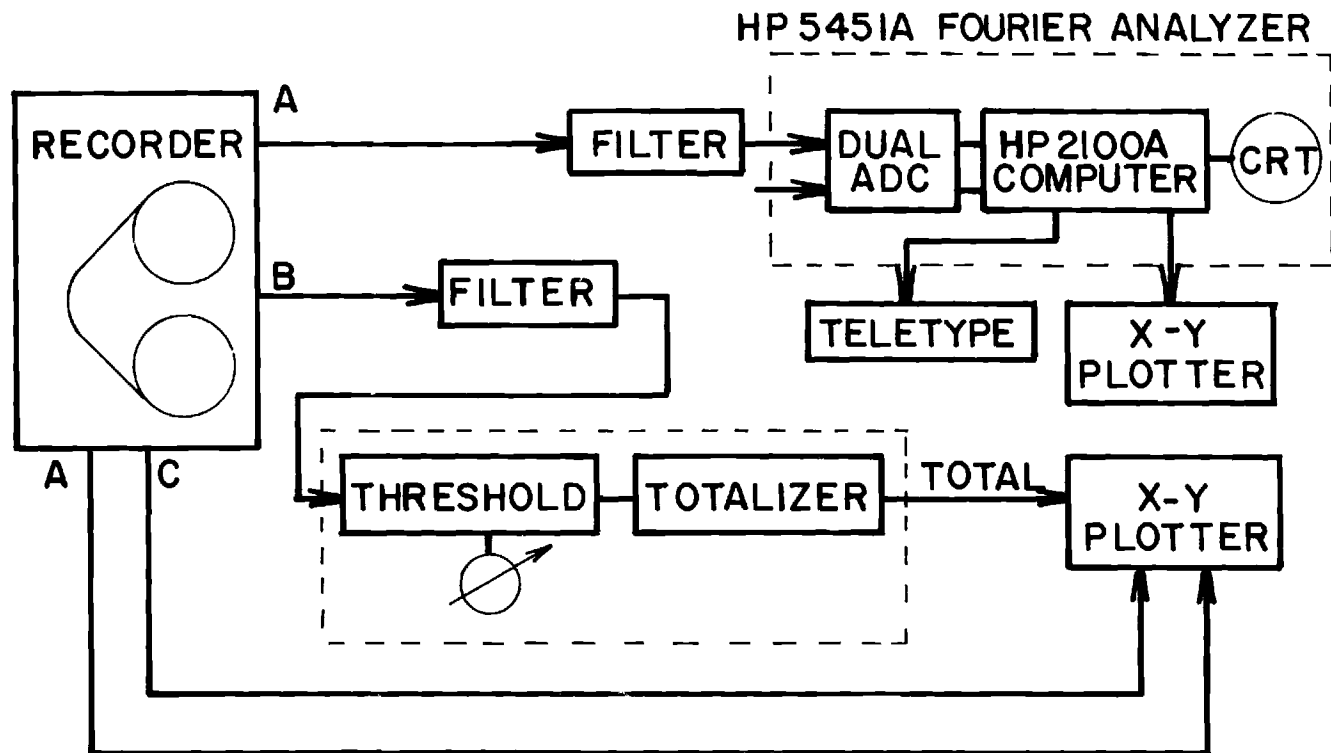


Figure III A-4. Data Reduction System for Combustion Noise.

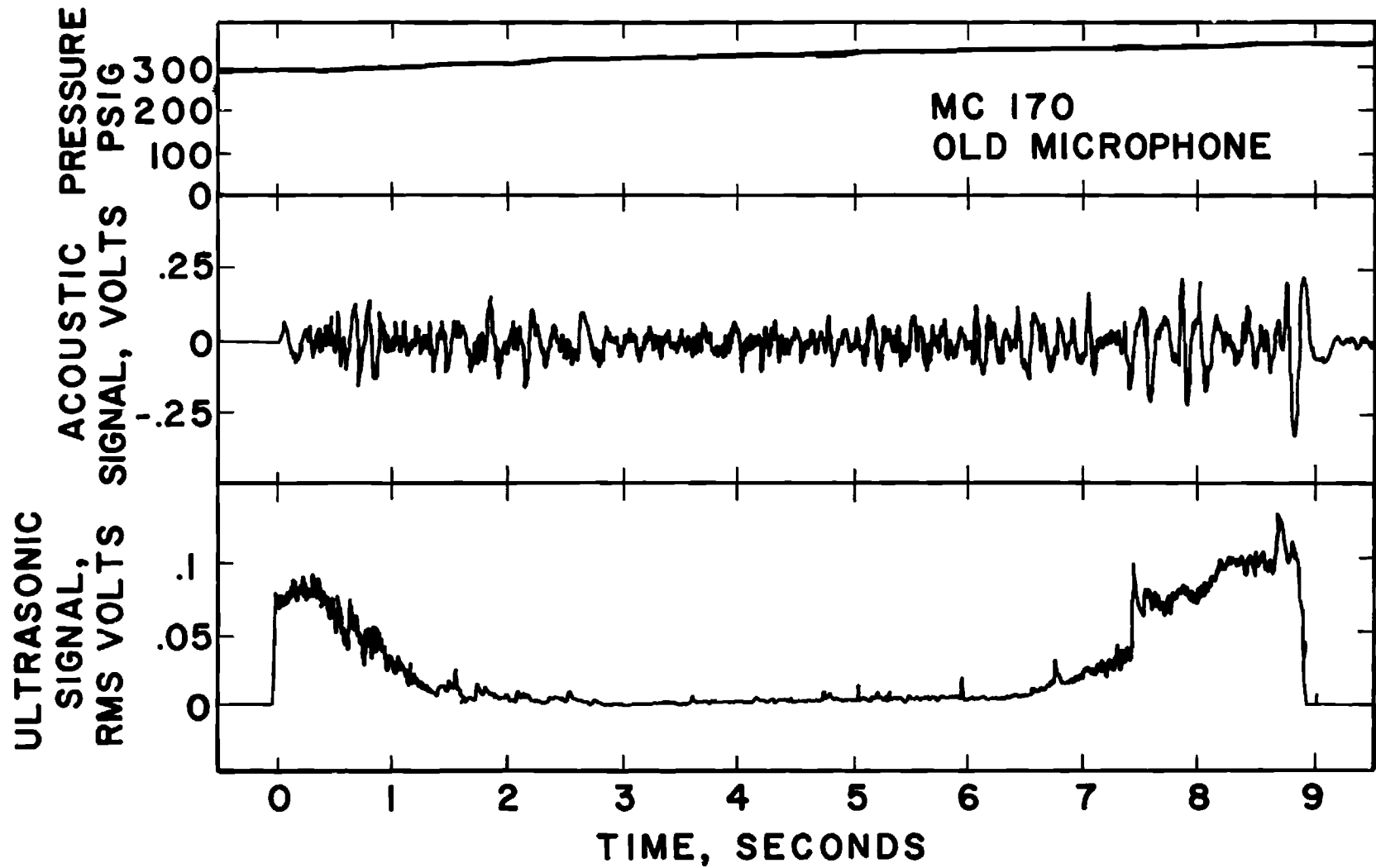


Figure III A-5. Time History for a Typical Solid Propellant.

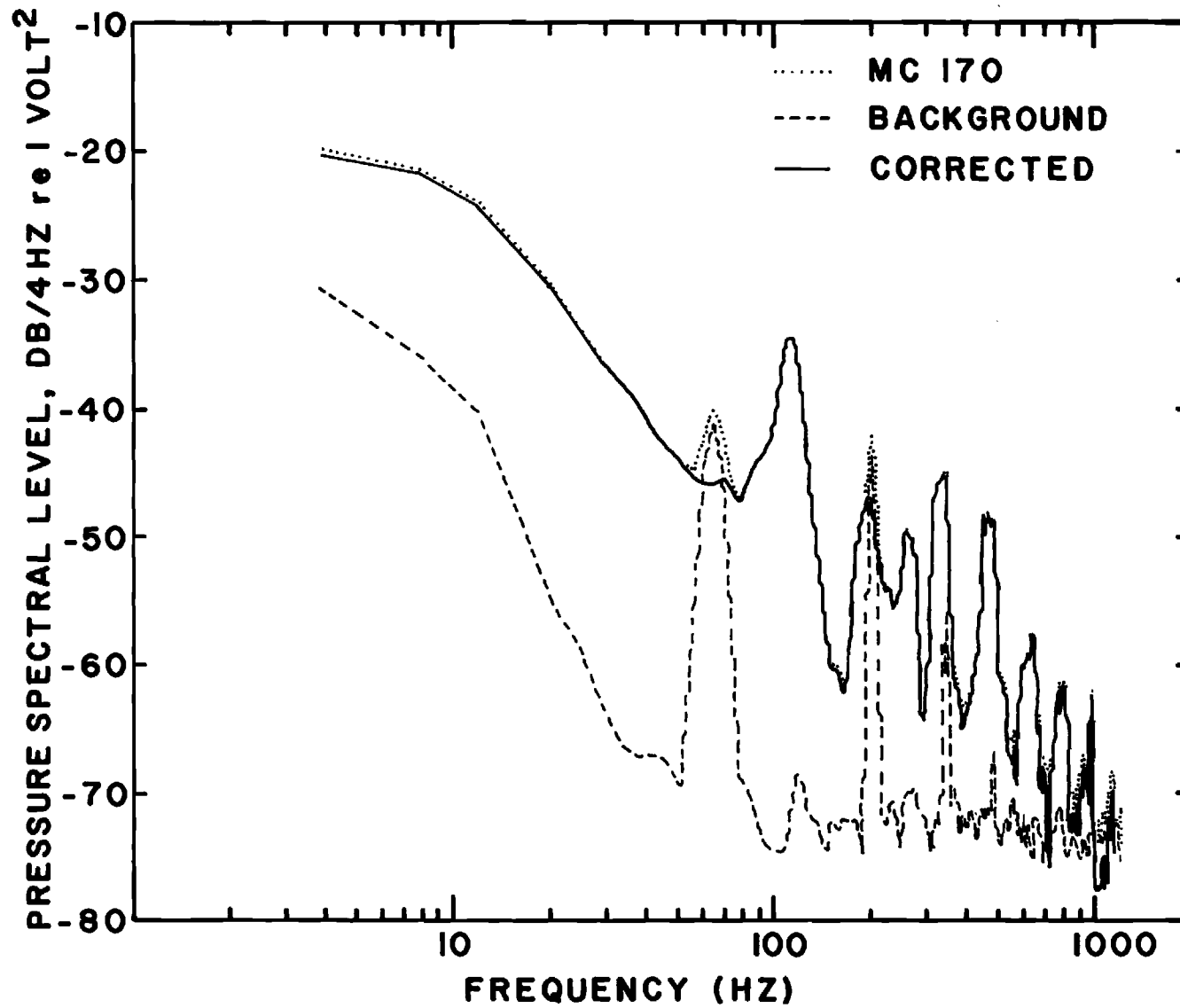


Figure III A-6. Pressure Spectra of a Typical Solid Propellant.

and a speed reduction of 8:1 on the magnetic tape recorder. The signals were digitized and two Hanning windows were used to reduce leakage. All acoustic signals obtained in this section of the investigation were filtered with a Krohn-Hite electronic filter, model 3323R, set to pass all frequencies above 5 Hz. This was necessary to prevent saturation of Neff amplifiers due to large scale, low frequency oscillations of the acoustic signal. These oscillations were initiated by the ignition and starting transient of the combustion process. The magnitude and duration of these oscillations were enhanced by the BBN power supply, Model P-16, and lower high pass frequency settings of the Krohn-Hite filter. A 60 Hz noise problem in the recorded acoustic signal was discovered when the data reduction for this series of tests was initiated. This was traced to the Krohn-Hite filter. This 60 Hz signal was within the specifications of the filter and only became a problem when it was amplified by the Neff amplifier at a gain of 500 or 1000. The occurrence of the 60 Hz signal and its harmonics at comparable levels with the combustion generated noise is shown in Fig. III A-6. There was sufficient recorded signal to obtain background pressure spectral levels for all propellants at 300 psi, before sample ignition. This signal, labeled background, was subtracted from the uncorrected spectra, giving the corrected pressure spectral level. This reduced the peaks in the pressure spectra at 60, 180 and 300 Hz.

These corrected pressure spectra were further reduced to yield the strength of the combustion noise source if the propellant were radiating sound to a free field. The corrected pressure spectral level shown in Fig. III A-6 can be related to the actual pressure fluctuation in the following manner

$$PSL/4Hz = 10 \log G_p' \text{ 1volt}^2$$

This G_p can be related directly to the calibration of the acoustic transducer. The tape recorder had a voltage reduction of 4.47, the Neff amplifier had a gain of 500 and the acoustic calibration of the transducer for a signal 160 db re .0002 dy/cm² gave .122 volt, RMS. The actual strength of the combustion noise source, G_δ , as required in the theory,⁽¹⁰⁾ is related to the pressure spectral level G_p as follows.

$$G_\delta = \left(\frac{c_{prop}}{c_{nit}} \right)^2 \left(\frac{1}{P} \right)^2 G_p (\sin^2 kl + \beta^2 \cos kl)$$

The quantity β was evaluated at the first peak and trough.⁽¹⁰⁾

$$G_p(\text{peak})/G_p(\text{trough}) = 1/\beta^2$$

Three propellants were tested initially. They were MC-170, UTP-3001 and a CMDB propellant. The CMDB propellant was obtained from the U. S. Army BMDATC for this program. The composition of these propellants along with that of two other propellants MC-172 and T-48, is given in Table III A-1.

The sample burn rate, tube average pressure and the average sound pressure level for the comparison of the two BBN transducers, models 376A and 376LF (the low frequency transducer) are shown in Table III A-2. The actual strength of the combustion noise source, G_δ , is shown in Fig. III A-7 for the six tests. The pressure spectral levels were corrected for the frequency range 4 Hz through the third trough of Fig. III A-6.

The results for MC-170 using the low frequency transducer do not agree with the other two propellant results. The sample did not burn linearly. This is shown in Fig. III A-8 where the pressure signal does not agree with the ultrasonic signal. The rapid pressure increase has driven the acoustic transducer to saturation. This transducer appears to recover, but there is no acoustic signal for the rest of the run. This behavior was noted for all

Table III A-1 Properties of Propellants used in Tests

Designation	AP		Al	Binder	
MC-170	200 μ m	26.8%	68%	5 μ m 20%	HTPB 12%
	14 μ m	20.4%			
	6 μ m	20.8%			
UTP-3001	190 μ m	44.3%	67.5%	38 μ m 16.1%	PBAN 16.15%
	8 μ m	23.2%			
MC-172	200 μ m	26.8%	68%	5 μ m 20% (AFCAM)	HTPB 12%
	14 μ m	20.4%			
	6 μ m	20.8%			
T-48	48 μ m	70%			HTPB 30%
CMDB	FZO ₁	Double Base, HMX 56%			

Table III A-2 Results of Comparison of
Propellants and Transducers

Propellant	Transducer (BBN)	Burn Rate (in/sec)	Average Pressure (psi)	Sound Pressure Level db re.0002 dy/ cm ²
MC-170	376A	.39	333	91
MC-170	376LF	.52	353	105
UTP-3001	376A	.39	338	93
UTP-3001	376LF	.37	338	90
CMDB	376A	.175	328	78.5
CMBD	376LF	.179	336	77.5

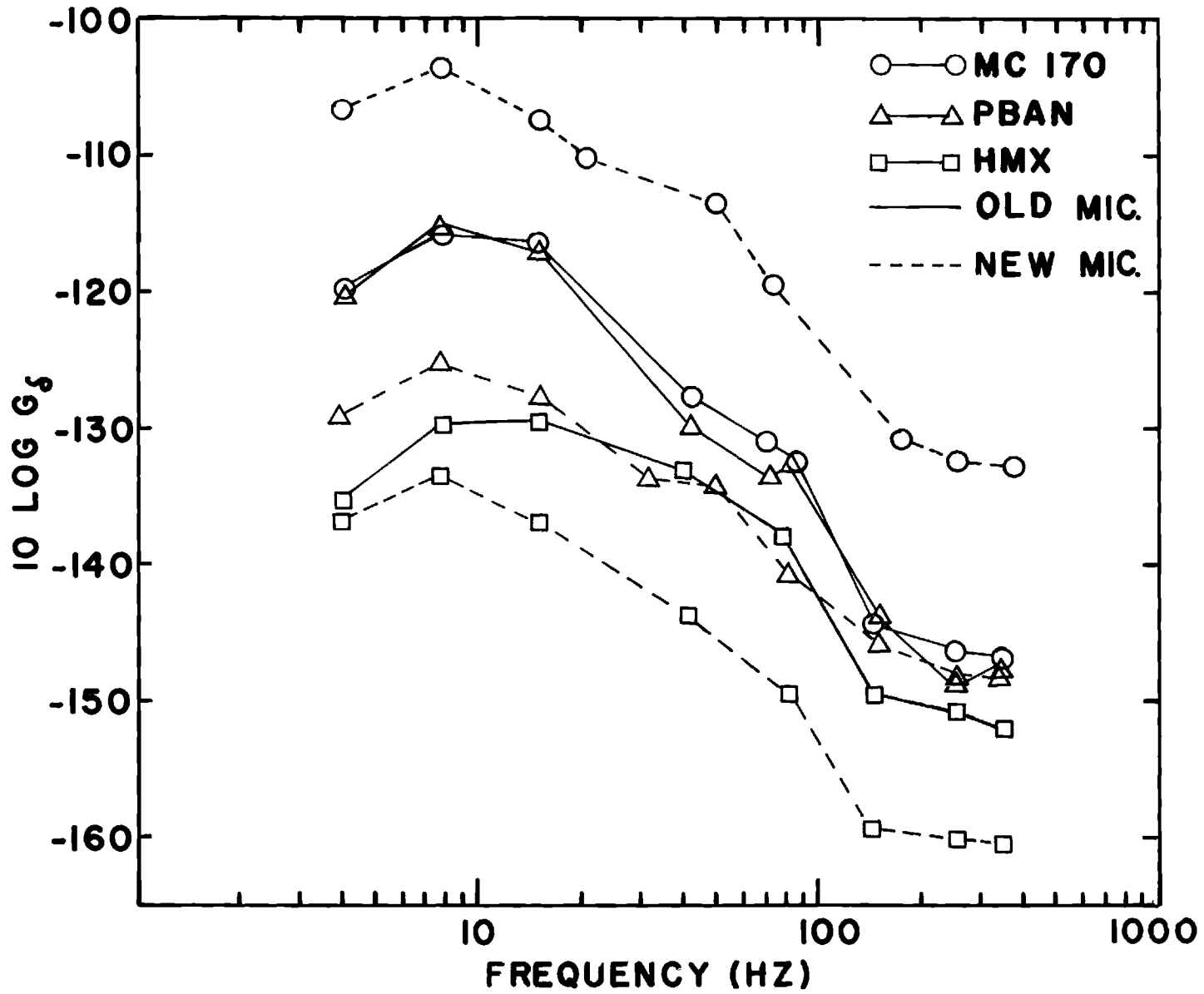


Figure III A-7. Strength of the Combustion Noise Source.

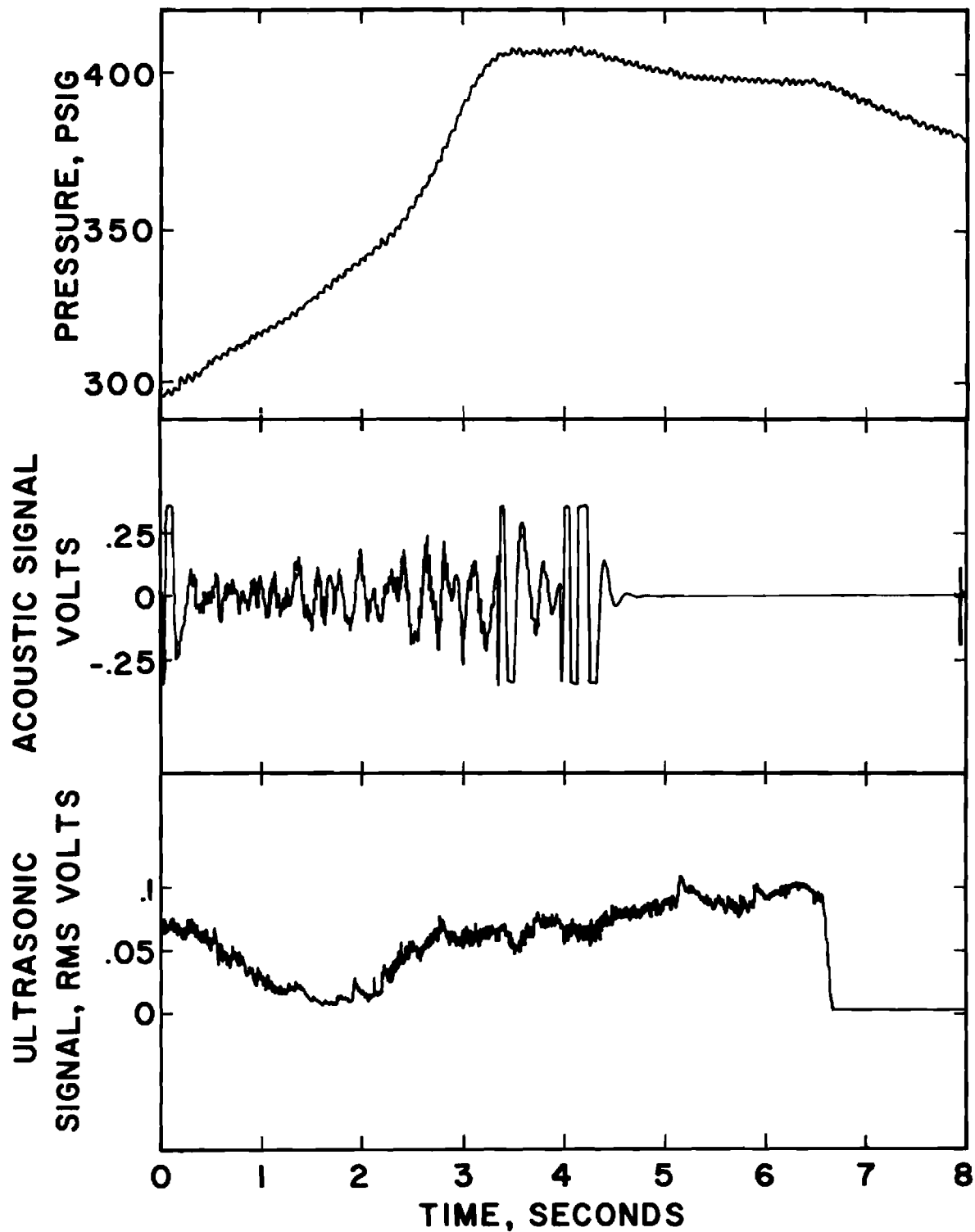


Figure III A-8. Time History for MC-170 using BBN 376 LF Microphone.

tests using the new transducer (376LF) in this series. All Fourier analysis was performed on the portion of the trace before any transducer saturation occurred. The first point, at 4 Hz, shown in Fig. III A-7 is in error since the signal was passed through a high pass filter set at 5 Hz before it was amplified and recorded. Additional tests were scheduled to obtain pressure spectra at lower frequencies (i.e. less than 5 Hz).

A series of eight direct noise tests were completed using both MC 170 and MC172. The results presented here are for MC 172, which is very similar to MC 170 (see Table III A-1). Three of the tests were conducted using various amplifier gains with the low frequency transducer, BBN 376LF. No useful data were obtained due to tape recorder, amplifier, and transducer saturation for all values of gain used. The next four tests were conducted using another type of piezoelectric transducer, AVL type 8QP500 ca. It was thought that this transducer and associated charge amplifier would have a better low frequency response and recover from saturation conditions faster. This was not obvious after the Fourier analysis of the resultant tests.

The final test of this series used the BBN, 376LF, low frequency transducer with a modified power supply. The current regulating diode was replaced with a factory supplied diode to allow for higher transducer currents. This increased battery drain, and it did improve the low frequency response and recovery. The pressure spectral level is shown in Fig. III A-9. The signal due to combustion was at least 35 db higher than the background measurements over the 1.6 to 30 Hz range. This separation of the low frequency spectra was visible at reduced gain with a high pass filter blocking the DC to 1 Hz signal. It was also present in the last test using the AVL transducer but the separation varied from 5 to 10 db over the 1.6 to 50 Hz region. The major result,

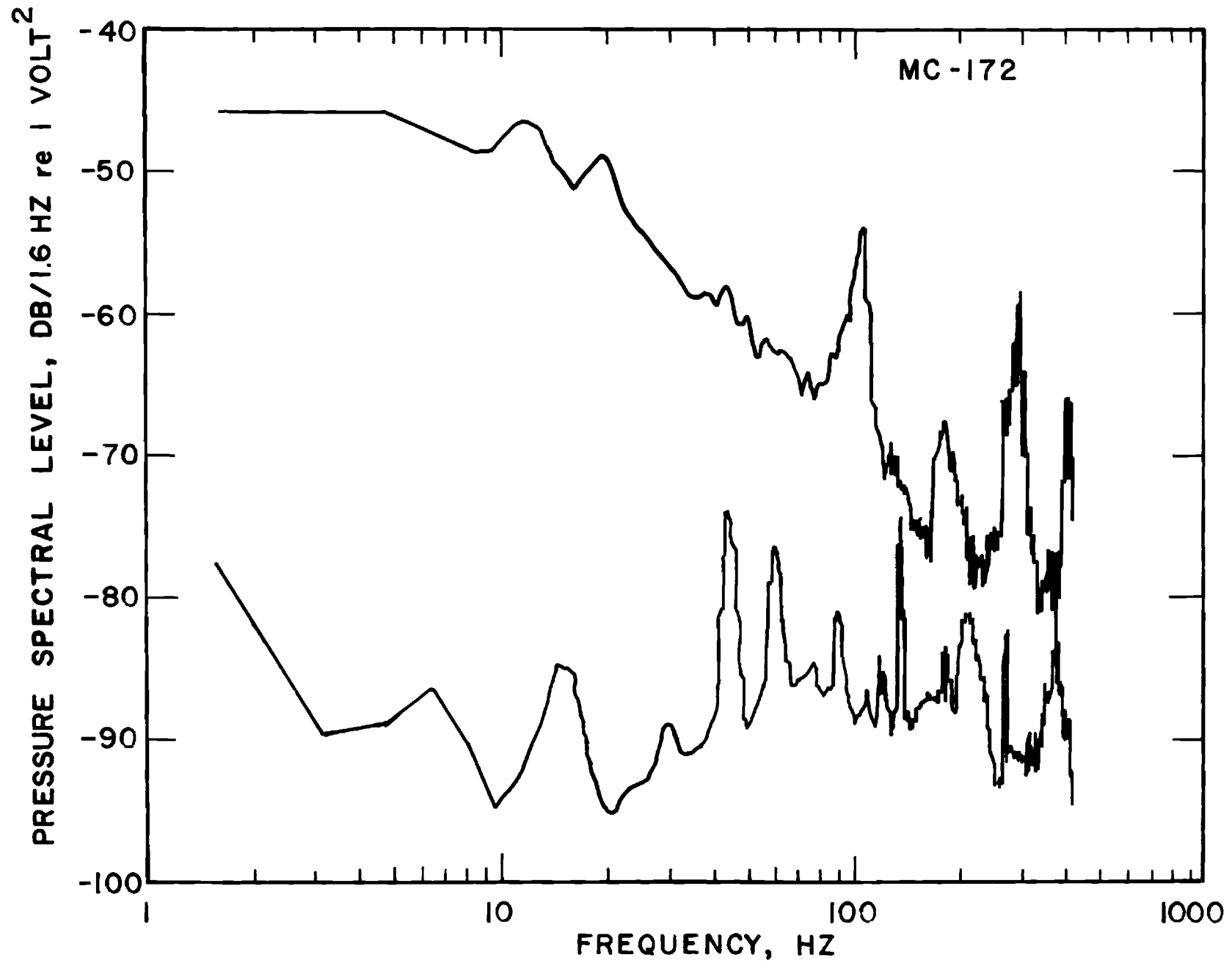


Figure III A-9. Pressure Spectra for MC-172 extending from 1.6 to 410.

when the very low frequency data was obtained, was that there was no surprise at low frequency. The noise spectra level off as zero frequency is approached. No further direct noise tests were conducted, since the magnitude analysis showed that the overall level of noise was too low to be important to the vibration problem for the propellants tested.

B. Cross-flow Effects on Combustion Noise

The object of the experiment was to measure the combustion noise from a process where there was a combustion and flow interaction. This effect has been explicitly excluded from the theory and it was desired to know the magnitude of the error involved. An erosive burning environment was simulated. It was necessary to have a thin sample and short burn time due to the finite volume of the acoustic tube. The sample volume was the same as the strand volume used in determining the direct combustion noise.

The sample holder was constructed to hold two $\frac{1}{4}$ " x $\frac{1}{4}$ " x $1\frac{1}{2}$ " strands (6.35 x 6.35 x 38.1mm) with a separation of up to $\frac{1}{4}$ " between the strands. This holder is shown in Fig. III B-1. Two types of tests were conducted using this U-shaped stainless steel sample holder. Atmospheric tests with plexiglas sides on the sample holder were conducted to obtain motion pictures of the burning samples. These movies allowed surface area - time histories to be obtained. Stainless steel sides were used when the samples were burned at 300 psi in the acoustic tube. The assembled sample holder for the pressure tests is shown in Fig. III B-2.

The initial assumption was to design the U-shaped channel so that the exit Mach number of the hot gases would be 0.5, if the sample burned normal to the $\frac{1}{4}$ " direction uniformly. It was hoped that by controlling the amount of ignitor paste the initial burning surface area could be controlled. Using available thermochemical equilibrium data for the UTP 3001 propellant, the

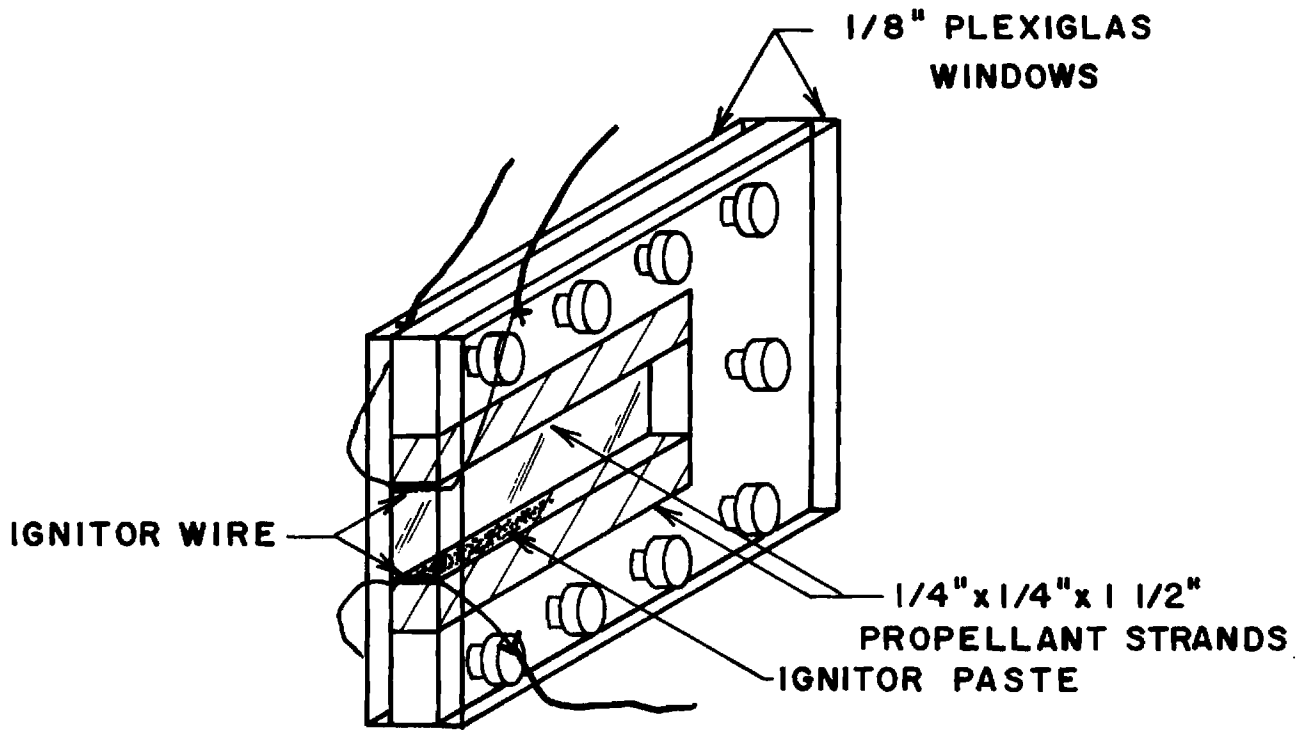


Figure III B-1. Apparatus to Test Combustion-Flow Interaction.

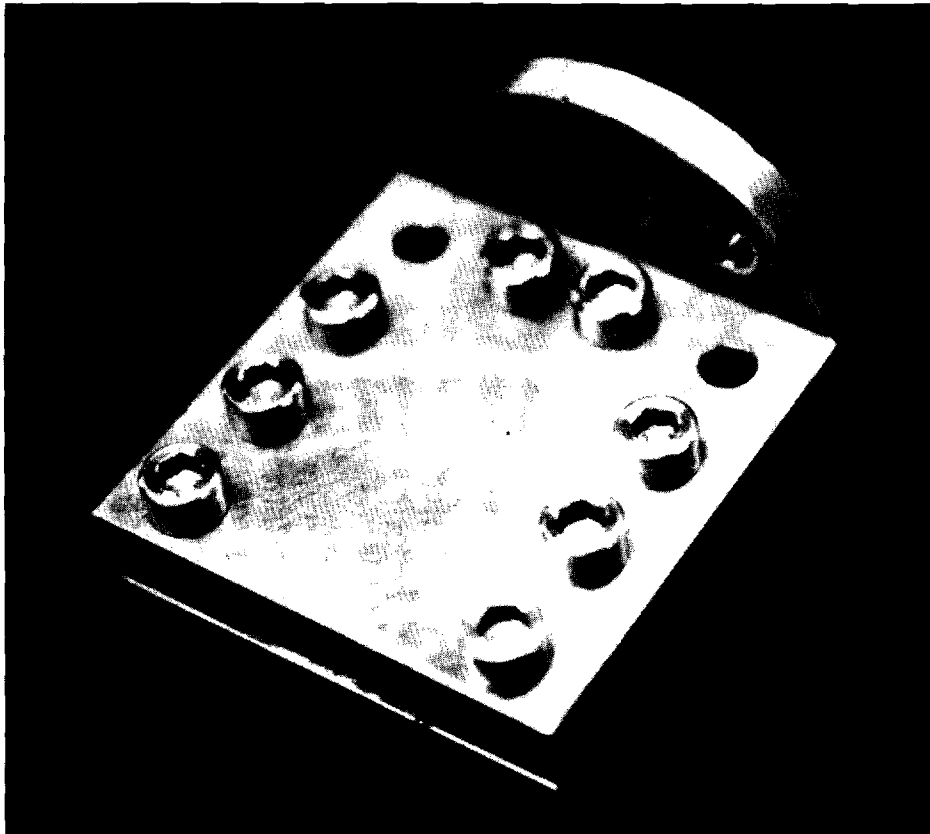


Figure III B-2. Sample Holder for 300 psi Combustion-
Flow Interaction Tests.

initial flow area was calculated. The stagnation temperature of 5382°R gave a speed of sound of 4102 ft/sec in the propellant product gases. A realistic burn rate from strand tests was .35 in/sec. In order to obtain a Mach number of 0.5 at the exit plane of the U-shaped channel, the initial sample separation of the two strands should be 0.057" (1.45mm). This initial channel was machined to allow for a $\frac{1}{4}$ " (6.35 mm) separation. This large separation was taken up with a $\frac{1}{4}$ " x $\frac{1}{4}$ " x $1\frac{1}{2}$ " (6.35 x 6.35 x 38.1mm) steel spacer.

A series of six atmospheric tests were conducted using the cross flow hardware to obtain motion pictures of the burning profiles through the plexiglas windows. A non-aluminized AP-HTPB propellant, T-48, was used in these tests. The presence of metal would obscure the motion pictures. The first two tests were unsuccessful because of extensive time delay in the sample ignition and high camera speed. In the third test the amount of ignition paste was increased and the camera slowed down to 500 fps from 800 fps. This sample started burning on the end and burned for 45 seconds. The sample stopped burning $\frac{1}{4}$ " from the end of the U-shaped channel. The ignition paste layer appeared to remain intact. For the fourth test the sample separation was eliminated and a minimum amount of ignition paste was used. This again resulted in an end burning sample. The fifth and sixth samples were successfully burned. The strands were tapered slightly to give an exit separation of .0625" (1.59mm). Sample frames from the movies of these tests are shown in Fig. III B-3. The side profile of the fifth sample is shown in Fig. III B-4. Assuming that the sample burned uniformly across the width of the U-shaped channel, the area as a function of time was calculated. This is plotted in Fig. III B-5 along with the associated correction factor to be added to the acoustic signal obtained from burning strands. According to theory, if there is no cross-flow effect, the amount of noise should scale linearly with the burning area.

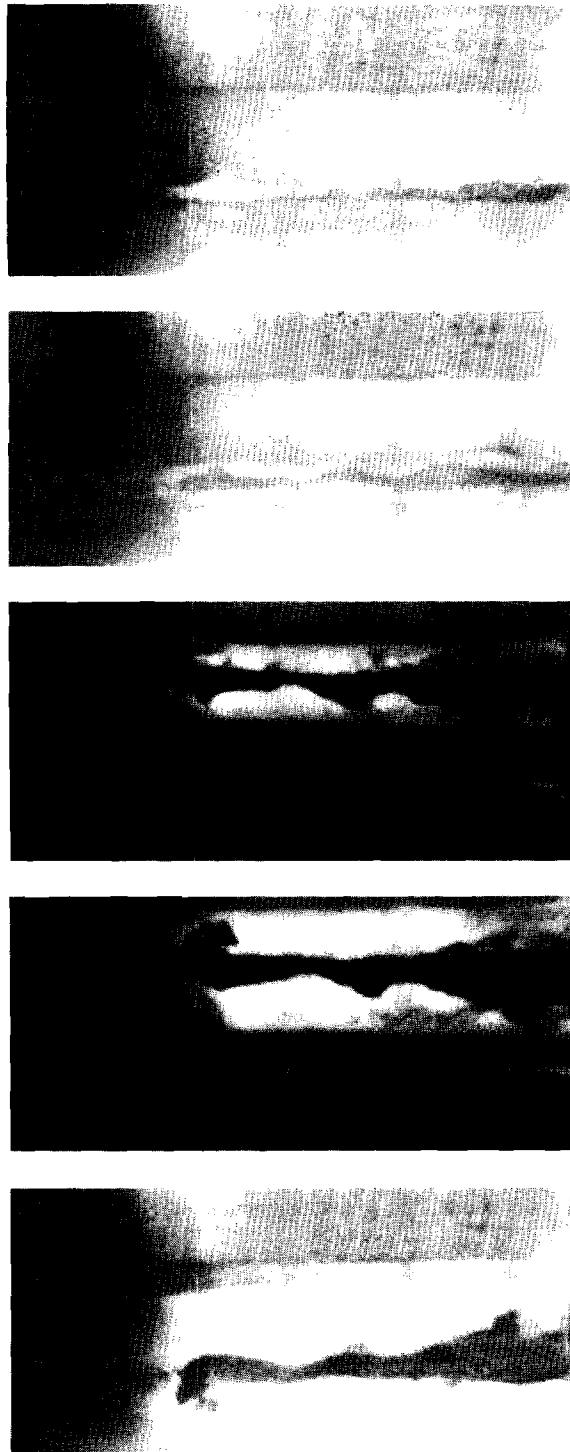
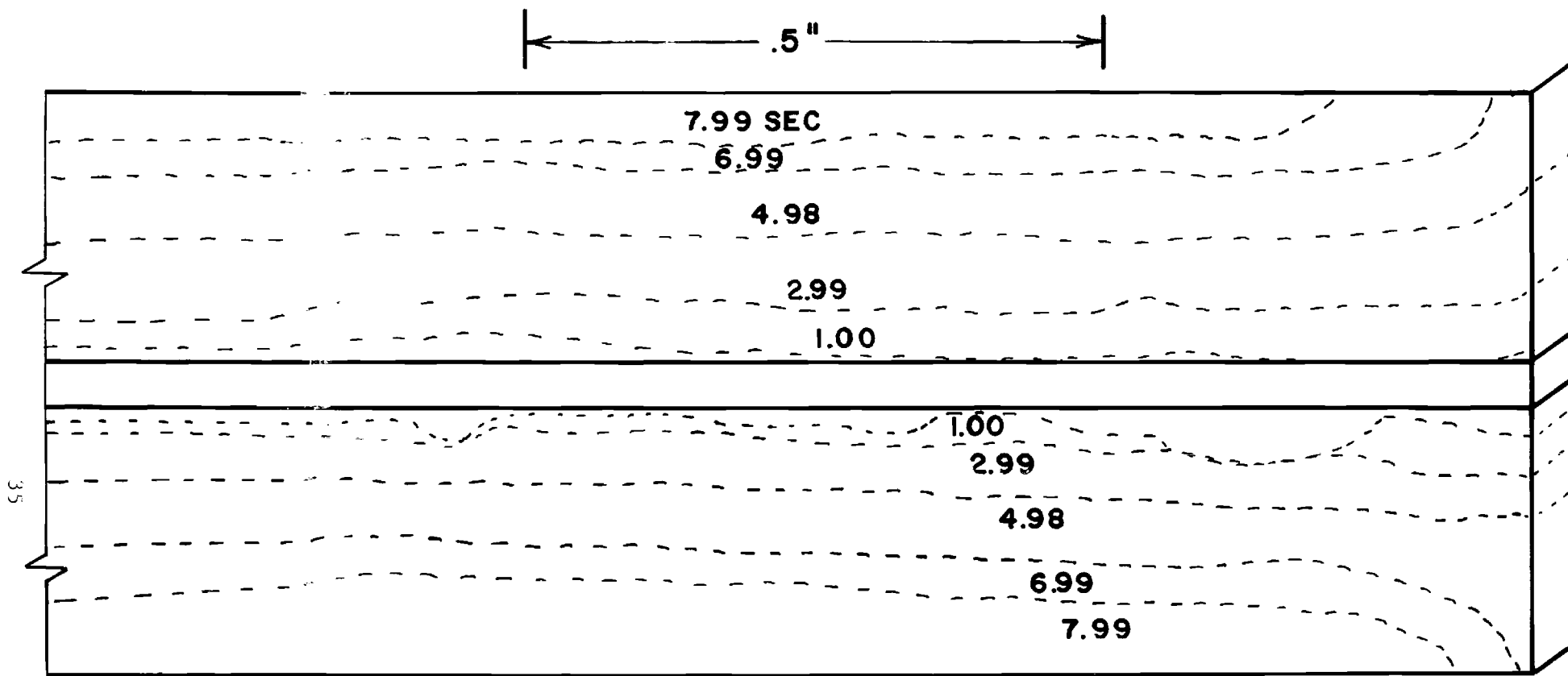


Figure III B-3. Combustion-Flow Interaction Side Profiles.



PROPELLANT BURNING SURFACES

Figure III B-4. Time History of Burning Surface Positions
for T-48 at Atmospheric Pressure.

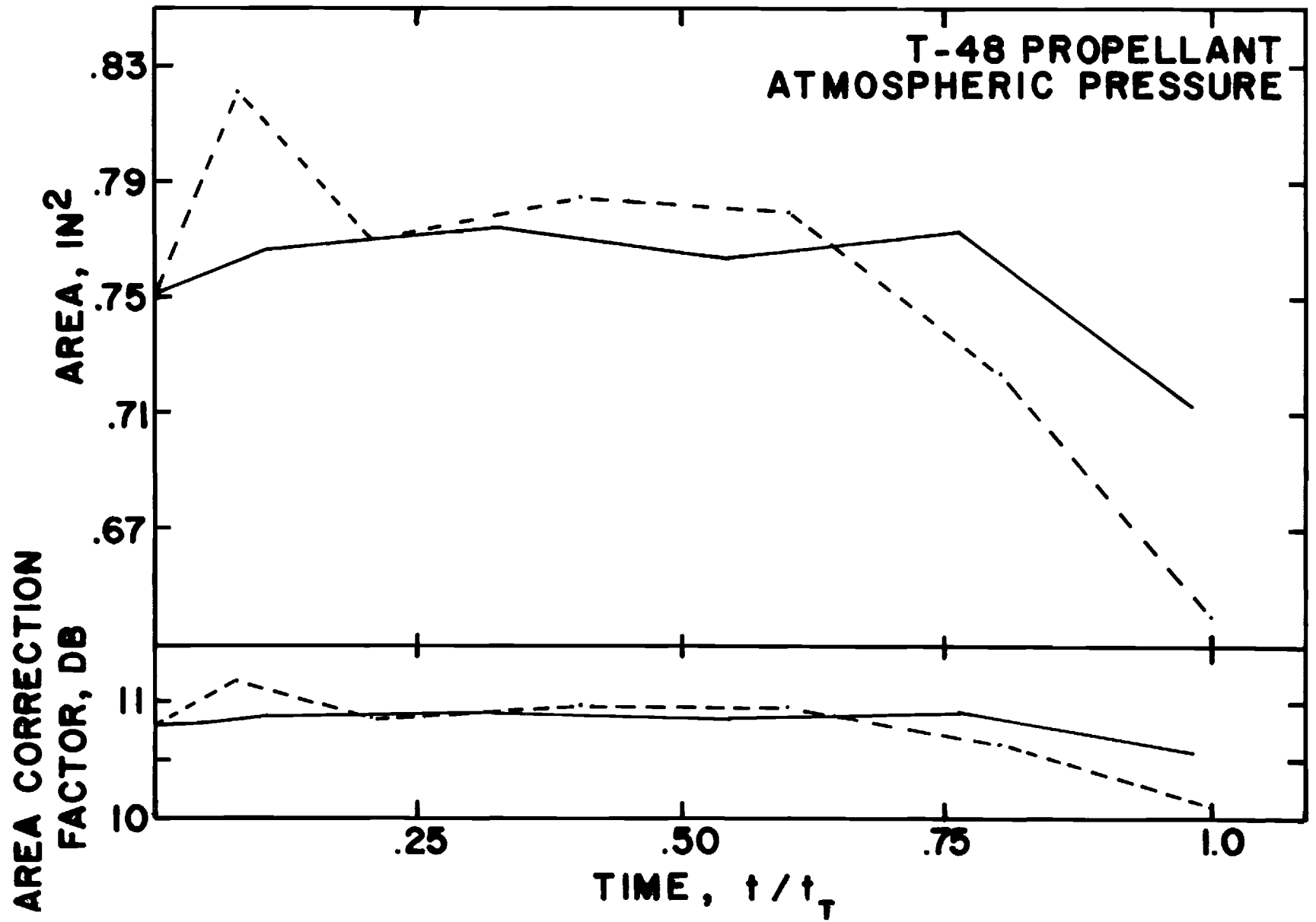


Figure III B-5. Time History of Area Correction Factor.

Direct combustion noise was then measured at 300 psi using the MC-170 and T-48 propellant. The U-shaped sample holder with stainless steel sides was used for these tests. The samples were prepared in exactly the same manner as for the two successful movies. The resultant sound pressure levels are listed in Table III B-1 along with the corresponding strand results. The samples in the channel burned slower than the corresponding strands. This could be due to a quenching or heat transfer effect of the stainless steel walls as opposed to the silicon rubber inhibitor on the strand samples. The samples with cross-flow generated more direct noise than the strand as was expected, due in part to the larger burning surface. Even when the nominal correction of 10.8 db from Fig. III B-5 is considered there is still a 7 to 7.5 db increase in the sound output. This is interesting, but it is found in the following section the noise is still too low to be of importance in the vibration problem.

The acoustic signal for the T-48 strand and U-shaped channel are shown in Figs. III B-6 and 7. The RMS value of the acoustic signal was obtained by playing the recorded signal back through a Hewlett Packard model 3400A RMS voltmeter. The tape recorder speed reduction and the time constant of the meter gave an effective time constant of .25 sec. The sound pressure level was consistently decreasing for the strand results in Fig. III B-6. This is as the tube pressure and temperature were increasing. For the sample with cross-flow the sound pressure level was constant over most of the test, or increasing slightly. The sound pressure level for both tests varies within a band of 2 to 3 db. The only change in the correction due to area fluctuations shown in Fig. III B-5 would be near the end of sample burning and would still be too small to make a meaningful shift in the trend of the sound pressure history to agree closer with the strand result. It must also be kept in

Table III B-1. Sound Pressure Levels for Combustion Flow Interaction Tests.

	TOTAL BURN TIME, SEC	BURN RATE IN/SEC	SPL DB
MC-170			
1/4" x 1/4" x 3.5" STRAND	9	.39	119.0
2 - 1/4" x 1.5" CHANNEL	1.2	.21	137.3
T - 48			
1/4" x 1/4" x 3.5" STRAND	8.7	.40	106.4
2 - 1/4" x 1.5" CHANNEL	1.6	.16	124.2

CHANGE EXPECTED DUE TO INCREASE IN BURN AREA = 10.8 DB

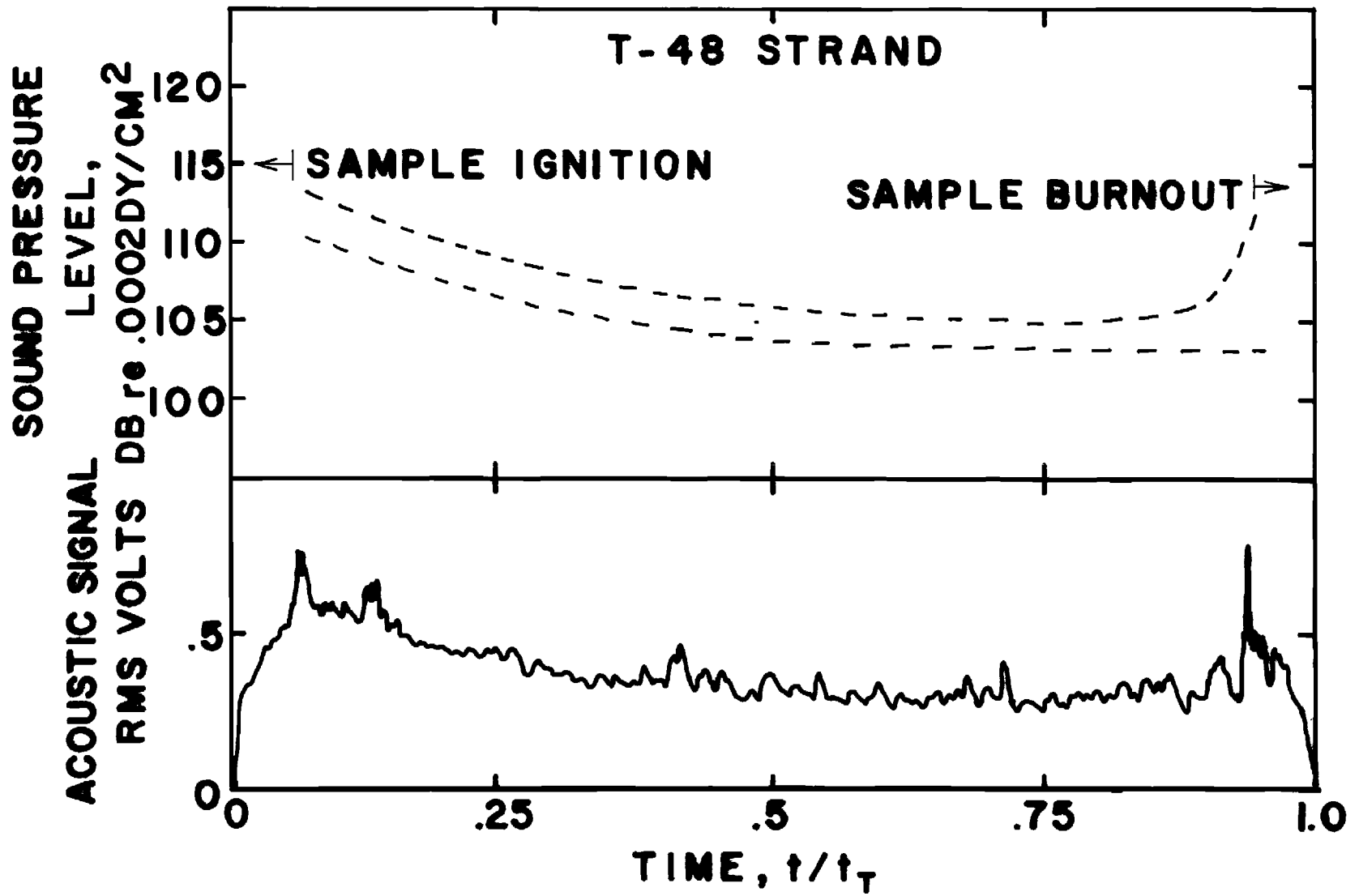


Figure III B-6. Sound Pressure Level History for Strand Test.

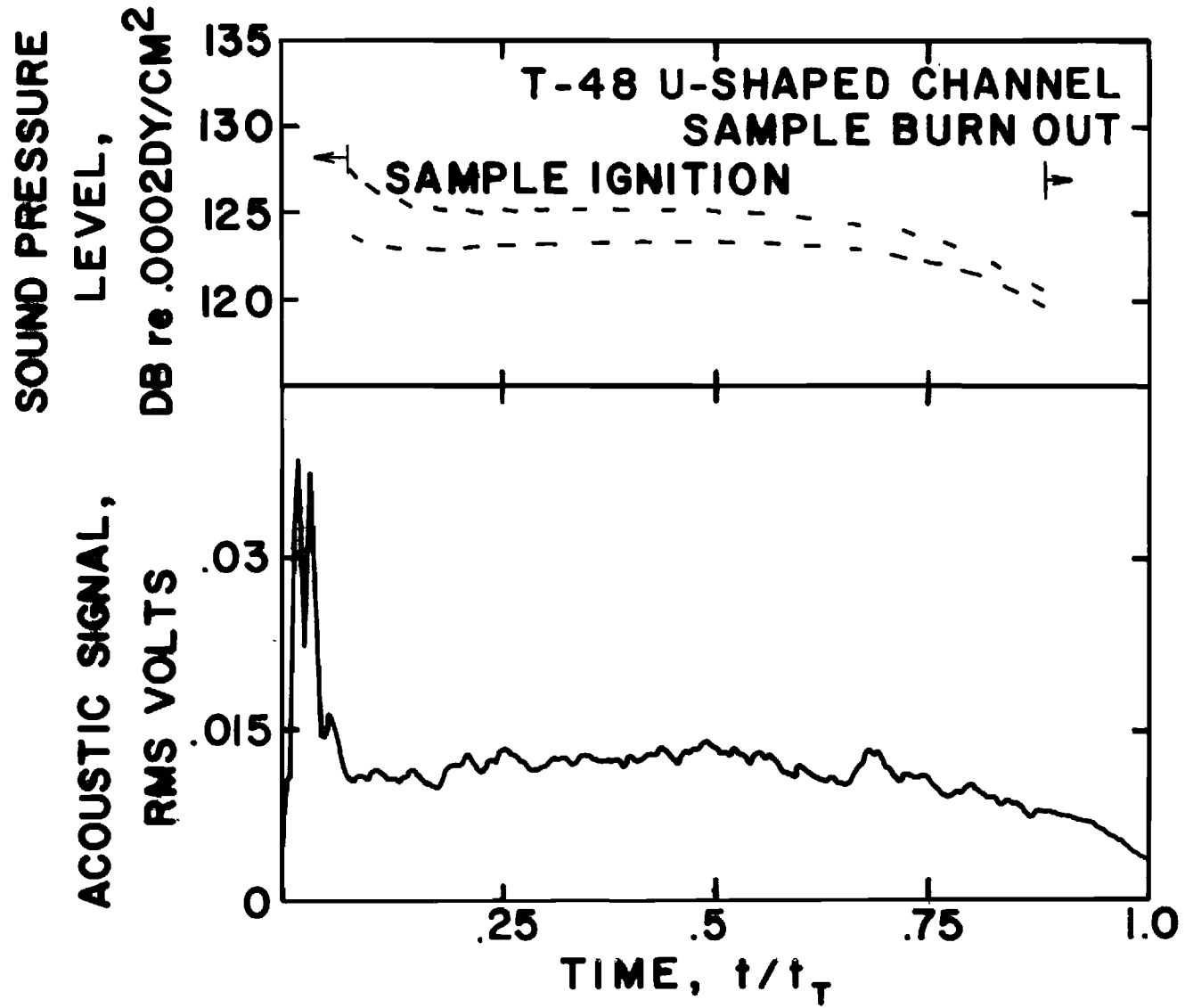


Figure III B-7. Sound Pressure Level History for U-shaped Channel Test.

mind that if the cross flow samples burned as fast as the strands there would be an even larger difference in the sound pressure level than 7 db.

Since the burn rate was down by a factor of two over what was assumed in the design of the crossflow hardware, the Mach number and Reynolds number based on the strand separation at the end of the Flow channel were recalculated. These calculations are included in Table III B-2. The exit Mach number was less than .26 for all conditions while Reynolds numbers indicated a definitely laminar flow.

These tests indicate that perhaps a significant weakness of the theory could be in a neglect of cross-flow effects in noise generation near the propellant surface. Further quantitative work in this area is required.

C. Temperature fluctuations

It was desirable to gain an estimate of the level and spectral content of the temperature fluctuations existing in the products of combustion of solid propellants. Such an estimate is directly required to estimate terms II_b and III in Eqs. (4). This was a difficult task because the temperatures are extremely high and any thermocouple small enough to respond to any small scale fluctuation would be susceptible to condensed phase product impact. Previous tests had indicated that temperature measurements could be made by burning the solid propellants in a plexiglas tube and using a thermocouple located near the wall, where it would measure the temperature of a cooled mixture of product gases and wall ablation product gases [Ref. (11)].

The initial test configuration consisted of a .5" (1.27 cm) inside diameter plexiglas tube with a .125" (3.2 mm) wall thickness. The initial tests were to be conducted at atmospheric pressure with a non-aluminized propellant. It was decided to use a Chromel-Alumel thermocouple that was commercially

Table III B-2 Exit Mach No. and Reynolds No. Values
for Combustion - Flow Interaction Tests

Propellant	Initial				Final			
	Separation	Mach No.	Velocity	Reynolds No.	Separation	Mach No.	Velocity	Reynolds No.
MC-170	.0625.in.	.26	1060 ft/sec	313	.5 in	.031	130 ft/sec	304
T48	.0625	.17	640	228	.5	.022	81	280

available in a .001" diameter wire. This type of thermocouple had a relatively fast time response, i.e., a short time constant. It had been used in previous tests to measure temperature fluctuations in a can combustor [Ref. (12)]. Techniques had been developed to correct the power spectral densities obtained from these thermocouples considering the time constant of the individual thermocouples [Ref. (12)]. This type of thermocouple will withstand a temperature of 1372°C (1605°K) with a thermoelectrical output of 54.875 millivolts when the reference junction is maintained at 0°C. This means that the distance above the burning surface and the distance from the wall must be controlled to prevent thermocouple destruction in every test, since the final temperature reached in adiabatic combustion would be on the order of 2500°K to 3000°K. A .097" (2.46 mm) ceramic cylinder was placed in the flowing hot gas to deflect any condensed material away from the thermocouple. This temperature fluctuation measuring apparatus is shown in Fig. III C-1. The length of the .5" (1.27 cm) diameter propellant sample was chosen to allow the thermocouple to reach an equilibrium value. A .25" (6.35 mm) height was sufficient for the atmospheric tests, while 1" (2.54 cm) height was used for the tests at 300, 600 and 900 psi. A photograph of a nonaluminized sample is shown in Fig. III C-2.

The flow pattern around a circular cylinder changes as a function of Reynolds number ($Re = \frac{\bar{u}d\rho}{\mu}$). For small Reynolds number the wake is laminar. As the Reynolds number increases a regular vortex pattern known as Kármán vortex streets are formed ($60 < Re < 5000$). At still higher Reynolds number the wake becomes turbulent. [Ref. (13)]. The frequency, f , at which the vortices are shed is related to the flow velocity and cylinder diameter by the Strouhal number, $St = \frac{fd}{u}$. The initial assumptions predicted a frequency of 2000 Hz. This was beyond the expected response range of the thermocouple

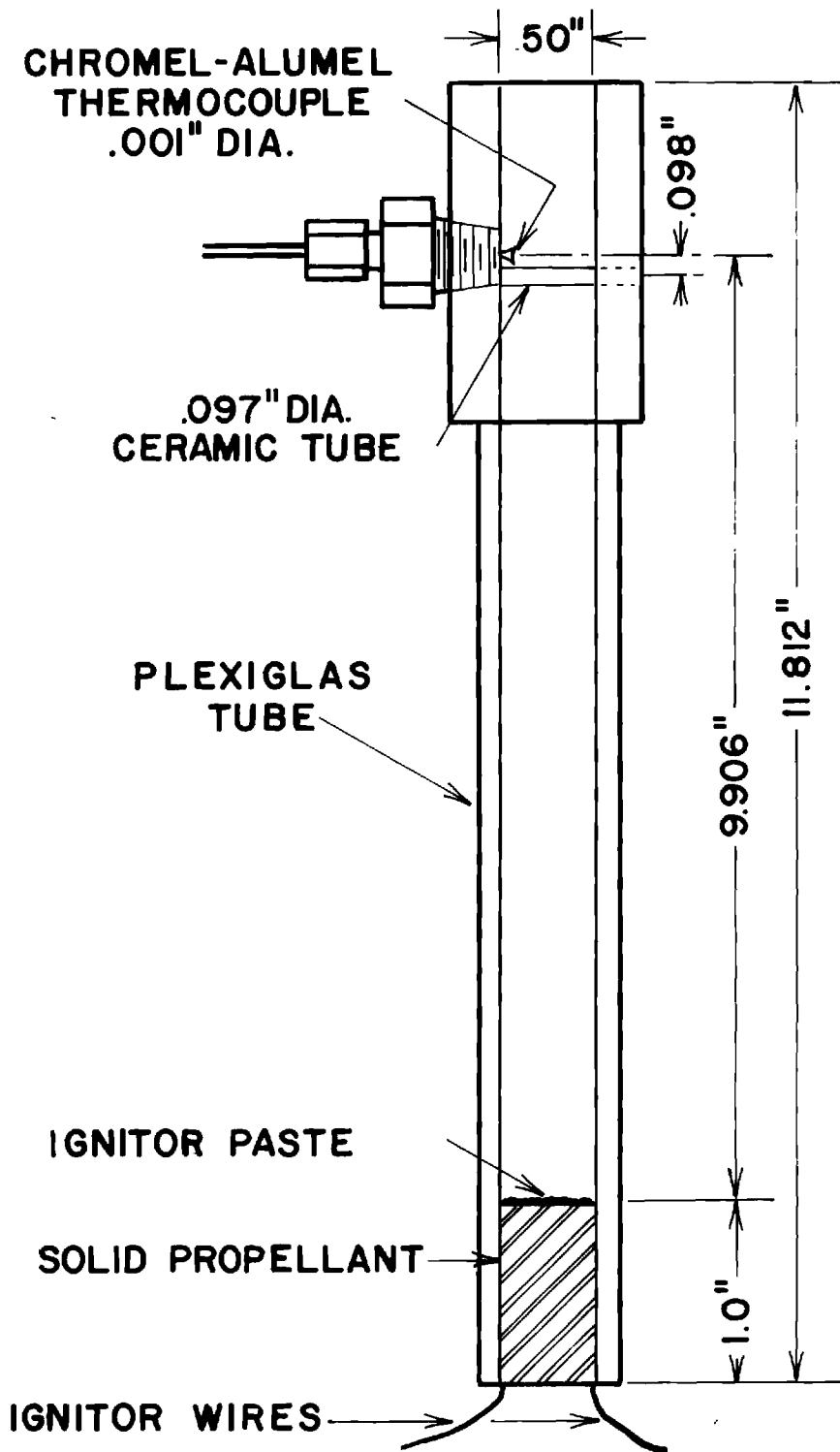


Figure III C-1. Temperature Fluctuation Test Apparatus.

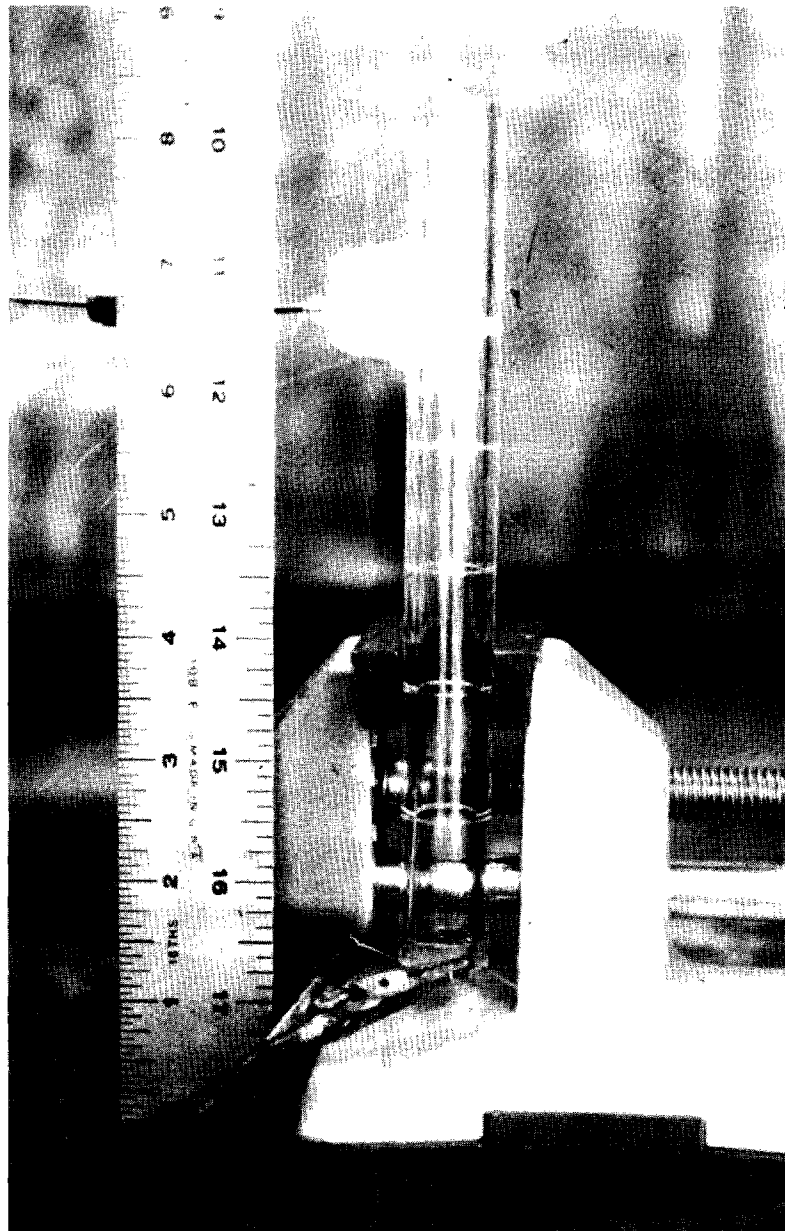


Figure III C-2. Photograph of Temperature Fluctuation Test Apparatus.

and no further consideration was given to this frequency. The post test calculations have yielded some different values which will be noted as the tests are discussed. The major assumption with this apparatus is that the wake filling and emptying time is short compared with a typical period of the fluctuations. Thus, the frequency content of the fluctuations should be small compared with the Strouhal shedding frequency.

An initial series of fourteen tests were completed using a non-aluminized propellant, T-48, at atmospheric pressure. The time histories of the thermocouple response were recorded on magnetic tape for reproduction and Fourier analysis. The thermocouple and its location was fixed for all tests in this series. The tube was shortened after each test. The first test that was completed was for a thermocouple located initially 3.9" (9.9 cm) above the burning surface. This thermocouple registered a maximum average temperature of 525^oK. The last test of the series was for the thermocouple initially located .27" above the burning surface. The temperature history for this run is reproduced in Fig. III C-3. The fluctuating component of the thermocouple response is also shown. This was obtained by passing the thermocouple signal through a high pass filter (Krohn-Hite model 3323 R) set to pass frequencies above 5 Hz. The upper limit imposed by the tape recorder was 30,000 Hz. The temperature history for one of these tests completed using an aluminized propellant, UTP-3001, at atmospheric pressure is shown in Fig. III C-4.

The RMS value of this fluctuation was obtained by two methods. It was passed directly through a Hewlett Packard model 3400 A RMS voltmeter or obtained by integrating the temperature spectral levels shown in Fig. III C-5. This latter method was preferred because the thermocouple response could be corrected for its individual time constant, as outlined in Ref. (12). The same problem that plagued earlier measurements of direct combustion noise

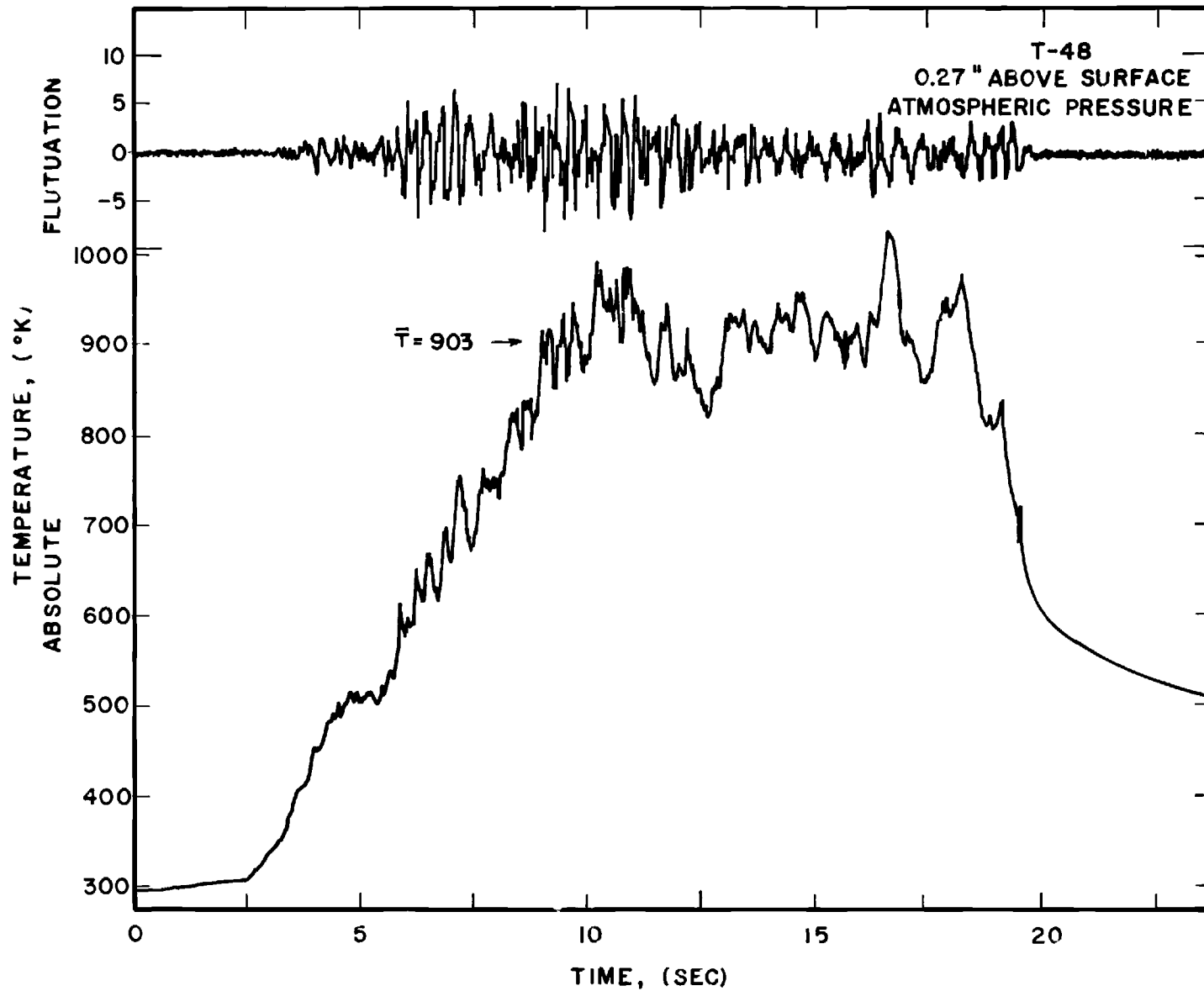


Figure III C-3. Temperature History for a Non-aluminized Propellant.

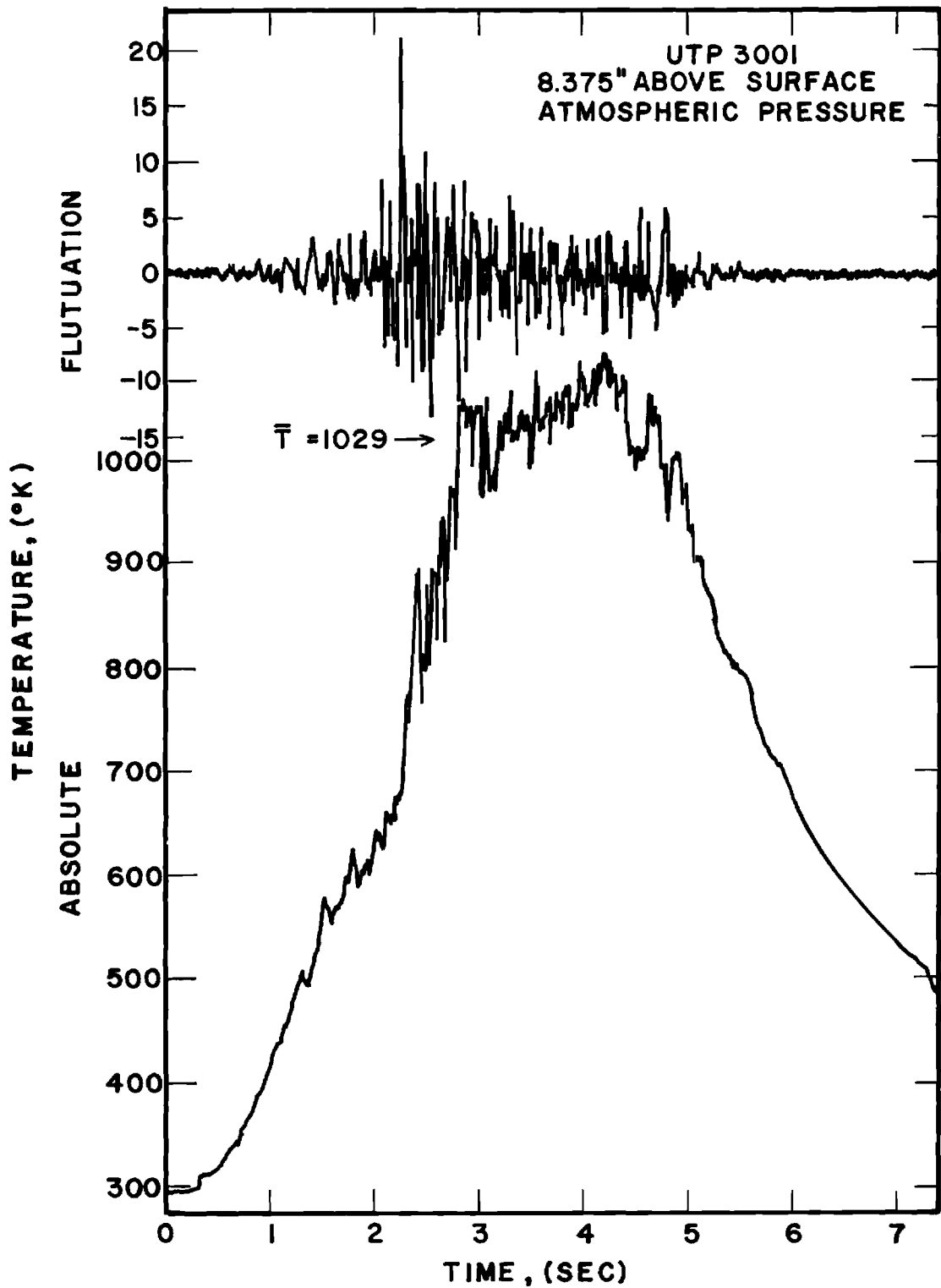


Figure III C-4. Temperature History for an Aluminized Propellant.

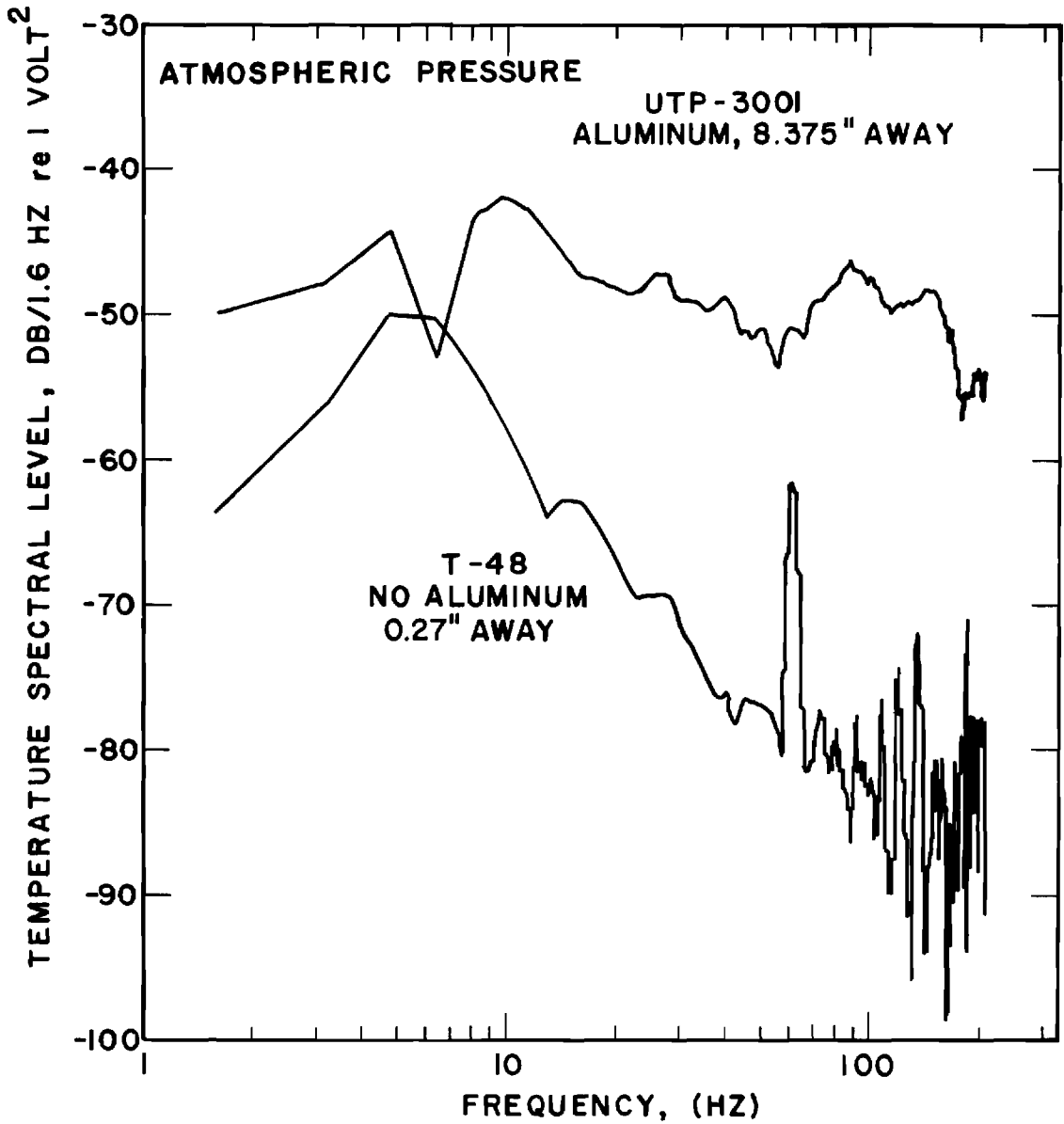


Figure III C-5. Temperature Spectra for Two Propellants.

reoccured when the same Krohn-Hite filter was used to high pass the temperature fluctuation signal. The 60 Hz signal and its harmonics were obvious in the low level temperature spectra. They were reduced to a lower level, as before, by subtracting background noise spectra. This correction was not as effective since the thermocouple output changed over a much larger range for an individual test than the pressure signal. The temperature spectra were corrected for both time constant and 60 Hz noise before the trace was integrated to give a representative RMS value of temperature fluctuation, T' .

The geometry of the test set up for T-48 non-aluminized propellant is indicated in Fig. III C-6 along with a representative average value of the absolute temperature of the gas passing over the thermocouple. The extremes of the fluctuations have been indicated. The non-dimensionalized RMS temperature fluctuation T' , divided by the average temperature, \bar{T} , is also shown as a percent. For the nonaluminized, atmospheric tests this fluctuation varied between .8 and 1.4%. The burn rate for these tests varied from .016 to .05 in/sec (.4 - 1.2 mm/sec). This was consistent with the burn rates obtained from the U-shaped channel atmospheric tests of the T-48 propellant.

The results for the absolute temperature, it's extremes and the per cent fluctuation for the aluminized propellant, UTP-3001, are shown in Fig. III C-7. This fluctuation varied from 4.4 to 6.9%. The burn rate for these tests varied from .05 to .06 in/sec (1.3 - 1.6 mm/sec). A photograph of the last test of UTP-3001 at an initial distance of 6.2" above the burning surface is shown in Fig. III C-8.

The burn rates for these tests were lower than that assumed in the initial calculations of Strouhal number and vortex shedding frequency. Considering a burn rate of .05 in/sec (1.2 mm/sec) at atmospheric pressure, the velocity of the product gas for T-48 (non-aluminized propellant) was 60 ft/sec (18.3 cm/sec).

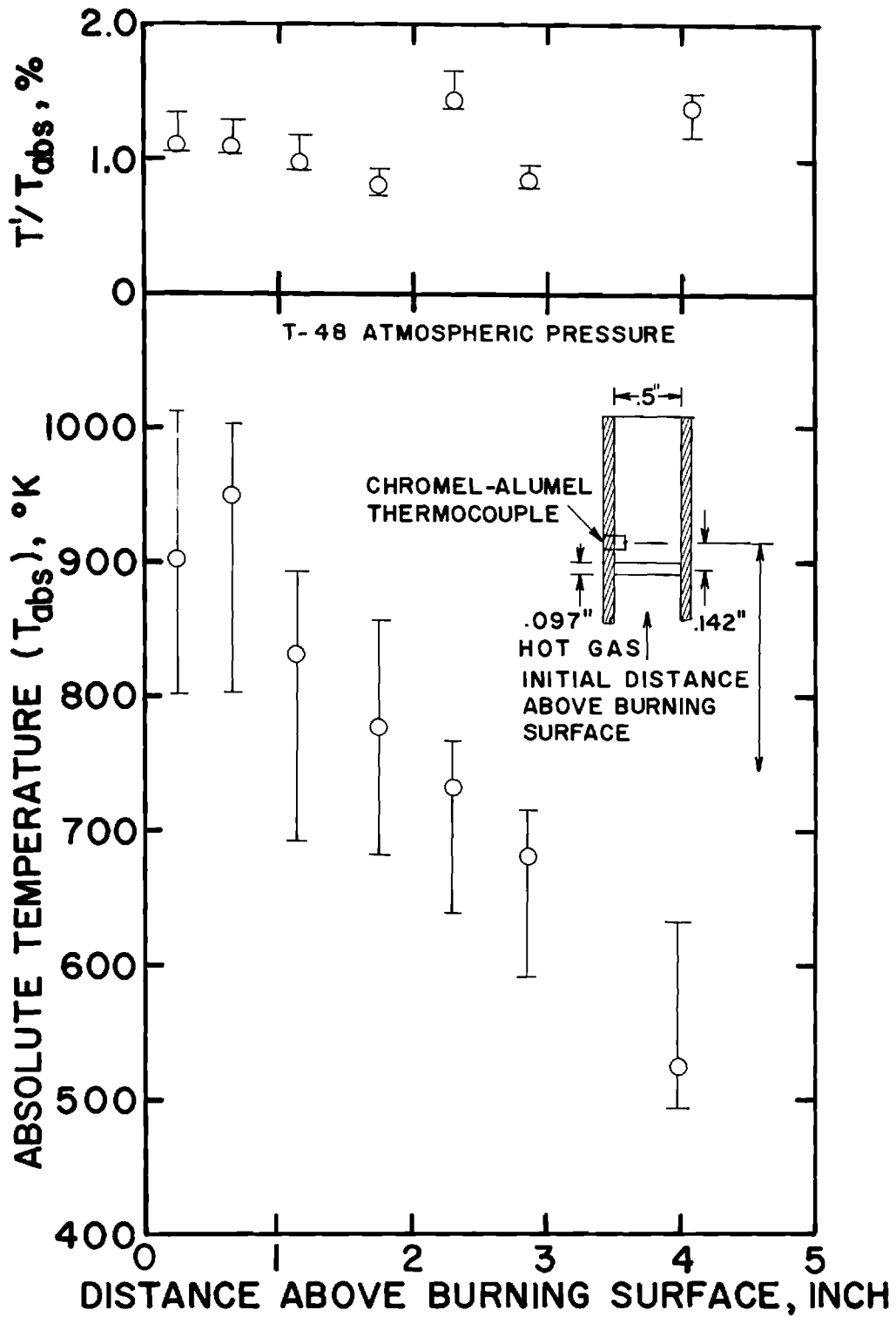


Figure III C-6. Temperature Measured above the Burning Surface of a Non-aluminized Propellant.

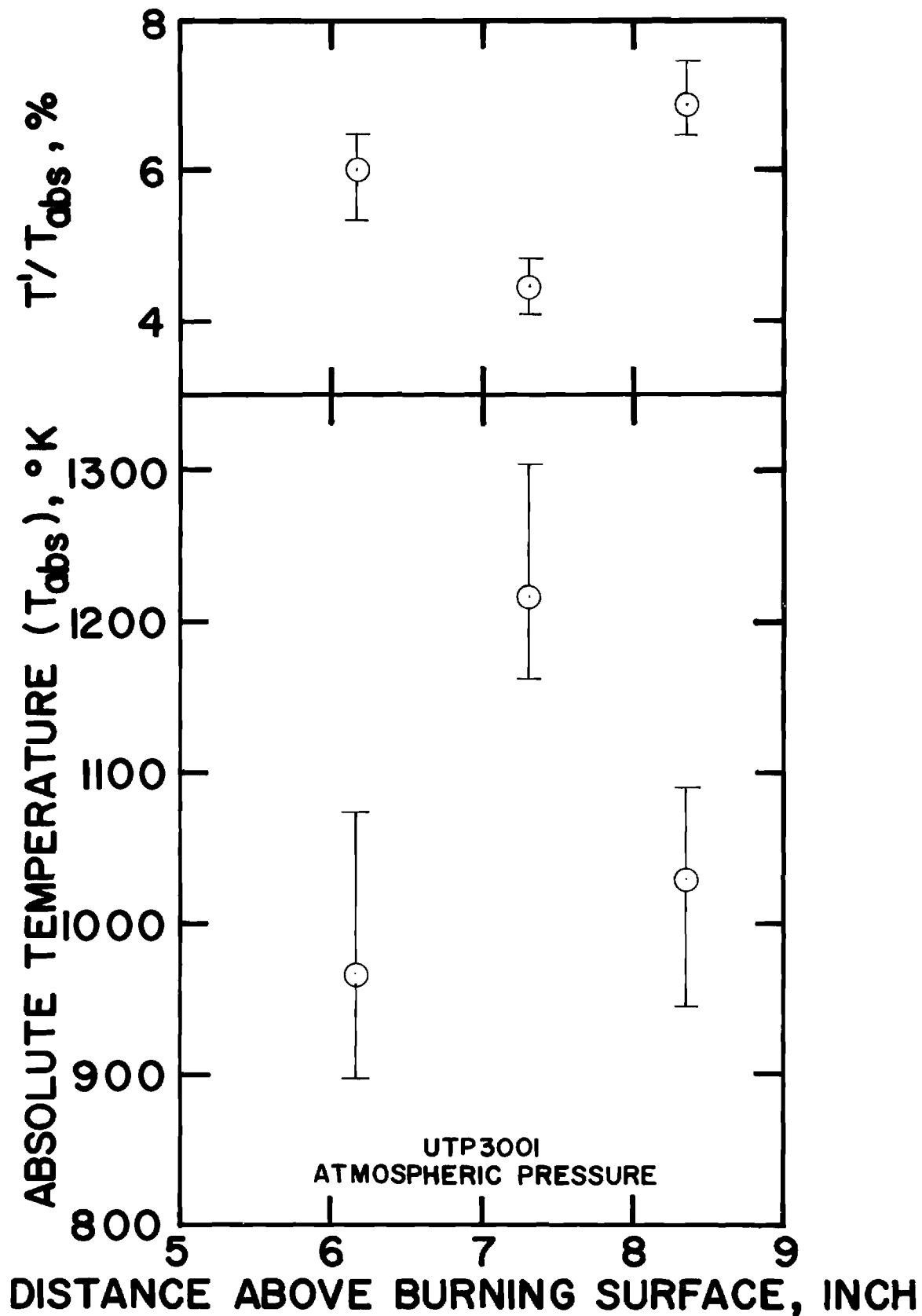


Figure III C-7. Temperature Measured above the Burning Surface of an Aluminized Propellant.

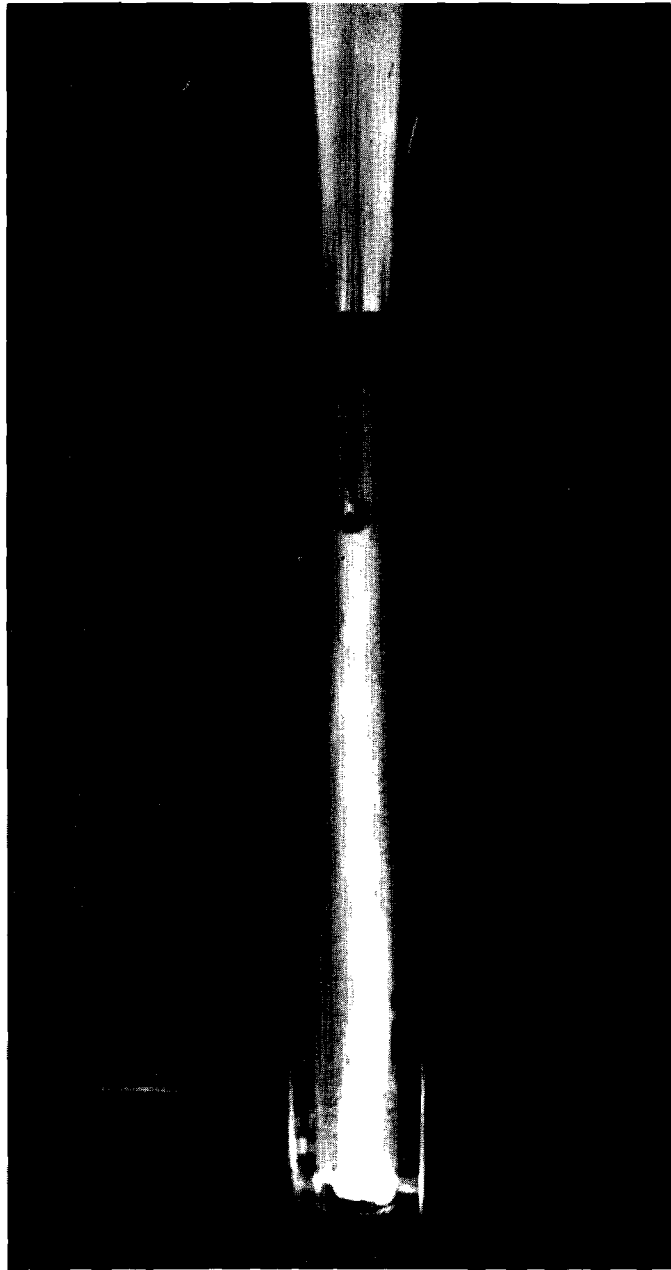


Figure III C-8. Photograph of Temperature Fluctuation Measurement of UTP-3001 Propellant, 6.2" away from the Surface.

The resultant Reynolds number was 1.6. This indicated a laminar flow well below the lower limit for the formation of vortices in the wake of the ceramic cylinder. For the aluminized propellant (UTP-3001), the flow velocity was up to 180 ft/sec (58.9 m/sec). The Reynolds number was 4.1 and the flow shown in Fig. III-8 should still be laminar with no vortices in the wake of the cylinder.

It was concluded from these tests that the temperature fluctuations in the product gases of the aluminized propellant were considerably higher than in the non-aluminized product gases. This was expected because of the burning aluminum agglomerates in the product gases. It was decided to conduct further test of the aluminized propellant at 300 psi.

The pressurized temperature fluctuation measurements were conducted in a nitrogen environment in the acoustic tube shown in Fig. III A-1. The sample was prepared and placed in a .5" (1.27 cm) inside diameter plexiglas tube as for the atmospheric tests. It was necessary to increase the sample height to 1" (2.54 cm) to compensate for the increase in burn rate as the pressure increased. This was necessary to obtain a sufficient temperature-time history for Fourier analysis. The plexiglas tube axis and the direction of the sample burn rate were now horizontal instead of vertical, due to the acoustic tube mounting system.

Two initial tests were conducted at a distance of 9.9" (25.1cm) away from the burning surface. Both thermocouples apparently reached an equilibrium temperature (1142^oK and 1385^oK) before failing. This was substantially below the upper limit of the Chromel/Alumel thermocouple (1645^oK). It was believed that failure was due to particle impingement. A new plexiglas tube was used for the remaining test. The length was increased to allow an initial separation of 24" (60.96 cm) from the thermocouple to the burning surface. Successful

tests were obtained at 24, 18 and 12" (61, 45.7 and 30.5 cm) The results for these three tests are shown in Fig. III C-9. The burn rate of these samples varied from .34 in/sec (.86 cm/sec) to 1.0 in/sec (2.54 cm/sec). The slow burning sample was for the test with 24" (61.cm) of separation between the thermocouple and burning surface. This sample definitely had problems reaching a steady state burn rate. The slow start of burn did not effect the resultant temperature measurements. The temperature fluctuation varied from 0.5 to 2.7% This was considerably below the values obtained in the open atmosphere tests shown in Fig. III C-7.

One atmospheric test was conducted using this same test configuration. The sample was burned in the acoustic tube that was flushed with nitrogen before the sample was ignited. The absolute temperature was consistent with earlier results, but the fluctuation was less than indicated in Figure III C-7. The temperature fluctuation due to after-burning of aluminum in a product gas mixing with nitrogen may be less than that produced when the product gas mixes with air.

The electrical treatment of the thermocouple signal was improved over the course of this experiment. All thermocouple cables and temperature compensation devices were electrically shielded. Ground loops and 60 Hz noise pickup were minimized by device and cable placement. The importance of the above precautions did not become known until this last phase of the investigation. This was consistent with the elimination of the high pass Krohn-Hite model 3323R electronic filter from the experiment.

Two more tests were conducted at 19" away from the burning surface at 600 and 900 psi. The absolute temperature and the temperature fluctuation have been included in Fig. III C-9. The temperature spectra of the 900 psi test indicated discrete frequencies at 700 and 820 Hz as shown in Fig. III C-10.

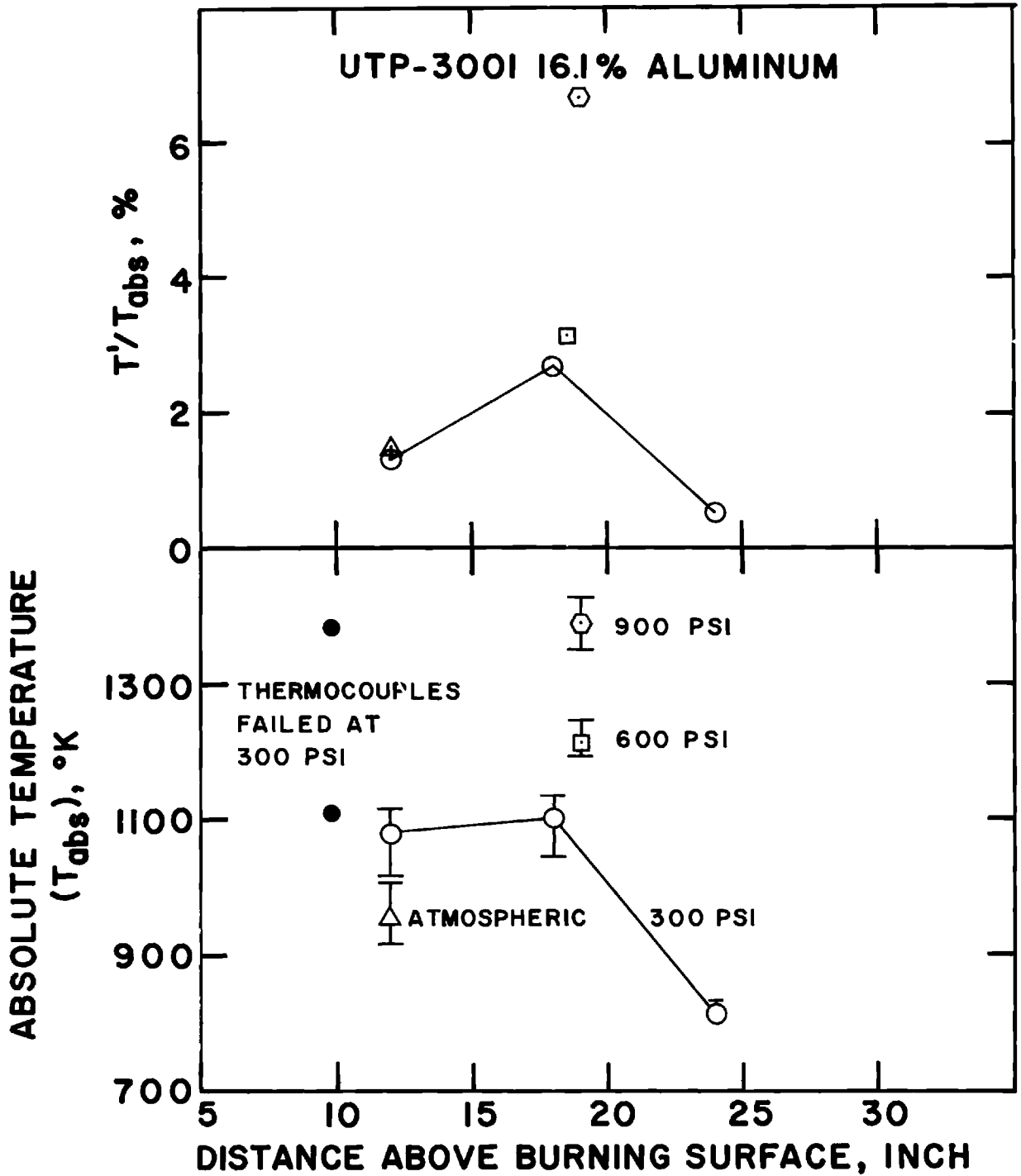


Figure III C-9. Temperature Measured above the Burning Surface of an Aluminized Propellant for Various Pressures.

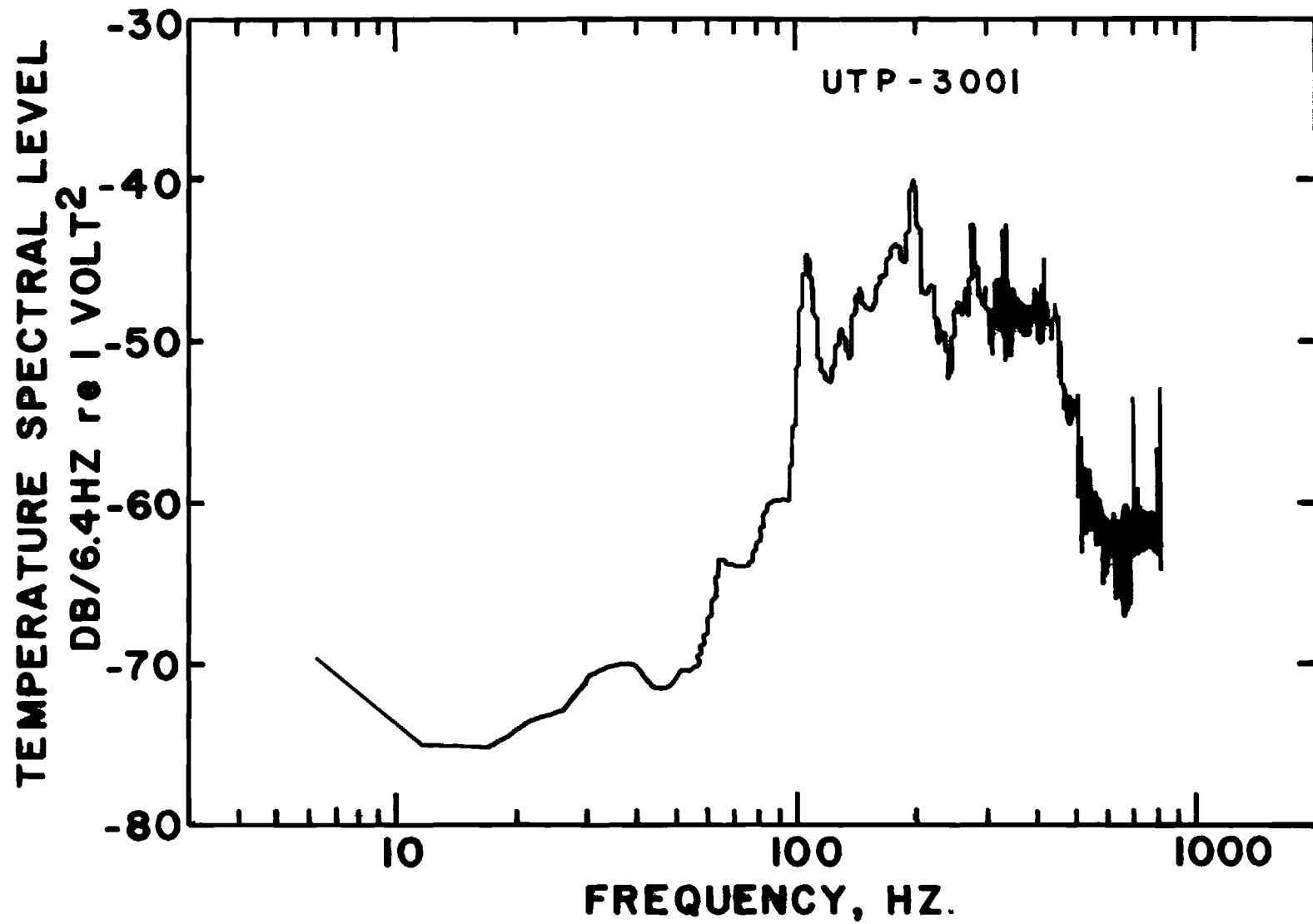


Figure III C-10. Temperature Spectra for an Aluminized Propellant at 900 psi.

This suggested the possibility of a vortex frequency. Calculations were made knowing the test sample burn rates and the results are summarized in Table III C-1. The resultant Reynolds numbers indicated that there could be discrete frequencies in four of the six tests. They were observed in the three tests where the maximum frequency considered in the Fourier analysis was greater than the frequency indicated by the Strouhal number calculation. The occurrence of more than one frequency is not surprising since the temperature spectra represents only 10 samples taken as the sample burns over 0.67 seconds. A change in velocity of $\pm 15\%$ would account for the different discrete frequencies indicated in this table. The major point, however, is that the peak in the temperature fluctuation spectra occur at frequencies well below the vortex shedding frequency. Consequently, the spectral shape and overall rms magnitude are believed representative of what would be seen if the protective cylinder were absent.

As will be seen in the next section, a typical distance between, say, 400 μm diameter burning particles is $2.4 \times 10^4 \mu\text{m}$. For the data appropriate to Fig. III C-10 the flow velocity was less than 50 ft/sec (less than because the gases have been cooled by the tube and are less dense than the calculated adiabatic flame value). Thus, an upper limit on the burning particle passing frequency is 690 Hz. This is the same ballpark as the region of maximum spectral density on Fig. III C-10. Moreover, it was observed in the experiment that as the pressure was lowered and the gas velocities consequently raised the frequency content shifted to higher values. These results are consistent with, but do not prove, that the temperature fluctuations are caused by convection of high temperature combustion fields past the thermocouple and these combustion fields are attached to the droplets. It is known that the burning metals carry their own diffusion flame with them in rocket

Table III C-1 Reynolds Number and Vortex Shedding
Frequency for Temperature Fluctuation Tests

Pressure (psi)	Burn Rate (in/sec)	Distance (in)	Velocity (ft/sec)	Re	f (Hz)	frequency indicated from Fourier A.
Atmospheric	.50	12	1040	475	26,900	~
300	1.0	12	33	15	~	~
300	1.0	18	101	47	1500	1720
300	.34	24	101	47	1500	~
600	.94	19	52	47	766	705, 820, 890
900	1.50	19	48	67	843	700, 820

environments, so that this source of the temperature fluctuations at a point is a plausible one. This is the view that will be adopted in the next section and is one which critically affects the outcome of the calculations.

Another point to notice is that the temperature fluctuation levels were not particularly high. Part of this may have been caused by the fact that the ceramic shield prevented full realization of the actual T' . On the other hand, thermochemically the temperature carried in the diffusion flame surrounding a metal droplet should be significantly higher than that of the surroundings so that higher T' values should have been seen. The explanation here, which is consistent with the current explanation of the T' source, is that there is such a large distance between droplets compared with a droplet (and flame) dimension that the rms value of T' is suppressed over its peak value.

IV. Order of Magnitude Calculations

As mentioned in Section II, the ultimate output desired is the mean square (or rms) pressure fluctuation and its spectral distribution on the chamber walls. The formulation in the Appendix is in terms of the density fluctuation. This may be converted to a pressure fluctuation by multiplication of c_e^2 in regions where σ_w is zero, as it is assumed at the head and nozzle ends. By Eq. (2) of Section II, the quantity $p_w p_w^*$ is desired and it has already been mentioned that an initial assumption of zero correlation between the various source terms of Eqs. (38) of the Appendix will be made. Consequently, except for numerical factors, the G's of Eq. (3) of Section II are made up of c_e^4 times the square of the individual numerical terms of Eqs. (38) of the Appendix. Consider the following manipulations of each of these:

$$c_e^4 I_a I_a^* = K^2 K^{*2} \left(\int_V g_w (T_{11})_w dV \right) \left(\int_V g_w^* (T_{11})_w^* dV \right)$$

$$\begin{aligned} &\approx k^4 \int_V \int_V dV(y_i) dV(\xi_i) g_{\omega}(x_i, y_i) g_{\omega}(x_i, \xi_i) [T_{11}(y_i)]_{\omega} [T_{11}(\xi_i)]_{\omega} \\ &= k^4 \int_V dV(y_i) \int_V dV(\eta_i) g_{\omega}(x_i, y_i) g_{\omega}(x_i, y_i + \eta_i) [T_{11}(y_i)]_{\omega} [T_{11}(y_i + \eta_i)]_{\omega} \end{aligned}$$

with $\xi_i = y_i + \eta_i$. Now, if T_{11} is only correlated with its space-separated $T_{11}(y_i + \eta_i)$ over a distance which is short compared with a typical distance over which the Green's function varies, the above may be approximated

by

$$c_e^4 I_a I_a^* \approx k^4 \int_V g_{\omega}(x_i, y_i) g_{\omega}(x_i, y_i)^* dV(g_i) \cdot \int_V dV(\eta_i) [T_{11}(y_i)]_{\omega} [T_{11}(y_i + \eta_i)]_{\omega}$$

The second integral here has the magnitude of the squared value of $T_{11}(y_i)_{\omega}$ times a volume over which the T_{11} is correlated, which itself may be a function of the frequency. The first integration merely weights the second by the square of the Green's function and adds up all the correlated volumes. Consequently, the order of magnitude estimate is

$$c_e^4 I_a I_a^* \approx k^4 (g_{\omega} g_{\omega}^*)_{\text{average}} V V_{\text{cor}} \left[(T_{11})_{\omega} (T_{11})_{\omega}^* \right]_{\text{average}} \quad (6)$$

Similarly, any term involving an area integration, say term I_c , is

$$c_e^4 I_c I_c^* \approx c_e^2 (g_{\omega} g_{\omega}^*)_{\text{exit plane}} S_e S_{\text{cor}} \left[\frac{\partial}{\partial y_i} (T_{11})_{\omega} \right] \left[\frac{\partial}{\partial y_i} (T_{11})_{\omega} \right]_{\text{exit plane}}^*$$

To obtain the mean square value of pressure, the Fourier transform product is multiplied by the 2π times the reciprocal of the ensemble average time and integrated over frequency.⁽⁶⁾ That is,

$$\langle p'^2 \rangle = \int_{-\infty}^{\infty} \frac{2\pi p_{\omega} p_{\omega}^*}{t_0} d\omega$$

For order of magnitude estimation purposes the Green's function will

be taken in the low frequency analytical form of Eq. (5). The motor parameters will be taken as those of the baseline case of the Appendix, with $\tilde{\mu} = 0.5$. The crux of the problem is estimation of the spectral character of the source terms T_{ij} , σ and \mathcal{M} .

A. Turbulence Noise

There have been no direct measurements of the turbulence intensity or spectra distributions within a solid rocket motor. A simulation,⁽⁸⁾ however, has shown intensity distributions which are similar to those of pipe flow.⁽⁷⁾ Consequently, the spectral distributions of Ref. (7) will be used for estimation purposes. First, look at term I_a and the makeup of $(T_{11})_\omega$,

$$(T_{11})_\omega = \rho_e \left[(u_e + u')(u_e + u') \right]_\omega'$$

where, in accordance with Lighthill theory, the primary contribution to the fluctuations in T_{ij} are those due to the velocity fluctuations (the density fluctuations are accounted for in the combustion noise term and it may be shown that the density fluctuations arising in T_{ij} are much smaller than those in term II_b). The Fourier transform of the fluctuating part of T_{11} then becomes

$$(T_{11})_\omega = \rho_e \left[2 u_e u_\omega + (u'^2 - \langle u'^2 \rangle)_\omega \right]$$

This consists of a linear part plus a part due to nonlinear fluctuations in velocity. The first term is the analogue of "shear-noise" and the second is "self-noise", using the terms of jet noise theory.⁽¹⁵⁾

The quantity needed is

$$\begin{aligned} (T_{11})_{\omega} (T_{11})_{\omega}^* = \rho_e^2 \left\{ 4u_e^2 u_{\omega} u_{\omega}^* + 2u_e \left[(u - \langle u'^2 \rangle)_{\omega}^* u_{\omega} \right. \right. \\ \left. \left. + u_{\omega}^* (u^2 - \langle u'^2 \rangle)_{\omega} \right] \right. \\ \left. + (u^2 - \langle u'^2 \rangle)_{\omega} (u^2 - \langle u'^2 \rangle)_{\omega}^* \right\} \end{aligned}$$

In jet noise theory it has been estimated that the self noise terms are of the same magnitude as the first term above.⁽¹⁵⁾ The reasons lie in the facts that in jets a) the turbulence level is higher than in pipe flow and b) there are many more of the nonlinear self noise terms in jet theory than in the above so that the sheer weight of numbers comes in. Here, however, there are only two terms involving the non-linear part and mean turbulence levels are only of the order of 5%. Consequently, the first term will dominate.

$$(T_{11})_{\omega} (T_{11})_{\omega}^* \approx 4 \rho_e u_e^2 u_{\omega} u_{\omega}^*$$

For estimation purposes, Laufers' pipe flow spectra for a particular radial location are shown in Fig. IV A-1. Shown are both the radial and axial velocity fluctuation spectra, with the axial velocity the one of interest here. It is known that, for fully developed flow, the spectra are invariant with pipe diameter and flow velocity if they are plotted as $F(St)$ vs $St = 2\tilde{k}a$. The scale is shown in Fig. IV A-1 such that

$$\langle u'^2 \rangle / \bar{u}^2 = \int_0^{\infty} F(St) dSt$$

The next problem in evaluation of Eq. (6) lies in determination of V_{cor} . If Taylor's hypothesis is followed, that the turbulence is convected

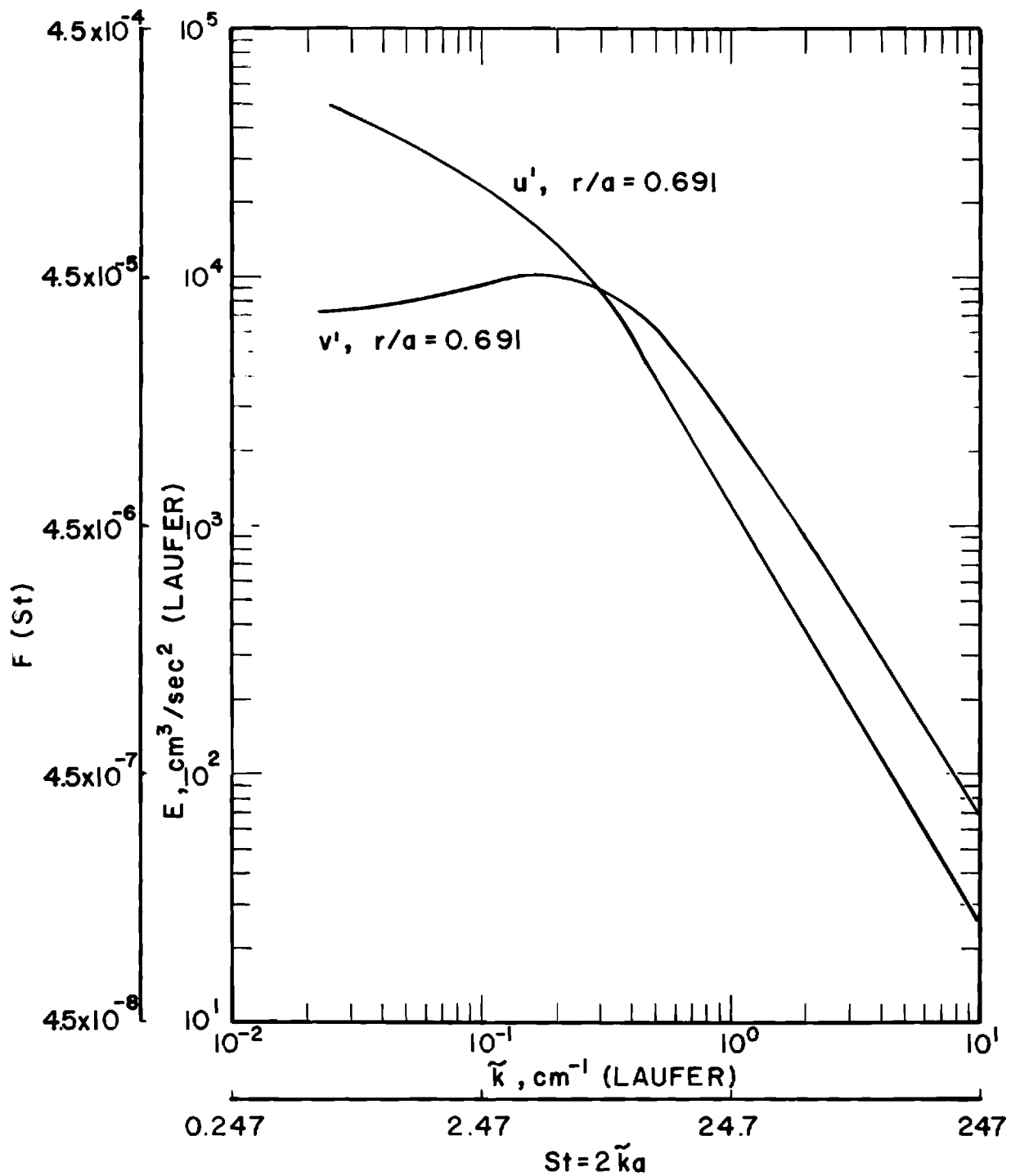


Figure IV A-1. Turbulence Spectra from Laufer's Pipe Flow Data.

by the mean flow speed, the frequencies seen by an observer would correspond to a flow velocity divided by an eddy size. The correlation volume would be therefore proportional to ω^{-3} . However, Taylor's hypothesis must fail at sufficiently low frequency because the eddies would have to be of infinite size. At the low frequency end of the range it appears reasonable to choose the integral scale of the turbulence as the appropriate length scale. A function which has the above behavior is

$$V_{\text{cor}} = \frac{l_e^3}{(1 + \frac{l_e}{2a} St)^3}$$

and has the transition to a behavior like ω^{-3} when the frequency is reached corresponding to convection of the integral scale eddies by the mean flow speed. From Laufer's pipe flow data $l_e/2a \approx 0.4$

Finally, since there is little or no turbulence at the head end and highly developed turbulence at the exhaust end, the full volume V does not contribute to the noise in Eq. (6). Arbitrarily, V is divided by two in the magnitude estimate. Then the operation of Eq. (2) is performed. The result is

$$\frac{\langle p'^2 \rangle}{P_e} I_a = 10^{-6}$$

This result shows the volume distributed turbulence to be an infinitesimal noise source.

The term I_b is treated in substantially the same manner as above. The nozzle admittance condition is $a_w = -M_e(\gamma-1)/2\gamma$, appropriate for a short nozzle. Here only a surface area integration is required and

$(T_{11})_{\omega}$ is estimated as above and $S_{\text{cor}} = \ell_e^2 / (1 + \frac{\ell_e}{2a} \text{St})^2$. The result is that

$$\frac{\langle p'^2 \rangle}{\rho c} I_b = 2 \times 10^{-5}$$

which is also a small percentage fluctuation in pressure.

Term I_c presents a more difficult magnitude estimation problem.

A quantity required is

$$\begin{aligned} \frac{\partial}{\partial y_i} (T_{i1})_{\omega} &= \frac{\partial}{\partial y_i} (\bar{u}_1^2 + \bar{u}_1 u'_i + \bar{u}_1 u' + u'_1 u'_i - \overline{u'_1 u'_i})_{\omega} \\ &= \bar{u} \frac{\partial u_i}{\partial y_i} \omega + \frac{\partial}{\partial y_i} [u'_1 u'_i - \overline{u'_1 u'_i}]_{\omega} + \bar{u} \frac{\partial u_{\omega}}{\partial y} \end{aligned}$$

It is assumed that the turbulence motion is primarily vortical so that first term, being a divergence of the vortical velocity fluctuation, is zero. The second term is actually a sum of three terms involving the nonlinear self noise part of T_{ij} . The third term is the linear part and consists of contributions from only the axial velocity fluctuations. When one then estimates

$$\frac{\partial}{\partial y_i} (T_{i1})_{\omega} \quad \frac{\partial}{\partial y_i} (T_{i1})_{\omega}^*$$

there arise sixteen non-zero terms of which one consists of the linear part squared, six come from the product of the linear and nonlinear parts, and nine come from the products of the nonlinear parts. At a five percent turbulence fluctuation level one would need about twenty of the linear-nonlinear product terms to be comparable in magnitude to the square of the linear parts. One would need about 400 of the nonlinear-squared terms to be comparable to the square of the linear parts. Consequently, only the

square of the linear parts is retained and

$$\frac{\partial}{\partial y_i} (T_{i1})_{\omega} \frac{\partial}{\partial y_i} (T_{i1})_{\omega}^* \approx \rho_e^2 u_e^2 \frac{\partial u_{\omega}}{\partial y} \frac{\partial u_{\omega}^*}{\partial y}$$

Now, if the turbulence is convected at the flow speed $\partial u_{\omega} / \partial y \approx i \omega u_{\omega} / u_e$, and this will be assumed here. The magnitude analysis then follows the previous approach to yield

$$\frac{\langle p'^2 \rangle}{\rho_e} I_c = 7 \times 10^{-5}$$

This is now large enough to be a contender for noise-making at the 1% level. It has been independently verified, by using the linearized vorticity-acoustic approach⁽⁵⁾ to this problem, that term I_c is the major term arising in a vorticity-nozzle interaction. Thus, two different approaches yield the same answer, giving confidence in this Lighthill approach.

B. Combustion Noise

Consider now the term II_a whereby

$$c_e^4 II_a II_a^* = k^2 \rho_e^2 c_e^4 M_r^2 \left(\int_{S_w} m_w^* g_w^* dS \right)$$

This is estimated as usual as

$$\gamma^2 p^2 M_r^2 g_w g_w^* S_w \tilde{G}_\delta$$

where

$$\tilde{G}_\delta = \frac{1}{S_w} \int dS \int dS m_w m_w^*$$

is a quantity related to the quantity measured in Section III. In fact,

$\tilde{G}_\delta = S_p G_\delta$ where G_δ was the source quantity measured. A reasonable fit to the UTP-3001 and MC-170 data, representing the maximum noise propellant, is

$$G_\delta = \frac{3.98 \times 10^{-7}}{1 + \left(\frac{\omega}{42}\right)^2} \text{ sec/rad}$$

at 300 psia. Again using the low frequency form of the Green's function and integrating over all values of frequency as

$$\frac{\langle p'^2 \rangle}{\bar{p}^2} II_a = 8 \times 10^{-7}$$

Thus, combustion noise near the propellant surface is a small noise source. Recall, however, that crossflow appears to increase this level. It is possible that this could become significant in the presence of crossflow. However, considered here were the maximum noise propellants, and, as a consequence, combustion noise generated near the propellant will be rejected as an important noise source in general. It is possible that this should be reexamined in the future. The scaling rules of this noise should also be noted in Ref. (10): It is possible that under some conditions

of pressure and burn rate this noise may become important.

Now consider the noise generated in the chamber volume by the burning suspended metal. The source term in Π_b is $\bar{D} \sigma' / Dt$ which is the time derivation of the entropy fluctuations seen by an observer moving with the mean fluid speed. By the second law of thermodynamics this is composed of two parts - the heat release rate fluctuation and convection of mean entropy gradients by the observer by the turbulence velocity fluctuations. It has been assumed in the treatment that mean entropy gradients are absent so one is left with the heat release rate fluctuations. One will see a heat release rate fluctuation moving at the mean fluid speed by the convection of individual metal combustion fields past the observer by the turbulence of the field and by any metal droplet motion not strictly parallel to and with the same velocity as the mean velocity. It is presumed that each metal droplet burns with its own vapor phase diffusion flame wrapped about the droplet. (14) Consequently, the volume associated with the combustion/diffusion field surrounding the droplet is of the order of the droplet volume.

It is instructive here to compare magnitudes. The number of droplets per unit volume is given approximately by

$$n_d = \frac{\rho_e Y_d^6}{\pi d_d^3 \rho_S} = \frac{1}{v_d} \equiv \left(\frac{\pi d_{inf}}{6} \right)^{-3}$$

so that d_{inf} is a typical linear dimension between particles. Using numbers for aluminum metal at 300 psi and assuming an aluminum loading of 16%

$$d_{inf}/d_d \approx 28$$

Therefore, droplets are well separated and can burn individually. The ratio

of d_{inf} to a typical eddy size is given by

$$\frac{d_{inf}}{l_e} = 28 \frac{d_d}{l_e} \approx \frac{28}{0.8} \frac{d_d}{a} \approx 0.01$$

for $d_d = 100 \mu\text{m}$ and $a = 1 \text{ ft}$. Therefore, there are about 10^6 droplets per eddy. The major point here is that the volumes over which combustion events are correlated are extremely small compared with the correlation volumes of the macroscopic turbulence.

In the magnitude estimate $(\bar{D}\sigma/Dt)_\omega$ will be estimated as $\omega \sigma_\omega$. Then

$$c_e^4 \Pi_b \Pi_b^* \approx \gamma^2 \bar{p}^{-2} k^4 g_\omega g_\omega^* \left(\int \sigma_\omega dV \right) \left(\int \sigma_\omega^* dV \right)$$

A slightly different problem exists here in estimation of the volume integrals since such a large distance exists between correlated volumes, as shown in the magnitude estimates above. The meaning of the double volume integration is the $\sigma_\omega \sigma_\omega^*$ magnitude times the correlation volume times the total volume over which correlated volumes exist. Here

$$\int \sigma_\omega dV \int \sigma_\omega^* dV \approx \sigma_\omega \sigma_\omega^* d_d^3 V \left(\frac{d_d}{d_{inf}} \right)^3$$

where the last factor accounts for the fact that the correlated volumes are widely disbursed. Then using the low frequency form of the Green's function and the usual substitutions

$$\frac{p_\omega p_\omega^*}{\bar{p}^2} \approx \frac{\gamma^2 d_d^3 1 (2\pi)^2}{S_e u_e^2} \omega^2 \frac{(d_d/d_{inf})^3}{(1.9 - \gamma n)^2} \sigma_\omega \sigma_\omega^*$$

Now, unless a spectral shape is introduced for $\sigma_\omega \sigma_\omega^*$ an integration is impossible to perform to obtain $\langle p'^2 \rangle$. As a first approximation, assume that all of the noise is concentrated in a narrow frequency band near ω_0 and

assume that ω_0 corresponds to roughly 400 Hz, where the temperature fluctuations peak for a run in Section III. Then even if $\langle \sigma'^2 \rangle$ is as large as unity, the result is

$$\left\langle \frac{p'^2}{\bar{p}^2} \right\rangle_{II_b} = 2 \times 10^{-7} d_d^3$$

with the units of d_d in feet. It is clearly seen that for any realistic droplet size $\left\langle \frac{p'^2}{\bar{p}^2} \right\rangle_{II_b}$ is negligible. This is a direct consequence of the fact that the correlation volumes are so small; there is an extreme amount of cancellation of sound. None of the assumptions in the magnitude analysis, if relaxed, would change this conclusion.

C. Entropy Noise

Now consider term III with $b_e = M_e/2$, consistent with the short nozzle assumption. Here

$$III \quad III^* \quad c_e^4 \approx \gamma^2 k^2 \bar{p}^2 g_\omega g_\omega^* \frac{M_e^2}{4} \int \sigma_\omega dS \int \sigma_\omega^* dS$$

Again, there is a problem here in the double area integral because the correlation areas are disbursed because the droplets are widely separated. It is here being assumed that the temperature fluctuations behave in accordance with the experimental results of Section III and that in an actual rocket motor, even if combustion is complete by the time the exit plane is reached, the correlation sizes correspond roughly to the initial metal droplet sizes.

Then

$$\int \sigma_\omega dS \int \sigma_\omega^* dS \approx d_d^2 \sigma_\omega \sigma_\omega^* \left(\frac{d_d}{d_{inf}} \right)^2$$

Using the low frequency form of the Green's function an integration may be directly performed and even if $\langle \sigma'^2 \rangle$ is as large as unity

$$\left\langle \frac{p'^2}{\bar{p}^2} \right\rangle_{III} \approx 10^{-7} d_d^2$$

with d_d again in feet. Clearly entropy noise is not a factor for any realistic d_d .

The conclusion is evident that only one noise source is clearly dominant - that due to vorticity-nozzle interaction. It should be remarked that the distributed turbulence is close in magnitude, but upon close examination $\langle p'^2 \rangle_{I_a \text{ or } I_b} \propto M_e^4$. Since a high M_e case was purposefully chosen for this case, a higher number than normal has appeared for the distributed turbulence estimate. In addition there is some concern about the estimate for combustion noise near the propellant surface - if crossflow alters the results significantly. Consequently, comparison of the results with a motor firing are desirable.

V. Motor Prediction

The calculation of predicted pressure fluctuations in the solid rocket motor interior will now proceed more accurately on the basis of only one noise source - that of vorticity-nozzle interaction. To obtain a more accurate calculation than that produced in the order of magnitude calculations several things will be done. These are a) a more accurate spectral distribution and intensity of turbulence will be produced, b) the Green's function will be accurately calculated and c) the effects of propellant feedback response will be included.

The primary interest is at the head end of the motor. The "exact" formula for the spectral density of the pressure there, assuming only vorticity-nozzle interaction noise is present, is

$$G_p = \frac{2}{t_o} \rho_e^2 \omega^2 \left(\int_{S_e} u_\omega g_\omega dS \right) \left(\int_{S_e} u_\omega^* g_\omega^* dS \right) \quad (7)$$

In order to evaluate this exactly, the temporal and spatial behavior of the u_1 component of turbulence is required. In Laufer's pipe flow data the spectra of u_1 are given as a function of space location, but the spatial cross correlations are not. In the study of Ref. (8) only intensity distributions are given, with no consideration of spectra or spatial cross correlations. It is consequently necessary to introduce into Eq. (7) one of the approximations used in Section IV - the one dealing with an estimate of correlation area behavior with frequency and the assumption that the Green's function is invariant over a correlation volume. Equation (7) becomes

$$G_p = \frac{2}{t_o} \rho_e^2 \omega^2 g_\omega g_\omega^* S_{cor} S u_\omega u_\omega^* \quad (8)$$

where the correlation volume will be estimated as before with $S_{cor} = l_e^2 / (1 + l_e St/2a)^2$.

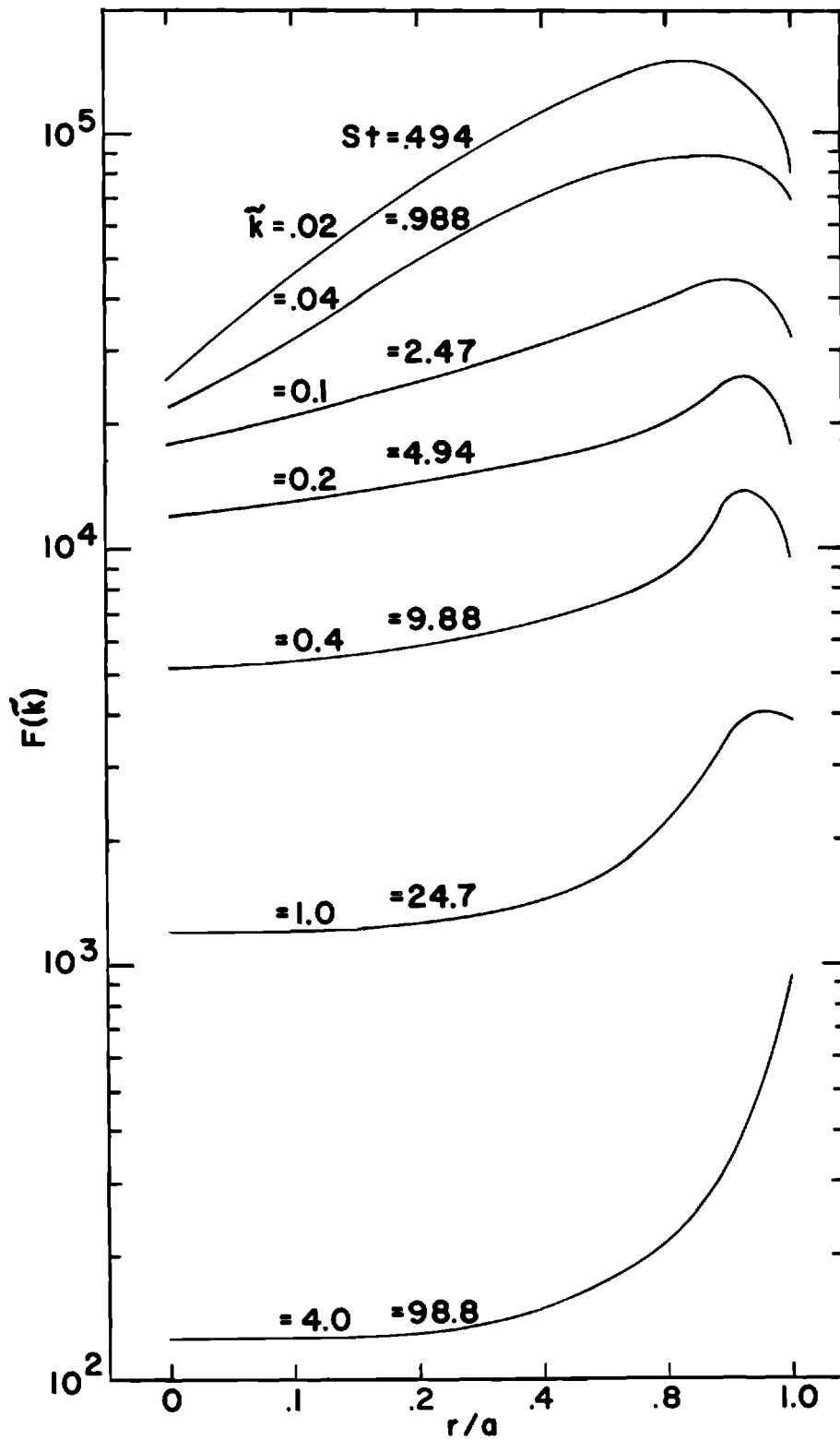


Figure V-1. Turbulence Spectra as a Function of Radial Position with Wavenumber a Parameter.

The spectral behavior of u_1 will be taken from Laufer's pipe flow data but corrected in level to yield the intensity distribution of Ref. (8). First, Fig. V-1 displays the pipe flow spectra data as a function of radial position with wavenumber as a parameter. The cross-section is broken up into five equal area sections with midpoint r/a values equal to 0.22, 0.54, 0.71, 0.84 and 0.95. Values of the spectra from Fig. V-1 at these points and for the values of St on Fig. V-1 are stored for computation. The units of F are immaterial since only shape is required here. Secondly, the spectral absolute level at each radial location is scaled such that the area under the curve will give the proper turbulence intensity. This is done by observing that the experiments of Ref. (8) yield a maximum intensity near the wall

$$(\langle u_1'^2 \rangle)_{\max}^{1/2} = 0.248 \bar{u}^{0.8} \text{ m/s} \quad (9)$$

with \bar{u} in m/s. It is also found that a reasonable correlation of the minimum intensity, at $r = 0$, is given by

$$(\langle u_1'^2 \rangle)_{\min}^{1/2} = 0.37 \left[(\langle u_1'^2 \rangle)_{\max}^{1/2} \right]^{0.47} \quad (10)$$

again with all units in m/s. It is next observed that the maximum intensity occurs so close to the wall that for the calculations here a monotonic variation from the minimum to the maximum will be assumed. The variation which fits the data of Ref. (7) is a law which varies the intensity according to $(r/a)^{1.7}$. Thus the formula for radial variation of intensity is

$$(\langle u_1'^2 \rangle)^{1/2} = (\langle u_1'^2 \rangle)_{\min}^{1/2} + \left\{ (\langle u_1'^2 \rangle)_{\max}^{1/2} - (\langle u_1'^2 \rangle)_{\min}^{1/2} \right\} (r/a)^{1.7} \quad (11)$$

Thus at each radial location G_u has the shape given by Fig. V-1 and is scaled so that the area under the spectral plot yields Eq. (11).

The next problem is the incorporation of a feedback response law into the Green's function in Eq. (8). A perusal of the combustion instability

literature⁽¹⁶⁾⁽¹⁷⁾ for the pressure coupled response functions (velocity coupling is specifically excluded by assumption) yields some interesting observations. First, there is a paucity of data in the low frequency regime of interest here (say, <1000 Hz). Secondly, there is little data to support differences in response functions between metalized and non-metalized propellants. Thirdly, there is no adequate theory that fits the data on even unmetalized propellants. Fourth, a reasonably significant collapse of some data occurs if one plots the value of $\tilde{\mu}$ vs. f/r^2 rather than f alone. This last fact suggests that the thermal wave in the solid phase controls at least the low frequency behavior of $\tilde{\mu}$, since theories based on such a mechanism yield an f/r^2 scaling rule.⁽¹⁶⁾ It is also found a posteriori that the feedback law chosen does not influence the results greatly, as long as one is sufficiently removed from a stability limit. Consequently, the "A-B" model of Ref. (16) is chosen. This sets

$$\frac{\tilde{\mu}}{n} = \frac{AB}{\lambda + A/\lambda - (1 + A) + AB}$$

$$\lambda = \frac{1}{2} + \left[\frac{1}{4} + i \frac{\alpha_p \omega}{r^2} \right]^{1/2} \quad (12)$$

with A and B free parameters. Best fits to much data yield B of order unity and A of the order of 20. For the computations to follow the values B = 1, A = 15 have been used which are appropriate for A-35 propellant.⁽¹⁶⁾ It is important to notice that Eqs. (12) yield the physically expected result that $\tilde{\mu} \rightarrow n$ as $\omega \rightarrow 0$. The calculation of the Green's function follows from the formulas in the Appendix.

Before proceeding with the actual calculations it is first important to notice a general result from Eq. (8). Since $1_e/a$ is expected to be relatively invariant with motor design variables, the maximum relative intensity of turbulence is relatively insensitive to \bar{u} in Eq. (9), and noticing the approximate

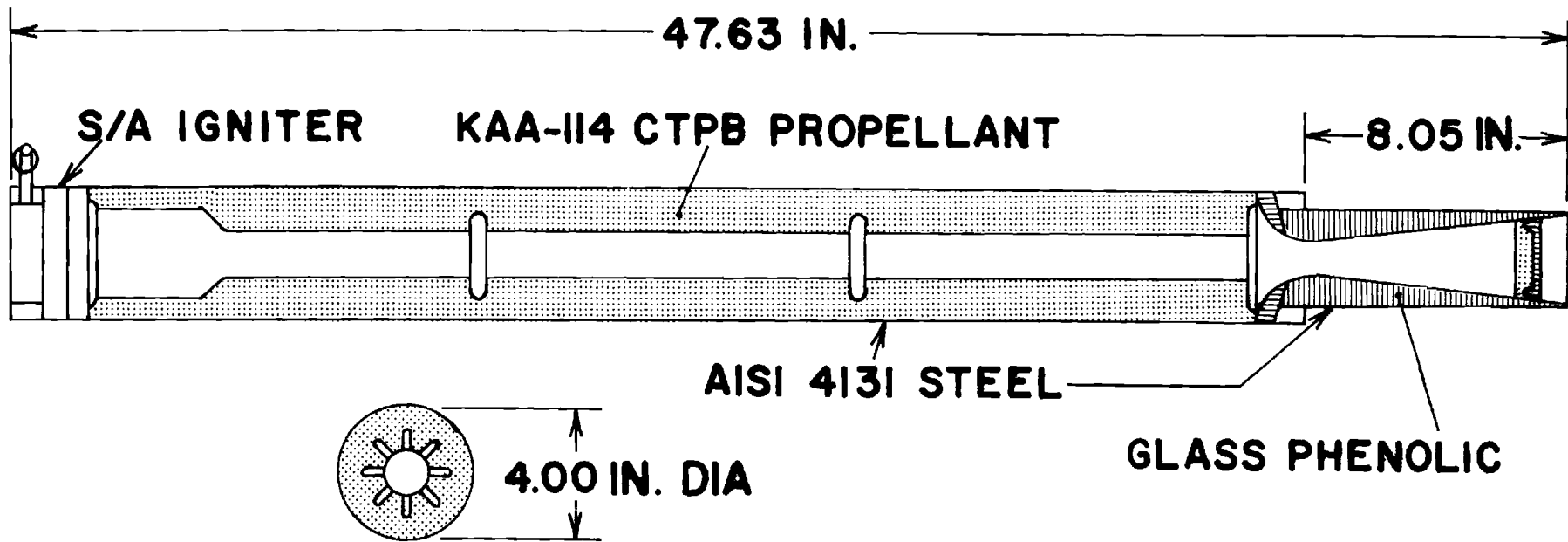
low frequency form of the Green's function in Eq. (5), it follows that an integration over frequency of Eq. (8) to yield $\langle p'^2 \rangle$ will yield $\langle p'^2 \rangle / \bar{p}^2$ completely insensitive to motor design variables. Therefore, the calculations made here for a particular motor will be more or less general for the relative pressure fluctuations. The spectral distribution will depend upon motor variables but $\langle p'^2 \rangle / \bar{p}^2$ will not.

It should be noted that the numbers to be calculated will, of course, depend upon the input intensity of turbulence. Considered here are motors with a relatively constant cross section area with axial position. If a complex grain design yields turbulence levels at variance with the inputs then different pressure fluctuation levels will be achieved. Using the physical notion that complex geometries will increase the turbulence level, it appears plausible that what is being calculated is a lower limit to the pressure fluctuations.

Motor data were supplied by Hercules Incorporated/Allegany Ballistics Laboratory. A cutaway view of the motor is shown in Fig. V-2. The motor conforms nicely to the assumptions of the theory in that the great majority of the grain length is a center perforated grain. The motor and firing designation was LCIM-7. The propellant formulation and characteristics are as follows

CTPB	13.0%
Fe ₂ O ₃	1.0%
Al (6 μm)	6.0%
AP (400 μm 31%, 200 μm 19%, 50 μm 30%)	80.0%
c*	5109 ft/sec
r @ 1000 psi 70°F	0.594 in/sec
n	0.406

The data of interest were over the first 0.8 sec of firing wherein the motor pressure is roughly constant at 1900 psia. Other numbers required for computation are as follows:



79

Figure V-2. Cutaway View of Solid Propellant Motor.

$$\begin{aligned}
 c_e &= 3630 \text{ ft/sec} & M_e &= 0.1447 \\
 l &= 2.96 \text{ ft} & a &= 0.097 \text{ ft} \\
 M_r &= 0.00244
 \end{aligned}$$

The thermal diffusivity of the propellant was taken as the value for pure AP, $\alpha_p = 6 \times 10^{-5} \text{ in}^2/\text{sec}$. Computed values for the maximum and minimum relative turbulence intensity were 9% and 0.8%, respectively. The short nozzle approximation was used, which is perfectly valid for the frequency range covered. As mentioned, the feedback parameters were taken as $B = 1.0$ and $A = 15$. This is a low metal loading motor, and in view of the results in the appendix that the metal damping affects the results very little, $Y_1 = Y_2 = 0$ are chosen.

The results are shown in Fig.V-3 for the theoretical spectrum. The results are presented as spectral level/50 Hz bandwidth to be consistent with the later experimental results. The spectrum has been normalized by the square of the mean pressure so that the area under the curve yields the square of the fractional pressure fluctuation. The number for the rms pressure fluctuation is $p'_{\text{rms}}/\bar{p} = 0.0036$, about the same level as estimated in Section IV. Most of the pressure fluctuation comes from the spectral distribution at very low frequency. The first longitudinal mode hump contains only a small amount of the mean square pressure.

The experimental spectrum was supplied on the basis of 200 points spaced 2.5 Hz apart, from 0-500 Hz. The pressure pickup was a water cooled Kistler gauge mounted in the head end. There was no detectable signal above 350 Hz. The setup of the electronics was actually to monitor a ± 100 psi oscillation so that all signal here is very close to the noise level of the equipment.

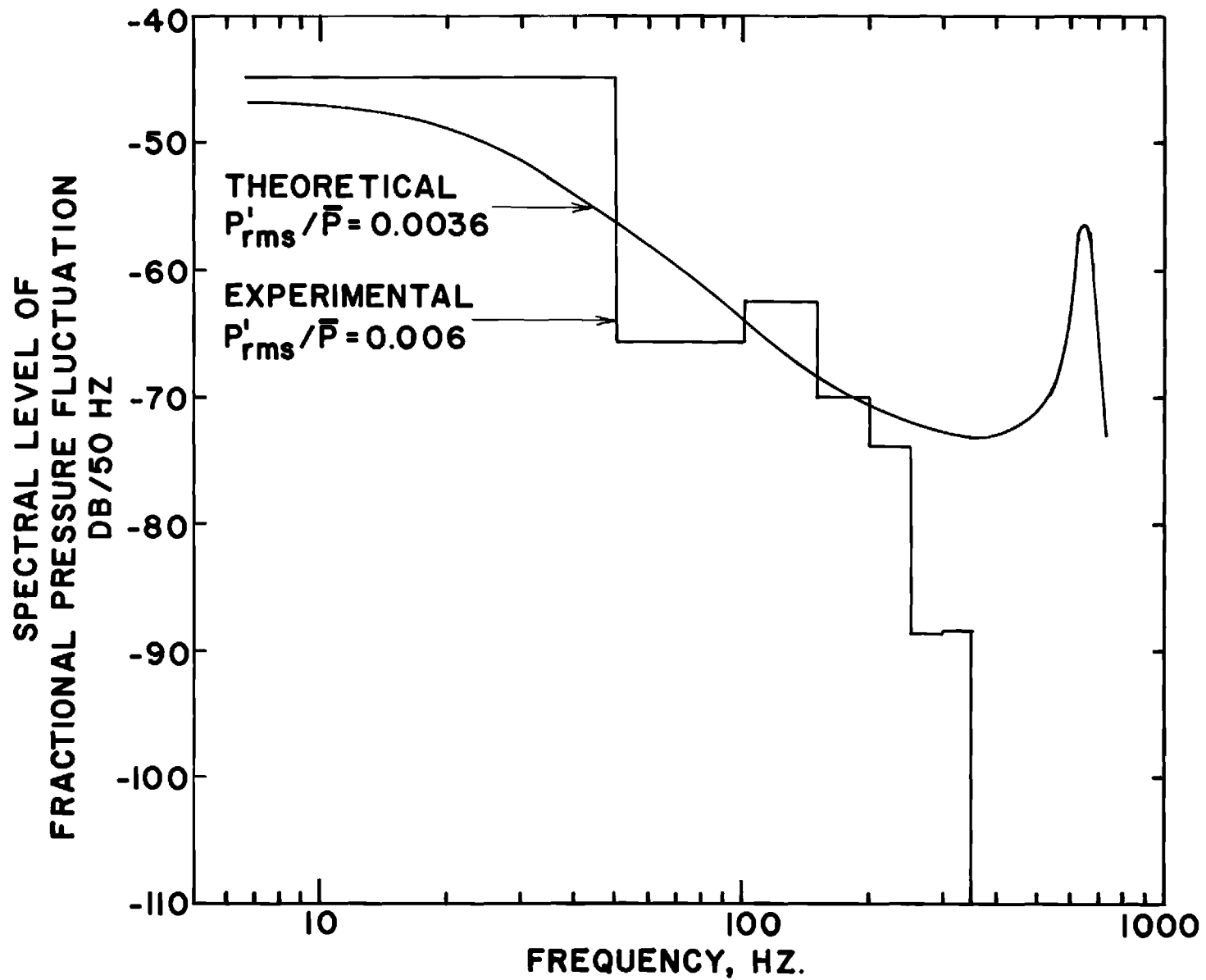


Figure V-3. Comparison of Theoretical and Experimental Spectra for Hercules Motor.

However, the comparison with theory is highly favorable so that it is believed the experimental spectrum is truly indicative of the gasdynamic noise. To smooth the spectrum, twenty adjacent bands are averaged so that in Fig. V-3 an experimental spectrum with a 50 Hz bandwidth is presented. Given all of the massaging of the data and the observations above, the error in the experimental spectrum is probably of the order of a factor of two, or ± 3 dB. Given all of the approximations of the theory the same kind of error may be expected in the theoretical curve. In this light, the agreement between theory and experiment on Fig. V-3 is considered remarkable.

It is noted that the rms pressure levels agree within a factor of 1.67. The spectral shape at low frequency is well predicted. The major discrepancy is beyond 300 Hz where the experiment does not show the cut-in of the first longitudinal mode. The significance of this discrepancy is believed to be that the turbulence spectrum of pipe flow does not strictly apply to the rocket motor system. In fact, with mass addition from the propellant surface one would expect a thickening of the mixing layer between the core flow and the injected flow as compared with the transition layer between core flow and zero wall flow in the case of pipe flow. This increase in mixing length scale should be reflected in greater low frequency content, as compared with pipe flow results. An interesting point here is that it may be possible to infer the turbulence spectrum from the pressure fluctuation results.

The fact that the theory somewhat underpredicts the level of the overall fluctuation should probably not be given too much attention. It would be tempting to blame it upon the neglect of the other noise sources. However, as mentioned above, the theory and the experiment contain inaccuracies which are probably larger than the observed difference in pressure. It should be recalled, however that this is considered a lower limit analysis.

VI. Conclusions

1. There is a single noise source which is dominant in producing pressure fluctuations within a solid rocket motor cavity. This noise is caused by turbulence encountering the exhaust nozzle and is dominant whether or not the propellant is metalized or is composite. The only caveats are that a) there is a possibility that at low port-to-throat the turbulence distributed through the chamber volume may become important as a noise source and b) there is still an unknown effect of turbulence interaction with the flame zone near the propellant surface, which may be an additional noise source.
2. The noise floor due to the above mechanism is at a level of roughly 0.4% fluctuation of chamber pressure, is low frequency in nature and can be larger than the stated level if the motor grain design induces a high turbulence level in the chamber gases.
3. The noise level is predictable but the spectral distribution needs some further experimental work, because the theory predicts a slower high frequency roll-off than is indicated experimentally.
4. For simple motor geometry the noise considered is relatively invariant with motor design variables, when quoted as the magnitude of the fractional pressure fluctuation.
5. A simple theory of aeroacoustics, based upon the Lighthill approach, has recovered all of the expected physics of the noise problem. It allows a framework to calculate noise magnitudes excluded here if

future experimental work shows the neglected sources should be included.

6. As opposed to results of instability analysis, the effects of metal and metal oxide damping and of the propellant feedback response functions are weak in noise analysis, as long as one is reasonably well removed from a stability limit.
7. If the source frequencies are primarily below that of the first transverse acoustic mode of the chamber gases, the pressure oscillations and, hence, the motor vibration is purely axial, except for manufacturing misalignments and small local, rather than global, pressure fluctuations.

Appendix - General Theory

Formulation-Differential Equation

There are several possible theoretical formulations for the problem of the interior aeroacoustics of a rocket motor.⁽⁵⁾ They are all approximate methods and the method chosen should represent a balance between analytical simplicity and the accuracy of the data to be used in the theory. After a review of several possible approaches it was decided to attack the problem from the Lighthill theory. This was done because a) an analytical solution to the problem was anticipated by this method b) the theory is known to give proper orders of magnitude and scaling rules in calculations of jet noise⁽⁵⁾ and combustion noise,⁽¹⁾ c) the theory is especially good for relatively low Mach number flows such as found in the interior of rocket motors d) the data base to be used in the theory will contain inaccuracies that make use of a more accurate theory unjustified and e) it was found possible to include all of the anticipated physical effects of the problem through this approach.

Writing the continuity and momentum equations for the gas phase

$$\frac{\partial \rho}{\partial t} + \frac{\partial}{\partial x_i} (\rho v_i) = m \quad (1)$$

$$\rho \frac{\partial v_i}{\partial t} + \rho v_j \frac{\partial}{\partial x_i} v_i = - \frac{\partial p}{\partial x_i} + f_i \quad (2)$$

In Eq. (1) the mass source for the gas phase comes from the combustion of suspended condensed phase material. In Eq. (2) the force term comes from drag of the condensed phase material. Equation (2) considers an inviscid gas, except for the drag term, since viscosity plays little role in noise generation;⁽⁴⁾ the larger turbulent eddies are responsible for noise, whereas viscosity is primarily active in the fine scale structure of the turbulence.

The Lighthill equation is obtained by a combination of Eqs. (1) and (2). This is

$$\begin{aligned} \frac{\partial^2 \rho}{\partial t^2} - c_e^2 \frac{\partial^2 \rho}{\partial x_i \partial x_i} &= \frac{\partial^2}{\partial x_i \partial x_i} (\rho v_i v_j) + \frac{\partial^2 (p - c_e^2 \rho)}{\partial x_i \partial x_i} \\ &\quad - \frac{\partial}{\partial x_i} (f_i + m v_i) + \frac{\partial m}{\partial t} \end{aligned} \quad (3)$$

Equation (3) holds for any constant c_e , but c_e will be now identified with the speed of sound at the nozzle entrance plane. The last two terms involving mass addition are typically dominated by heat addition, which will arise from the third term on the right hand side of Eq. (3); consequently, the last two terms of Eq. (3) are dropped. Since it will be found that it is most convenient to work in the frequency domain, rather than the time domain, the Fourier transform is taken of Eq. (3).

The result is

$$\frac{\partial^2 \rho_\omega}{\partial x_i \partial x_i} + k^2 \rho_\omega = \frac{-1}{\partial x_i \partial x_j} (T_{ij} \omega + \frac{\partial^2}{\partial x_i \partial x_i} (\rho_\omega - \frac{p_\omega}{c_e^2})) + \frac{\partial}{\partial x_i} (f_{i\omega}) \quad (4)$$

In Eq. (4) all quantities are now the transform of the fluctuating quantities; the d.c. components have been removed by subtraction.

Now, two kinds of condensed phase particles will be considered in the calculation of f_i , a metal and its oxide. It is furthermore assumed that a single representative size may be assigned to each particle type. Since the metal will disappear as the nozzle is approached, due to combustion, the size assigned to the metal will be some average size during the metal's lifetime. An average number density will also be assigned to the metal and oxide, recognizing that in reality this will be a function of chamber position.

If the number density were a constant, the particles were suspended in a stream flowing at constant velocity u_e , and the particles were also flowing at velocity u_e , there would be no drag. Considering fluctuations about such a condition

$$f'_i = \bar{n} D'_i \quad (5)$$

The condensed phase momentum equation is

$$m \left(\frac{\partial v_{p_i}}{\partial t} + v_{p_j} \frac{\partial}{\partial x_j} v_{p_i} \right) = - D_i$$

which becomes for fixed mass m and the approximation of Eq. (5)

$$\frac{\partial v'_{p_i}}{\partial t} + \bar{u}_e \frac{\partial}{\partial x} v'_{p_i} = - D'_i \quad (6)$$

Using Stokes law for the drag coefficient

$$C_D = \frac{24}{Re}$$

and taking the Fourier transform of Eq. (6),

$$\begin{aligned} \frac{\partial v_{p_i \omega}}{\partial x} + \frac{i\omega}{u_e} v_{p_i \omega} &= \frac{3\pi d \mu}{m u_e} (v_{i \omega} - v_{p_i \omega}) \\ &\equiv \alpha (v_{i \omega} - v_{p_i \omega}) \end{aligned} \quad (7)$$

The exact solution to Eq. (7), subject to the condition that there is no particle motion fluctuation at the head end ($x=0$) is

$$v_{p_i \omega} = \alpha e^{-\beta x} \int_0^x v_{i \omega} e^{\beta x} dx \quad (8)$$

with $\beta \equiv i\omega/u_e + \alpha$. For large β , an asymptotic solution to Eq. (8) is

$$v_{p_i \omega} = v_{i \omega} \alpha / \beta \quad (9)$$

Equation (9) is exact in two limits; these are $\beta \rightarrow \infty$ (either α or ω/u_e large) or $\alpha \rightarrow 0$. There is error committed for moderate β (both α and ω/u_e moderate). Because of the exact behavior at two limits this error involved in use of Eq. (9) is expected to be minimal, especially in

view of the other approximations leading to Eq. (7). Moreover, it will be found that there is a relatively small effect of condensed phase drag on the solution. Consequently, Eq. (9) is accepted and the Fourier transform of Eq. (5) becomes

$$f_{i\omega} = \bar{n} \alpha u_e \left(\frac{\alpha}{\beta} - 1 \right) v_{i\omega} \quad (10)$$

Neglecting the mass addition term in Eq. (1), consistent with a previous assumption, and assuming small fluctuations about the exit plane conditions together with a mean one-dimensional flow of the chamber gases, the transform of Eq. (1) becomes

$$i\omega \rho_\omega + \bar{u} \frac{\partial}{\partial x} \rho_\omega + \bar{p} \frac{\partial}{\partial x_i} v_{i\omega} = 0$$

whereby with the aid of Eq. (10)

$$\begin{aligned} \frac{\partial}{\partial x_i} f_{i\omega} &= \frac{Y_d}{1-Y_d} \left[i\omega \rho_\omega + \bar{u} \frac{\partial \rho_\omega}{\partial x} \right] \frac{\omega}{i} \left(\frac{i\alpha u_e}{\omega} \right) \left[\frac{1}{1 - \frac{\alpha u_e i}{\omega}} \right] \\ &\equiv z_d \left[\omega^2 \rho_\omega + \frac{\bar{u}\omega}{i} \frac{\partial \rho_\omega}{\partial x} \right] \end{aligned} \quad (11)$$

Finally, a factor of $(2iku_e/c_e) \partial \rho_\omega / \partial x$ is subtracted from both sides of Eq. (4) and Eq. (8) is substituted in Eq. (4) with the additional approximation in Eq. (8) that $\bar{u} = u_e$. The result is

$$\begin{aligned} \frac{\partial^2 \rho_\omega}{\partial x_i \partial x_i} - ikM_e \frac{\partial \rho_\omega}{\partial x} [2 + zd] + \kappa^2 \rho_\omega &= -\tilde{\Gamma} \\ \tilde{\Gamma} &\equiv \frac{1}{c_e^2} \frac{\partial^2}{\partial x_i \partial x_j} (T_{ij})_\omega + \frac{\partial^2}{\partial x_i \partial x_i} \left(\rho_\omega - \frac{p_\omega}{c_e^2} \right) - z ikM_e \frac{\partial \rho_\omega}{\partial x} \\ \kappa^2 &= k^2 (1 + z_d) \end{aligned} \quad (12)$$

Some of the approximations in the first of Eqs. (9) can now be rationalized. The operator on the left hand side is easily recognized as that appropriate to wave propagation in the presence of a uniform mean flow where a) the Mach number is low so that terms of the order of M_e^2 compared with unity have been neglected and b) a correction for droplet drag is present. The insertion of M_e for the actual variable $M(x)$ or $M(x_i)$ is an approximation which is valid in the spirit of this treatment, which is basically an order of magnitude treatment. The main effect of the second term on the left hand side is on the resonant frequencies of the motor (as may be seen later). While it is believed reasonable to include this effect, it is done in only an approximate manner. The z_d term in the second term on the left hand side is actually small compared with 2. As may be deduced by direct computation $z_d < Y_d$ which, at a maximum, is of the order of 0.2. Consequently, errors in the treatment of condensed phase drag affects this term very little. Droplet drag is essential in the last term on the left hand side, in the wave number κ . z_d is a complex number and the imaginary part will induce an imaginary part to κ . This will be responsible for a damping effect of condensed phase drag. There is, in fact, an optimum damping condition. This is seen by investigation of the imaginary part of z_d which is proportional to

$$\frac{\alpha u_e / \omega}{1 + \left(\frac{\alpha u_e}{\omega} \right)}$$

This has a maximum at $\alpha u_e / \omega = 1$. Thus, this approximate treatment retains the known feature of more exact treatments that at each frequency there is an optimum particle size for damping. ⁽¹⁸⁾ Summarizing, even though

there are approximations in the treatment of the particle damping and flow effects, the essential physics are retained and the scaling properties with various variables are retained.

Equation (9) is the modified Lighthill equation to be solved for this interior aeroacoustics problem. In the spirit of that approach, the right hand side is considered calculable from estimates of turbulence behavior. The right hand side contains the Lighthill quadrupoles, T_{ij} the combustion noise term, $\rho_w^{(1)}$, a pressure fluctuation term which will be addressed later and a term involving M_e . This last term will now be dropped as being small compared with the other source terms (right hand side terms), especially the $\partial^2 \rho_w / \partial x_i \partial x_i$ term. The right hand side of Eq. (12) will then act as the forcing function for the wave operator on the left hand side, where now the right hand side is set equal to $-\Gamma$ with

$$\Gamma = \frac{1}{c_e^2} \frac{\partial^2}{\partial x_i \partial x_j} (T_{ij})_w + \frac{\partial^2}{\partial x_i \partial x_i} \left(\rho_w - \frac{p_w}{c_e^2} \right)$$

To solve the equation appropriate boundary conditions are required.

Formulation - Boundary Conditions

The configuration is as shown in Fig. A-1. The differential equation in Eqs. (12) holds inside of V , which is enclosed by the bounding surface S . At this point it will be assumed that the cross-section area is constant with axial distance, and, in fact, that the grain is cylindrically perforated, although this will be relaxed later to allow more complex cross sectional shapes. The surface S_h at the head end coincides with the wall, and, since flow velocities are small there, it is assumed there is no turbulence there. The surface S_e bounds the nozzle entrance plane, across which, of course, a turbulent fluid is flowing. The surface S_w is set far

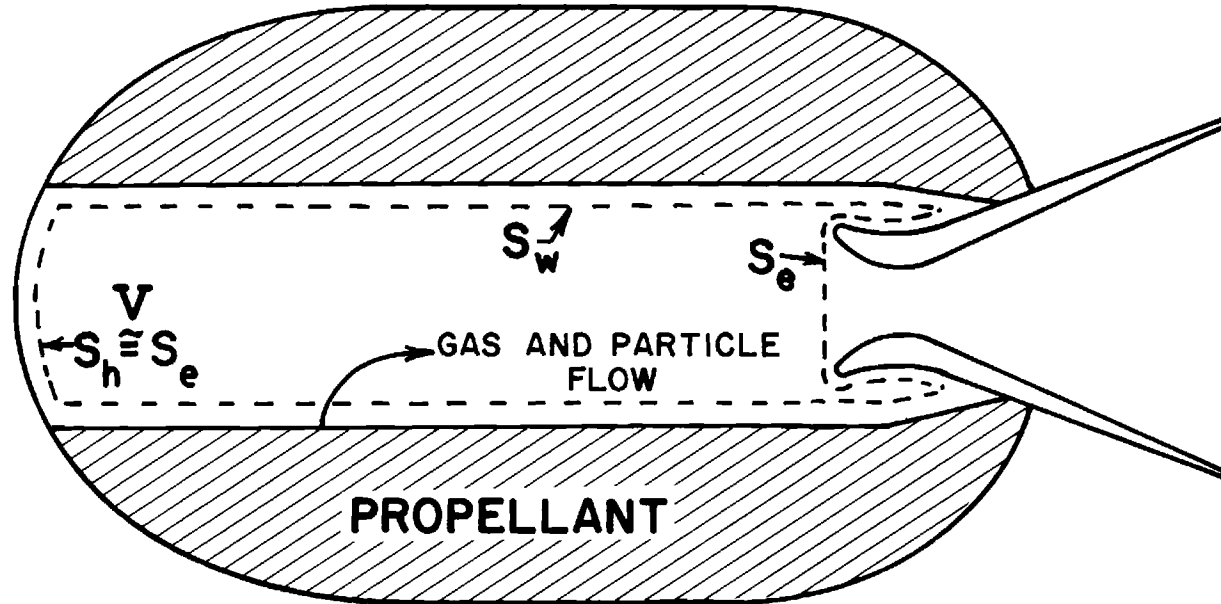


Figure A-1. Schematic of a Rocket Motor and Nomenclature Illustration.

enough off of the propellant surface that all reactions have been completed except those of any metals. Typically this distance will be of the order of hundreds of μm . Across S_w the gas flow is assumed purely radial. Moreover it is assumed that the turbulence does not penetrate S_w . This important assumption is tantamount to assuming that there is no erosive burning effect.⁽¹⁹⁾ The assumption is made for simplicity in the analysis to follow and will be reexamined when some cross flow experiments are considered. Across S_w , therefore, there is a radial, nearly laminar flow containing products of combustion and metals. The metal will be considered to be primarily consumed in V. Typically, even for heavily metalized propellants, the added energy by combustion of the metal is less than 20% of the overall energy of the gases. Consequently, in V there are considered gases with a mean speed of sound equal to c_e about which acoustic and turbulent fluctuations are taking place. The gases will be assumed perfect so that

$$\gamma \frac{p_e}{\rho_e} = c_e^2$$

and the fluctuation in entropy is given by

$$\frac{s'}{c_p} = \frac{p'}{\rho_e c_e^2} + \frac{\rho'}{\rho_e} \equiv \sigma' \quad (13)$$

Equation (12) now becomes

$$\begin{aligned} \frac{\partial^2 \rho_w}{\partial x_i \partial x_i} - (2 + z_d) i k M_e \frac{\partial \rho_w}{\partial x} + \kappa^2 \rho_w = \\ - \frac{1}{c_e^2} \frac{\partial^2}{\partial x_i \partial x_i} (T_{ij})_w - \rho_e \frac{\partial^2}{\partial x_i \partial x_i} \sigma_w \end{aligned} \quad (14)$$

where the Fourier transform of Eq. (13) has been used.

The boundary conditions for Eq. (14) must be developed on S_h , S_w and S_e . On S_h the wall is impervious. Assuming $f_i = 0$ at the head end because velocities and drag are small, Eq. (2) may be evaluated in the x - direction for which $v_1 = u = 0$. Consequently,

$$\left. \frac{\partial p}{\partial x} \right)_{0,r,\theta} = 0 \quad (15)$$

At the nozzle entrance plane a nozzle admittance condition for choked nozzles may be used. (20) It will be found later that, because of the interest here in only very low frequencies, only the plane wave acoustic mode will be under consideration. In this case the admittance conditions is (20)

$$\frac{u_{\omega_{oo}}}{c_e} + a_{\omega} \frac{p_{\omega_{oo}}}{p_e} + b_{\omega} \sigma_{\omega_{oo}} = 0 \quad (16)$$

The oo subscript indicates the plane wave mode and is equivalent to a cross section average of the indicated physical quantity. Considering a one-dimensional mean flow at the nozzle entrance and completed burning so that $m = 0$, Eq. (1) may be written as

$$i \omega \rho_{\omega} + \rho_e \frac{\partial}{\partial x_i} v_{i\omega} + u_e \frac{\partial \rho_{\omega}}{\partial x} = 0 \quad (17)$$

at the nozzle entrance plane after linearization of Eq. (1). Because condensed phase drag is included in the basic differential equation and will be found to have only a minor effect, it will be excluded in writing the momentum equation at the nozzle entrance plane. Linearizing Eq. (2) about the mean flow condition, the transform of Eq. (2) becomes

$$i \omega \rho_e v_{i\omega} + \rho_e u_e \frac{\partial v_{i\omega}}{\partial x} = - \frac{\partial p_\omega}{\partial x} \quad (18)$$

The cross-section average of Eqs. (17) and (18) can be taken, yielding equations in $u_{\omega_{00}}$, $\rho_{\omega_{00}}$ and $p_{\omega_{00}}$, and a combination of Eqs. (16)-(18) then yields

$$\left. \frac{\partial \rho_{\omega_{00}}}{\partial x} \right)_\ell + \tilde{\alpha}_e \rho_{\omega_{00}} \Big|_\ell = \tilde{\beta}_e$$

$$\tilde{\alpha}_e \equiv - i k (M_e + \gamma a_\omega)$$

$$\tilde{\beta}_e \equiv - \rho_e \frac{\partial \sigma_{\omega_{00}}}{\partial x} + i k \rho_e \sigma_{\omega_{00}} (b_\omega + \gamma a_\omega) \quad (19)$$

where the transform of Eq. (13) has been used to eliminate $p_{\omega_{00}}$. Making the Eq. (13) substitution into Eq. (15), taking the cross section average and recognizing that $\sigma_\omega = 0$ at the head end

$$\left. \frac{\partial \rho_{\omega_{00}}}{\partial x} \right)_0 = 0 \quad (20)$$

The boundary condition on the side wall requires some further approximations. The fluctuation in gas mass flow per unit area crossing S_w may be written under the purely radial flow approximation as

$$\frac{m_\omega}{m} = \frac{\rho_\omega}{\rho_e} + \frac{v_{r\omega}}{\bar{v}_r} \quad (21)$$

It is assumed that this consists of the sum of two independent contributions - a fluctuation due to the propellant heterogeneity and a part due

to a pressure sensitivity of burn rate. That is

$$\frac{\dot{m}}{\dot{m}_e} = \mathcal{M}_w + \tilde{\mu} \frac{P_w}{P_e} \quad (22)$$

The feedback response factor, $\tilde{\mu}$, is allowed to be complex and frequency dependent. However, as frequency tends toward zero, it is demanded that $\tilde{\mu}$ tend toward the real valued pressure exponent of the burning rate. The factor \mathcal{M}_w will be determined from experiment. It will also be assumed that $\sigma_w = 0$ on S_w so that the oscillations are nearly isentropic on this surface. Neglecting condensed phase effects also, the transform of the fluctuation of the radial momentum equation may be written as

$$i k \rho_e \frac{v_{r,w}}{c_e} + \rho_e \frac{M_r}{c_e} \frac{\partial v_{r,w}}{\partial r} = - \frac{1}{c_e^2} \frac{\partial p_w}{\partial r} = - \frac{\partial \rho_w}{\partial r} \quad (23)$$

The second term of Eq. (23) will be neglected compared with the first since M_r is usually small (of the order of 0.02) Then substituting Eqs. (21) and (22) into Eq. (23)

$$\begin{aligned} \left. \frac{\partial \rho_w}{\partial r} \right)_{x,a,\theta} + \tilde{\alpha}_w \rho_w \Big|_{x,a,\theta} &= \tilde{\beta}_w \\ \tilde{\alpha}_w &= i k \rho_e M_r (\gamma \tilde{\mu} - 1) \\ \tilde{\beta}_w &= - i k \rho_e M_r \mathcal{M}_w \end{aligned} \quad (24)$$

Although it may seem a bit cavalier to throw out the term above with the M_r multiplier even when the terms in Eqs. (24) are retained with the same multiplier, the reason lies in the essential behavior of the term. $\tilde{\alpha}_w$ contains the feedback term and cannot be discarded, especially since $\tilde{\mu}$ can be large. $\tilde{\beta}_w$ contains the source term \mathcal{M}_w for which the

magnitude is not yet known. The point is that in Eq. (23) the second term is expected to be small compared with the first.

Equations (19), (20) and (24) are the boundary conditions on the problem. Although Eqs. (19) and (20) are specifically written for the plane wave mode, whereas Eq. (24) is general, it will be seen that this causes no difficulty. For solution of the differential equation, therefore, the boundary condition is of the general form

$$\frac{\partial p_w}{\partial x_i} n_i + \tilde{\alpha} p_w = \tilde{\beta} \quad (25)$$

where $n_i = e_1, e_r$ and $-e_1$ at the nozzle, side wall and head end, respectively.

Solution

The method of solution chosen is through use of a Green's function.

If the Green's function satisfies

$$\frac{\partial^2 g_w(x_i, y_i)}{\partial x_i \partial x_i} + (2+z_d) i k M_e \frac{\partial g_w}{\partial x} + k^2 g_w = -\delta(x_i - y_i) \quad (26)$$

with the boundary conditions

$$\begin{aligned} \left. \frac{\partial g_w}{\partial x} \right)_{0,r,\theta} + (2+z_d) i k M_e g_w &= 0 \\ \left. \frac{\partial g_w}{\partial x} \right)_{l,r,\theta} + [\tilde{\alpha}_e + (2+z_d) i k M_e] g_w &= 0 \\ \left. \frac{\partial g_w}{\partial r} \right)_{x,a,\theta} + \tilde{\alpha}_w g_w &= 0 \end{aligned} \quad (27)$$

it may readily be shown that $\rho_{\omega}(x_i)$ is given by

$$\rho_{\omega}(x_i) = \int_V g_{\omega}(x_i, y_i) \Gamma(y_i) dV(y_i) + \int_S g_{\omega} \tilde{\beta} dS \quad (28)$$

That is, Eq. (28) is the solution to Eqs. (12) subject to Eq. (25). The solution consists of a supposition of volume distributed sources and surface distributed sources. The Green's function gives the effective weight of the source (either Γ or $\tilde{\beta}$) at the observation point x_i . The Γ term contains T_{ij} and σ fluctuations and the $\tilde{\beta}$ terms contain σ and \mathcal{M} fluctuations. Evidently, the solution for g_{ω} will contain the nozzle and feedback effects, as well as those of condensed phase drag.

The solution to Eq. (26) subject to Eqs. (27) is carried out by standard methods. (21)

The solution is

$$g_{\omega} = \sum_{\substack{m, n=0 \\ \sigma = \pm 1}}^{\infty} F_{mn}(y) \Psi_{mn}^{\sigma}(\xi, \varphi)$$

$$\Psi_{mn}^{\sigma} = \begin{cases} J_m(\mathcal{K}_{mn}\xi) \cos m\varphi & \sigma = +1 \\ J_m(\mathcal{K}_{mn}\xi) \sin m\varphi & \sigma = -1 \end{cases}$$

$$\mathcal{K}_{mn} J_m'(\mathcal{K}_{mn}a) + \tilde{\alpha}_w J_m(\mathcal{K}_{mn}a) = 0$$

$$F_{mn}'' + (2+z_d) ikM_e F_{mn}' + (\mathcal{K}^2 - \mathcal{K}_{mn}^2) F_{mn} = - \frac{\delta(x-y) \Psi_{mn}^{\sigma}(r, 0)}{\Lambda_{mn} S_e}$$

$$F_{mn}'(0) + (2+z_d) ikM_e F_{mn}(0)$$

$$= F_{mn}'(\ell) + [\tilde{\alpha}_e - (2+z_d) ikM_e] F_{mn}(\ell) = 0 \quad (29)$$

which requires the solution to the F_{mn} differential equation. For any m,n pair the solution will look like

$$F_{mn} = A_- e^{\eta_- x} + A_+ e^{\eta_+ x}$$

with

$$\eta_{\pm} = ik \left[\pm \frac{k_{mn}}{k} - (1 + z_d/2) M_e \right]$$

$$k_{mn}^2 = \mathcal{K}^2 - \mathcal{K}_{mn}^2 \quad (30)$$

The lowest root of the defining equation for the \mathcal{K}_{mn} in Eqs. (29) is designated as the 00 mode and corresponds to the nearly plane wave mode. Noting that $\tilde{\alpha}_w$ is small, $\mathcal{K}_{00} \approx 0$, and, by expanding the Bessel functions in their appropriate power series for small values of the argument, it is found that

$$\mathcal{K}_{00} = \left(\frac{2\tilde{\alpha}_w}{a} \right)^{1/2} \quad (31)$$

which is a small, complex number. The next highest root is the 01 case which corresponds to the first antisymmetric transverse mode. The solution will be restricted to values of frequency such that $\mathcal{K}^2 < \mathcal{K}_{01}^2$. The transverse modes are then "cut-off" because k_{mn} for all transverse modes contains an imaginary part from Eqs. (30). The solution for F_{mn} then shows that these modes decay with x ; they are non-propagating. Consequently, only the plane wave mode need be considered, which is the first term in the series solution for g_w , in Eqs. (29). In the following, the 00 subscript will be dropped, it being understood that this is the only mode under consideration. This is the reason for expressing the boundary conditions of Eqs. (19) and (20) in plane wave form.

The solution to the F equation with the boundary conditions of Eqs. (29) also requires the statement that F is continuous at the singular point $x = y$. Then

$$\begin{aligned} F_R &= A_- e^{\eta-y} + A_+ e^{\eta+y} & x > y \\ F_L &= B_- e^{\eta-y} + B_+ e^{\eta+y} & x \leq y \end{aligned} \quad (32)$$

with the A's and B's determined from the four simultaneous equations

$$\begin{aligned} B_- (1-\mathcal{E}) - B_+ (1+\mathcal{E}) &= 0 \\ B_- e^{\eta-x} (1+\mathcal{E}) - B_+ \frac{(1-\mathcal{E})^2}{1+\mathcal{E}} e^{\eta+x} - A_- (1+\mathcal{E}) e^{\eta-x} + A_+ (1-\mathcal{E}) e^{\eta+x} &= \frac{i \psi_{00}(r, \theta)}{S k_{00}} \\ B_- e^{\eta-x} + B_+ e^{\eta+x} - A_- e^{\eta-x} - A_+ e^{\eta+x} &= 0 \\ A_- (1+q) e^{\eta-l} - (1-q) A_+ e^{\eta+l} &= 0 \end{aligned} \quad (33)$$

with

$$\begin{aligned} \mathcal{E} &= (1+z_d/2) M_e k/k_{00} \\ q &= \frac{i \tilde{\alpha}_e}{k_{00}} - (1+z_d/2) \frac{k}{k_{00}} M_e \end{aligned}$$

Since $\psi_{00} \approx 1$, in the plane wave limit $g_{\omega} = F(x, y)$.

An interesting calculation is in determining g_{ω} in the limit of low frequency. Carefully taking the limit of $\omega \rightarrow 0$ in Eqs. (33) and Eq. (32), it is found that a) the Green's function becomes independent of x and y (this becomes a bulk mode oscillation) and b) the following simple formula emerges:

$$g_{\omega} g_{\omega}^* = g_{\omega}^2 = \frac{1}{M_e^2 S^2 k^2 \left(\frac{5+\gamma}{2} - \tilde{\gamma}_{\mu} \right)^2} \quad (34)$$

Thus, since $g_{\omega}^2 \propto 1/k^2$, the Green's function becomes unbounded at low frequency which physically will mean that low frequencies are favored by the duct acoustics. Note in Eq. (34), if $\tilde{\mu}$ is large enough, $g_{\omega}^2 \rightarrow \infty$.

That is, with enough positive feedback from the propellant the system may be driven unstable, as is well known. Since \tilde{u} may actually be complex, the square operation of Eq. (34) is really to be interpreted as the quantity in brackets times its complex conjugate. In Eq. (34) the effect of droplet drag disappears at low frequency. This low frequency solution will be found to be useful for order of magnitude arguments. In general however, Eqs. (33) must be solved exactly.

Extension to Non-Circular Geometry

Since it has been found that only the plane wave mode is under consideration, this will permit an approximate generalization of the results to non-circular shapes of (nearly) constant cross-section area as a function of axial position. An example would be that of a star grain. If an effective circular radius is defined in terms of the cross-section area as

$$\pi a_e^2 = S_c$$

it is assumed that a_e may be used in place of a in the theory above. The radius, a , appears in K_{00} and physically measures the lateral length scale of distortion of the plane wave. The same physics are obtained by the approximate procedure.

Assuming for approximate calculation purposes that there are no condensed phases, a mass balance yields

$$\rho_e u_e S_c = \rho_e \bar{v}_r S_w \quad (35)$$

with $S_w = P\ell$. This yields a constraint on the ratio of $u_e/\bar{v}_r \approx M_e/M_r$ in terms of geometrical variables. The question arises as to an effective value of M_r to use in the theory for non-circular grains. Since the boundary condition is being applied at an effective radius, a_e , a mass

balance for an effective radial inflow at a_e yields

$$\rho_e \bar{v}_{r_e} 2\pi a_e \ell = \rho_e \bar{v}_r S_w$$

or

$$\frac{\bar{v}_{r_e}}{\bar{v}_r} \approx \frac{M_{r_e}}{M_r} = \frac{S_w}{2\pi a_e \ell} \quad (36)$$

Equation (35) provides M_e/M_r for a given grain and Eq. (36) gives a correction to M_r to be used in the theory above. The corrected M_r physically enters to gauge the amount of flow from the propellant and its effect upon the acoustic field. For large area grains (e.g., a star compared with a circular port) $M_{r_e} > M_r$ which gives the same physical effect in the theory as occurs in practice; that is, there is a stronger incoming radial flow. Therefore, the approximations of this section, while somewhat coarse, are expected to yield proper scaling behavior and orders of magnitude, in accord with the purposes here.

Calculations of the Green's Function

In order to show some general trends and to see where Eq. (34) may be a useful approximation, some exact calculations, via, Eqs. (32) and (33), have been carried out. The baseline motor parameters used in computation are shown in Fig.A-2. $M_e = 0.3$ is a relatively high number and is so chosen in anticipation of some results to follow. The short nozzle assumption means that the wavelength under consideration is long compared with the nozzle length. Under this condition the nozzle behaves in a quasi-steady fashion and⁽²⁰⁾

$$a_w = - \frac{\gamma-1}{2\gamma} M_e$$

It may readily be verified in the theory that if more than one condensed

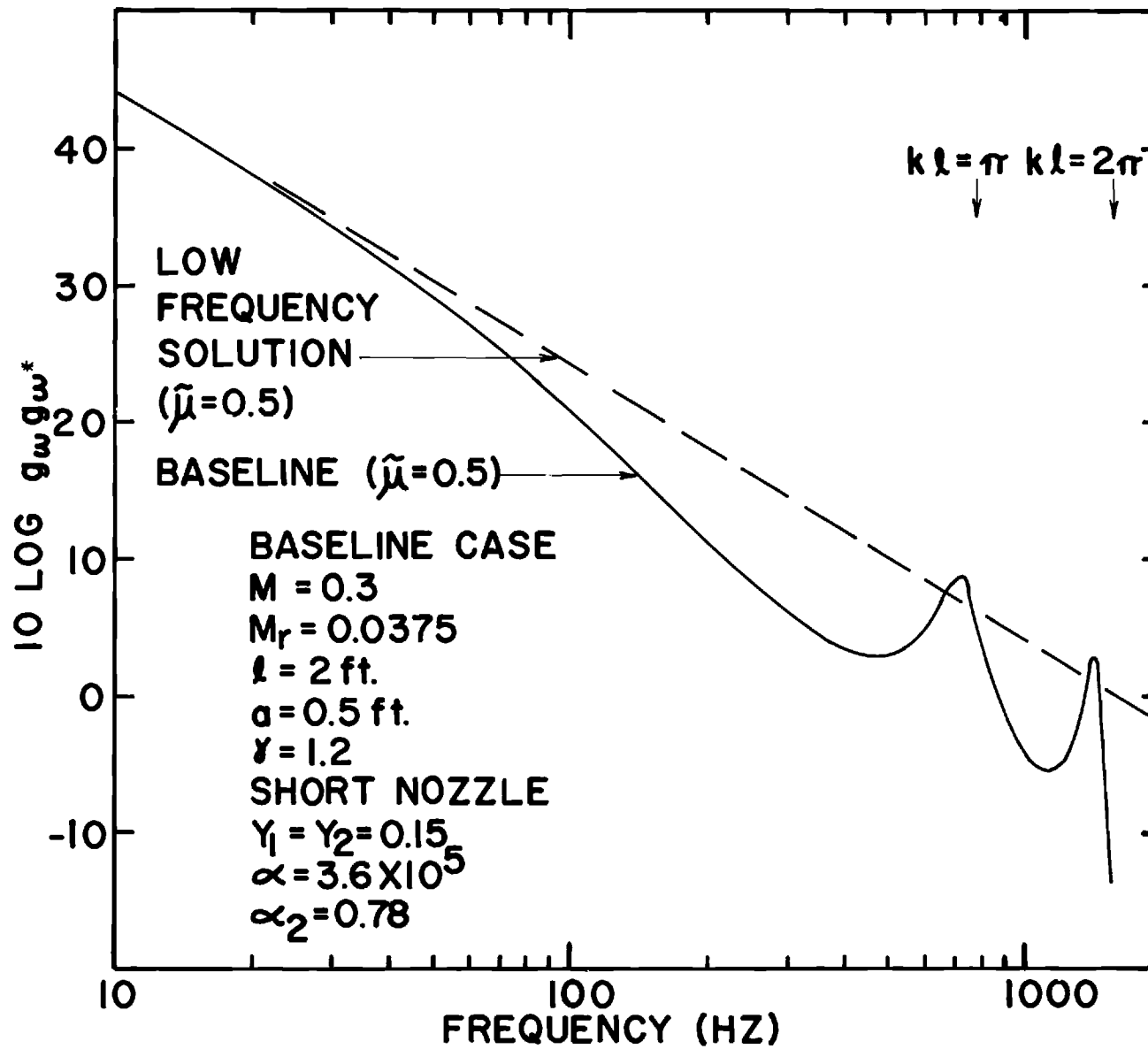


Figure A-2. Green's Function for Baseline Case and Its Low Frequency Approximation.

phase group is present

$$z_d = \sum_i z_{d_i}$$

where z_{d_i} is calculated on the basis of the properties of the i^{th} group. It is assumed for these calculations that Al and Al_2O_3 are present at an average mass fraction of 0.15 each and that the Al diameter is $300 \mu\text{m}$ and the Al_2O_3 diameter is $1 \mu\text{m}$. This yields the α_1 and α_2 values in Fig. A-2.

Two curves are shown in Fig. A-2. One is an exact calculation with $n=0.5$, and one is the approximate solution of Eq. (34). There is generally good agreement in trend and magnitude except, of course, the approximate solution contains no resonance phenomena. The error in the approximate solution, however, never exceeds 10 dB and this will greatly aid in order of magnitude arguments later.

The resonances, corresponding to the first and second longitudinal modes, are clearly seen in Fig. A-2. The nozzle behaves as a relatively hard wall, and, if there were no flow present the resonance of the first longitudinal mode would occur at $k_1 = \pi$. The flow effect shifts the actual resonance frequency slightly down from $k_1 = \pi$.

Figure A-3 shows the Green's function for various pairs of values of x and y . While the behavior can become quite complex at the high frequency end of the spectrum, below about 200 Hz the relative values of x and y make no difference. At low frequency the oscillation gives way to a nearly bulk mode oscillation which is quite well predicted by the approximate equation, Eq. (34). It should be noted that the Green's function is symmetric; that is $g_{\omega}(x,y) = g_{\omega}(y,x)$.

Figure A-4 shows the effect of the feedback parameter $\tilde{\mu}$ for various real values and one imaginary value. From the asymptotic solution of Eq. (34) it is seen that $\tilde{\mu} = (5-\gamma)/2$ is a critical value for the low

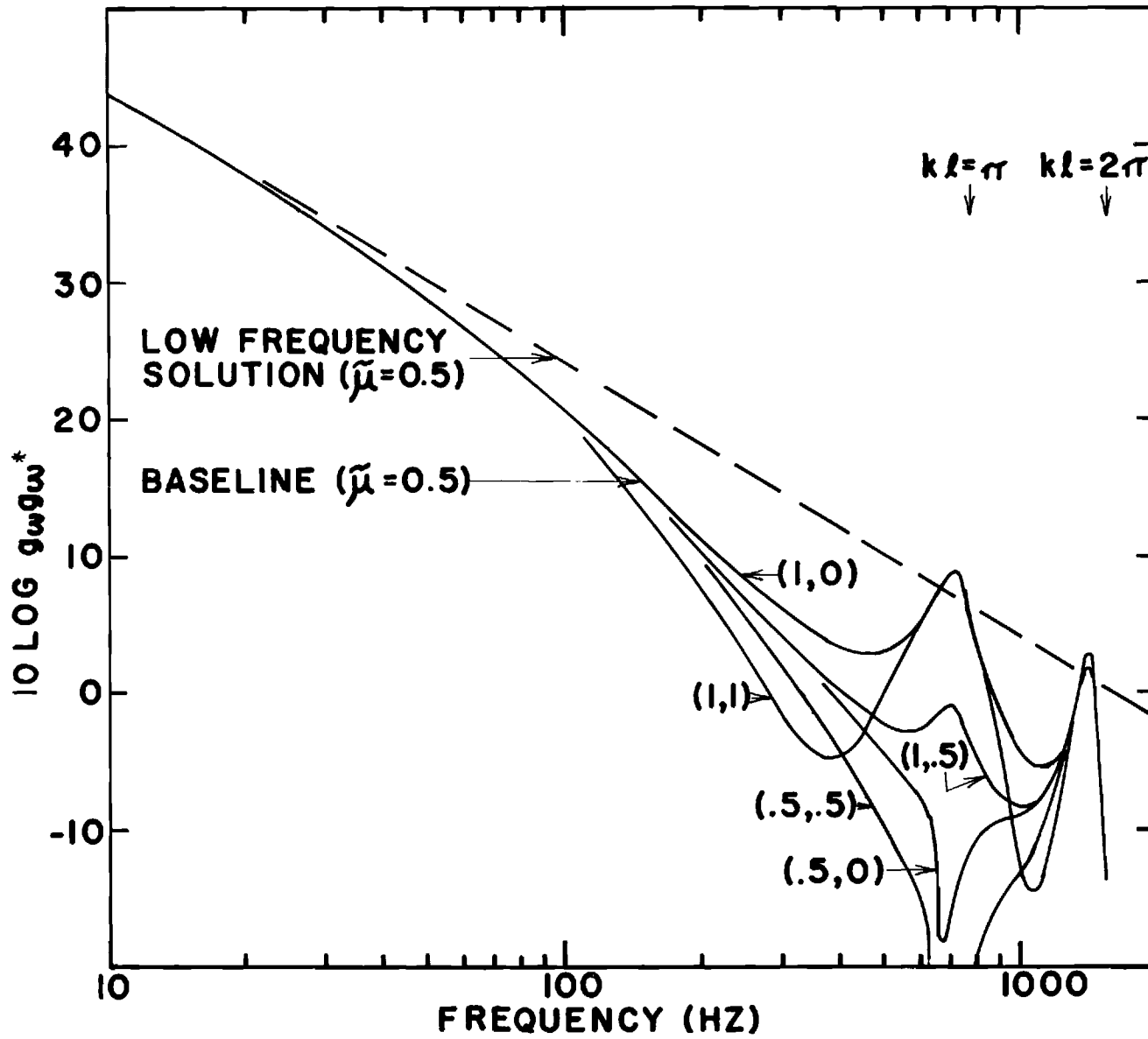


Figure A-3. Green's Function for Various Pairs of Values of x and y .

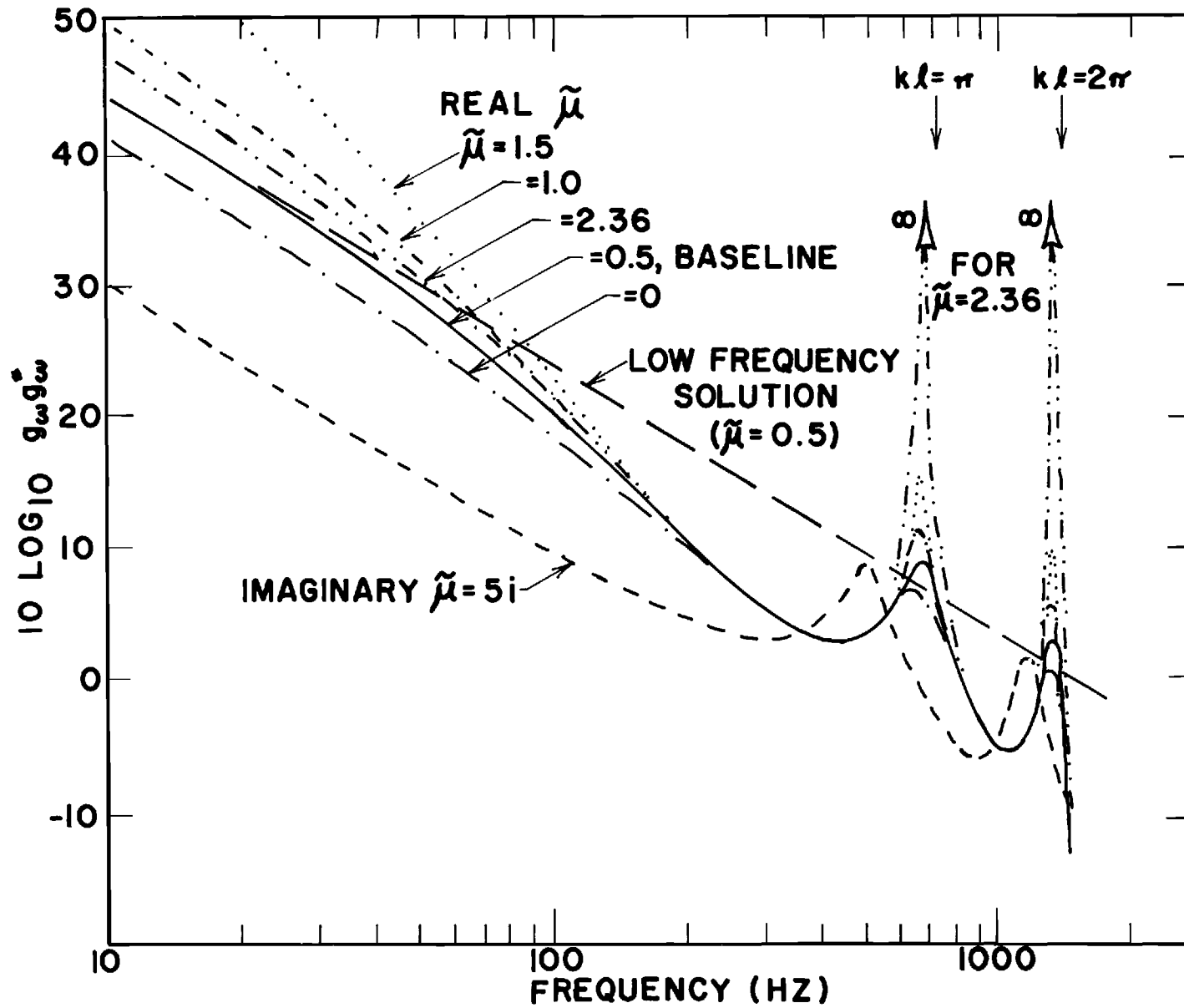


Figure A-4. Green's Function for Various Values of the Feedback Parameter, $\tilde{\mu}$.

frequency solution. By calculation, at the resonance point of the first longitudinal mode $\tilde{\mu} = 2.36$ is a critical value. Above these values, and if $\tilde{\mu}$ is real, a stationary random oscillation is impossible and an unstable oscillation will occur. It is assumed here that $\tilde{\mu}$ is always below the critical stability value. The imaginary value of $\tilde{\mu}$ primarily effects the resonant frequency at moderate frequencies, but at low frequency it also affects the magnitude of g_{ω} , as may be seen from Eq. (34) and Fig. A-4.

In Fig. A-5 the effect of Mach number is shown. Both M and M_r must be varied simultaneously for a given motor geometry as demanded by Eq. (35). The Mach number is varied by a factor of two in Fig. A-5. The effect of lowering M is to decrease the nozzle damping. This is especially effective at low frequency and at resonance points.

In Fig. A-6 the effect of M_r alone is shown under the constraint that the motor mass flow (thrust) is the same. By Eq. (36), this constraint requires M_r/a to be maintained constant. Consequently, Fig. A-6 is interpreted as the effect of a change in grain configuration to accommodate a slower burning propellant. There is an important effect of this variable. Slower burning propellants raise g_{ω} .

Finally, the effect of particle damping is shown in Fig. A-7. There is a surprisingly small effect when the particle mass fraction is changed. It was anticipated by example in the instability field⁽²²⁾ that the effect would be stronger. In fact, here the effect is negligible. If one reviews the equations it can be seen that the comparative magnitude of z_d terms is quite small.

It appears that only near unstable resonance points can the effect show up strongly. This is limited by the behavior at the longitudinal

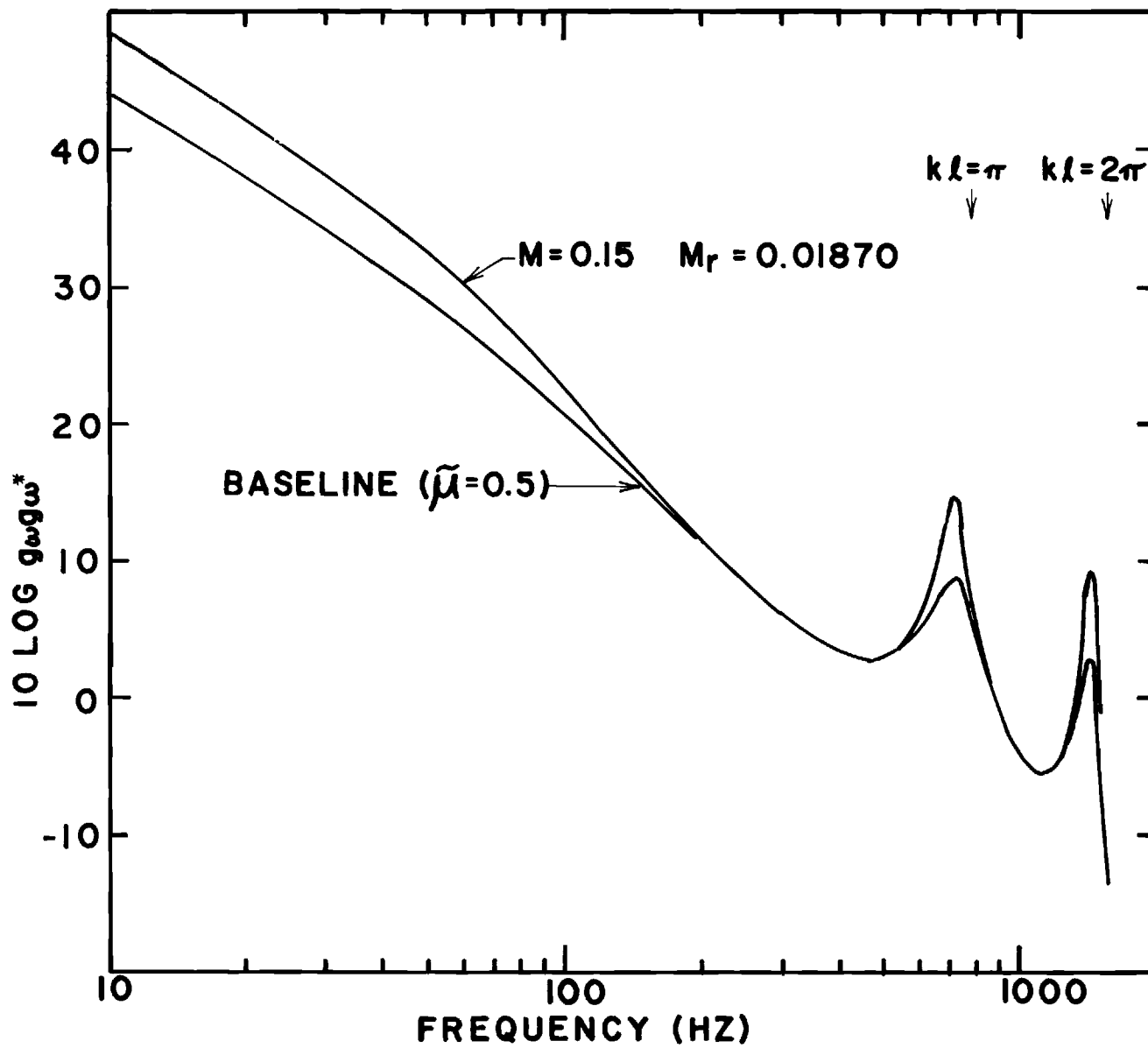


Figure A-5. Green's Function for Two Values of Exit Mach Number.

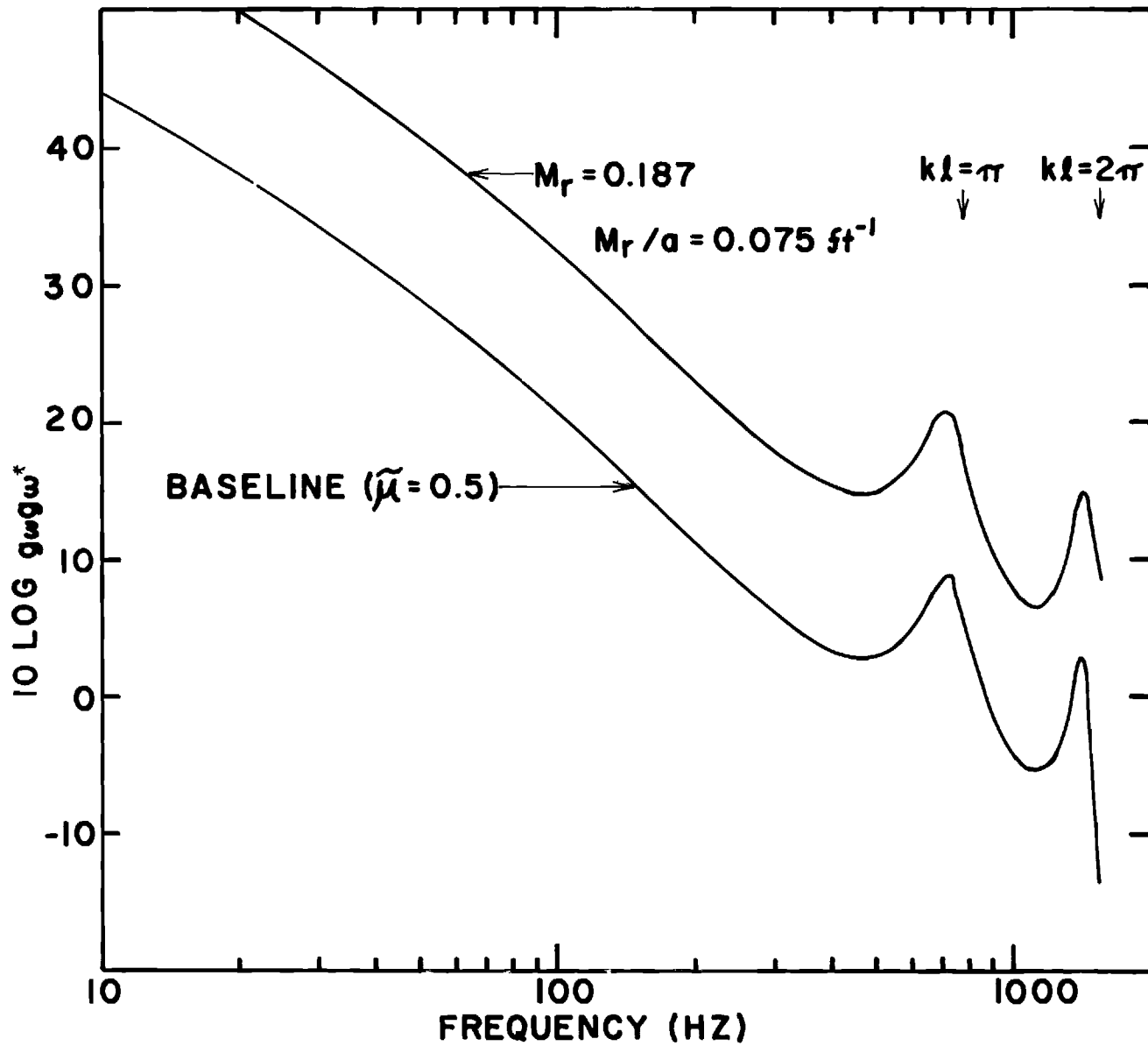


Figure A-6. Green's Function for Two Values of Radial Mach Number at Fixed Motor Thrust

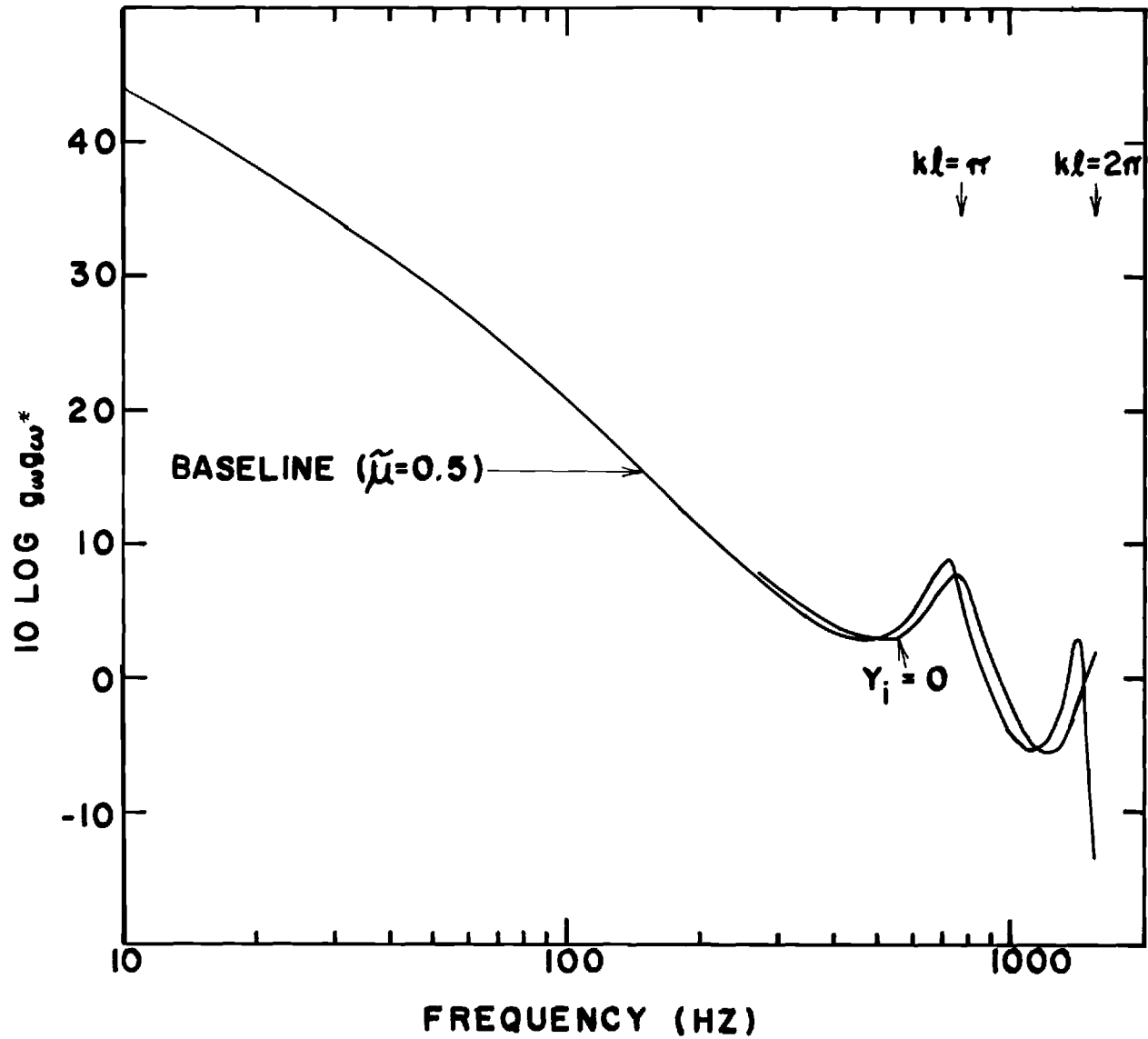


Figure A-7. Effect of Particle Mass Loading on the Green's Function.

mode resonance point. By and large, however, the particle damping effect is negligible for these stationary random oscillations for moderate $\tilde{\mu}$. Not shown are the effects of particle size change, because they are as ineffective as mass fraction changes in affecting the curves.

Summarizing, the behavior of the g_{ω} function is strongly affected by feedback parameter, flow speeds, and burn rate, but is insensitive to particle effects. The low frequency solution is adequate for order of magnitude arguments sufficiently far away from onset of the first longitudinal mode.

Decomposition of the Solution

Viewing Eq. (28), it is desired to further manipulate the solution into a form suitable for computation. Consider first the first term on the right hand side of Eq. (14). Repeated application of the divergence theorem, using the assumption that $T_{ij}' = 0$ on all S except S_e and using Eq. (26), the following operations are carried out.:

$$\begin{aligned}
 & \int_V g_{\omega}(x_i, y_i) \frac{1}{c_e^2} \frac{\partial^2 (T_{ij})_{\omega}}{\partial y_i \partial y_j} dV(y_i) \\
 &= \frac{1}{c_e^2} \int_V \left\{ \frac{\partial}{\partial y_j} \left[g_{\omega} \frac{\partial}{\partial y_i} (T_{ij})_{\omega} \right] - \frac{\partial g_{\omega}}{\partial y_j} \frac{\partial}{\partial y_i} (T_{ij})_{\omega} \right\} dV(y_i) \\
 &= \frac{1}{c_e^2} \int_{S_e} \left[g_{\omega} \frac{\partial (T_{ij})_{\omega}}{\partial y_i} \right] dS(y_i) - \int_{S_e} \frac{\partial g_{\omega}}{\partial y_j} (T_{ij})_{\omega} dS + \int_V \frac{\partial^2 g_{\omega}}{\partial y_j \partial y_i} (T_{ij})_{\omega} dV \\
 &= \frac{1}{c_e^2} \int_{S_e} \left[g_{\omega} \frac{\partial (T_{ij})_{\omega}}{\partial y_i} \right] dS - \int_{S_e} \frac{\partial g_{\omega}(x, y)}{\partial y} (T_{11})_{\omega} + \int_V \frac{\partial^2 g_{\omega}}{\partial y^2} (T_{ii})_{\omega} dV
 \end{aligned}$$

$$\begin{aligned}
= & \int_{S_e} \left[g_\omega \frac{\partial}{\partial y_i} (T_{11})_\omega \right] dS + \int_{S_e} \left[\tilde{\alpha}_e + (2 + z_d) ikM_e \right] g_\omega (T_{11})_\omega dS \\
& - T_{11}(x_i) - \kappa^2 \int_V g_\omega (T_{11})_\omega dV
\end{aligned} \tag{37}$$

In developing Eq. (37), terms of the order of M_e compared to unity have been dropped, consistent with the procedure used for the right hand side of Eq. (14). The first term on the right hand side of Eq. (37) is a rather complicated interaction of the turbulence with the nozzle entrance plane. The next three terms only depend upon T_{11} , with the first being a nozzle entrance plane interaction the second being the locally observed density fluctuation due to the turbulence and the third is a volume distribution effect. Similar manipulation can be made involving the σ_ω term which comprises Γ . The second term of the right hand side of Eq. (28) is obtained by plugging in the appropriate β values on the appropriate surfaces. There is then a reasonable amount of cancellation which occurs among various terms. The final solution for ρ_ω appears as

$$\rho_\omega(x_i) = I_a + I_b + I_c + II_a + II_b + III + IV_a + IV_b$$

$$I_a = - \frac{\kappa^2}{c_e^2} \int_V g_\omega (T_{11})_\omega dV$$

$$I_b = \frac{1}{c_e^2} \int_{S_e} \left[\tilde{\alpha}_e + ikM_e (2 + z_d) \right] g_\omega (T_{11})_\omega dS$$

$$I_c = \frac{1}{c_e^2} \int_{S_e} \left[g_\omega \frac{\partial}{\partial y_i} (T_{11})_\omega \right] dS$$

$$\begin{aligned}
II_a &= - ik\rho_e \int_{S_w} \mathcal{M}_w g_w dS \\
II_b &= - \frac{\mathcal{K}}{c_e} \rho_e \int_V \left(\frac{D\sigma}{Dt} \right)_w g_w dV \\
III &= ik\rho_e \int_{S_e} \sigma_w b_w g_w dS \\
IV_a &= - \frac{1}{c_e} 2 (T_{11})_w \\
IV_b &= - \rho_e \sigma_w
\end{aligned} \tag{38}$$

Notice also Eq. (13) so that if one calculates the pressure transform, term IV_b does not enter the pressure calculation. Moreover, at the head end and side walls $IV_a = 0$ so that terms I-III are the only terms of interest in the wall pressure, and, hence the vibration problem.

Discussion of Eqs. (38) is now in order. Term I_a is an effect of distributed turbulence on pumping up axial oscillations. It depends only on the axial components of T_{ij} . Term I_b is an interaction of the axial T_{ij} with the nozzle. So is term I_c . Terms II_a and II_b are direct combustion noise terms, with II_a caused near the propellant surface and II_b by burning of any particulate matter in the bulk volume of the chamber. Term III is an interaction of hot spots with the nozzle and is called entropy noise. Note it is directly proportional to the entropy admittance coefficient, b_w .

This solution is actually quite remarkable in its simplicity and capture of the essential physics. It contains all effects which were anticipated at the outset. This was not guaranteed because the approach is an approximate one and the Lighthill approach has not been previously attempted, to the author's knowledge, on an interior acoustics problem. In independent

calculations, not presented here, the term which will survive of terms I_b and I_c turns out to be identical with a vorticity-nozzle interaction term derived if the formulation used is the linearized acoustic-vorticity approach to aeroacoustics. Term III is similar in form and scales in the same manner as entropy noise derived from a different approach.⁽¹²⁾ Term II_b is identical in form with previous results in combustion noise⁽¹⁾ Therefore, there is a high degree of confidence that the solution of Eqs. (38) represents a complete picture of the actual solution, will yield proper orders of magnitude and will yield proper scaling laws. The problem now is to obtain numbers to set into the theory to make the actual computations.

References

1. Strahle, W. C., On combustion generated noise, Journal of Fluid Mechanics, 49, 339 (1971).
2. Pickett, G. F., Core engine noise due to temperature fluctuations convecting through turbine blade rows, Aeroacoustics; Jet Noise, and Core Engine Noise (Schwartz, ed.) p. 589, AIAA, New York (1976).
3. Strahle, W. C., A review of combustion generated noise, Aeroacoustics: Jet and Combustion Noise; Duct Acoustics (Nagamatsu, ed) p. 229, AIAA, New York (1975).
4. Lighthill, M. J. On sound generated aerodynamically, I. General theory, Proc. Roy. Soc. London, A 211, 564 (1952).
5. Goldstein, M. E., Aeroacoustics, McGraw-Hill, New York (1976).
6. Bendat, J. S. and Piersol, A. G., Random Data: Analysis and Measurement Procedure, Wiley, New York (1971).
7. Laufer, J., The structure of turbulence in fully developed pipe flow, NACA Tech. Rept. No. 1174 (1954).
8. Yamada, K., Soto, M. and Ishikawa, N., Simulative study on the erosive burning of solid rocket motors, AIAA Journal 14, 1170 (1976)
9. Bell, W. A., Craig, J. S., and Strahle, W. C., Study of unsteady combustion of heterogeneous solid propellants by analysis of acoustic emissions, AIAA Paper No. 77-15 (1977).
10. Bell, W. A., Craig, J. I., and Strahle, W. C., Audible and ultrasonic acoustic emissions from composite solid propellants, AFOSR Final Report AFOSR TR 78-009 September, 1977.
11. Price, E. W., Samant, S. S., Sigman, R. K., Meyer, W. L., Powell, E. A., Handley, J. C. and Strahle, W. C., The fire environment of a solid rocket propellant burning in air, Final Report, AFWL Contract No. F29601-76-C-0119, February 1978.

12. Strahle, W. C., Muthukrishnan, M., Neale, D. H., and Ramachandra, M. K.,
An investigation of combustion and entropy noise, NASA CR 135220 (1977).
13. Schlichting, H., Boundary Layer Theory, McGraw-Hill, New York (1960).
14. Aerothermochemistry Division, Combustion of solid propellants and low
frequency instability progress report 1 April - 30 September 1967,
NWC TP 4478 (1968).
15. Ribner, H. S., Quadrupole correlations governing the pattern of jet
noise, J. Fluid Mech. 38, pt. 1, 1 (1969).
16. Culick, F. E. C., A review of calculations for unsteady burning of a
solid propellant, AIAA Journal, 6, 2241 (1968).
17. Aerothermochemistry Division, Experimental studies on the oscillatory
combustion of solid propellants, NWC TP 4393 (1969).
18. Culick, F. E. C., Stability of longitudinal oscillations with pressure
and velocity coupling in a solid propellant rocket, Combustion Science
and Technology 2, 179 (1970).
19. Crocco, L. and Sirignano, W. A., Behavior of supercritical nozzles
under three-dimensional oscillatory conditions, AGARD ograph No. 117,
NATO (1967).
20. Morse, P. M. and Ingard, K. U., Theoretical Acoustics, McGraw-Hill,
New York (1968).